Analysis of Planar Measurements of Turbulent Flows

Pedersen, Jakob Martin; Sørensen, Jens Nørkær; Meyer, Knud Erik

Publication date:
2003

Document Version
Publisher's PDF, also known as Version of record

MEK-PHD 2003-01

Analysis of Planar Measurements of Turbulent Flows

by

Jakob M. Pedersen

Dissertation submitted to the Technical University of Denmark in partial fulfillment of the requirements for the degree of Doctor of Philosophy in Mechanical Engineering

Fluid Mechanics
Department of Mechanical Engineering
Technical University of Denmark
February, 2003

Fluid Mechanics
Department of Mechanical Engineering
Building 403
Technical University of Denmark
DK-2800 Lyngby, Denmark

Printed in Denmark by DTU-Tryk, Lyngby

Report MEK FM 2003-01 / ISBN 87-7475-292-8

This thesis has been typeset using LaTeX2e.

Preface

This dissertation is submitted in partial fulfillment of the requirements for obtaining the degree of Doctor of Philosophy in Mechanical Engineering. The dissertation is based on research work carried out during the period from February 2000 to January 2003 at the Department of Mechanical Engineering, Fluid Mechanics Section, at the Technical University of Denmark. The work was carried out under the guidance of Associate Professor, Ph.D. Knud Erik Meyer and Professor, Ph.D. Jens Nørkær Sørensen, and has been supported by a scholarship for the Ph.D. programme in Mechanical and Civil Engineering at the Technical University of Denmark.

First of all I would like to express my gratitude to my supervisors for all their help throughout the course of my study. The application of experimental as well as theoretical techniques would not have been possible without them both. Special thanks are also due to prof. dr. ir. Jerry Westerweel, for his inspiring supervision during my three month stay at the Department for Aero and Hydrodynamics, Delft University of Technology, The Netherlands, in the spring of 2002. I would like to thank my colleagues at the Fluid Mechanics Section for creating a friendly and stimulating environment. Especially the co–operation with former guest professor Oktay Özcan, performing the experiments on the jet-in-crossflow, is gratefully acknowledged. A special thanks also goes to Mads Reck for many fruitful discussions and help with proof–reading.

Finally, I would like to thank my family and best friends and not least my loving girlfriend, Karina, for always being there for me.

Technical University of Denmark
Copenhagen, February 2003

Jakob M. Pedersen
M.Sc., Mech.Eng.

Abstract

Analysis of turbulent velocity data, obtained by Particle Image Velocimetry (PIV), has been carried out. The reason for applying PIV was its ability to provide instantaneous realizations in a plane of a flow, which facilitates a quantitative study of spatial coherent flow structures. The main tool used for the investigations was the Proper Orthogonal Decomposition (POD). Also, Linear Stochastic Estimation (LSE), as well as traditional statistical analysis, has been applied to explore the data. Following a description of the theory behind the analysis techniques, three cases of engineering relevancy were considered. The results of the investigations can be summarized as follows.

In the first case considered, uncorrelated as well as temporally resolved data was obtained in a plane of a scale model of the Annex 20 room, which is a standard measure room used for investigation of ventilation problems. The data was obtained in a region near the inlet, where a wall jet enters the room along the ceiling below which a region with slowly developing flow structures is found. A POD analysis was carried out, which permitted a study of the temporal variation of the influence of the most dominant flow structures occurring in this region of the room. Further, the length scales were investigated and the dominant structures derived from the POD were reproduced with LSE. The results showed that flow structures which differ substantially from the mean velocity field are important to the dynamics of the flow in the Annex 20 room.

In the second case, the complex flow found in the near field of the turbulent jet-in-crossflow (JICF) was investigated. Stereoscopic PIV measurements yielding all three velocity components in different planes near the jet exit were carried out. The mean velocity fields were presented to give a picture of the evolution of the JICF along and downstream of the jet trajectory. Carrying out POD analyses in a number of mutually perpendicular planes revealed that the dominant structures of the near field of the JICF are found just downstream of the jet trajectory, and that these are associated with velocity fluctuations normal to the symmetry plane. Based on these observations, it was conjectured that the maximum production of turbulent kinetic energy results from the inititation of the wake vortices of the JICF which in turn seems to be connected to the dynamics of the characteristic counter–rotating vortex pair.

The third and final case considered was the free axisymmetric turbulent jet. Raw measurement data obtained with PIV and Laser Induced Fluorescence (LIF) were processed to obtain combined velocity and concentration fields in a region centered 80 jet diameters downstream. The mean velocity field was depicted and compared to the results of a self similarity analysis. Detecting the jet boundary from the LIF data, statistical quantities could be derived relative to the turbulent/non-turbulent interface between the jet fluid and the ambient fluid. The results showed a change in velocity gradient across the interface caused by a vorticity maximum, which is believed to be

caused by the frequent occurrence of small scale vortices in this region. Further, it was shown that the velocities and the root mean squared values of their fluctuating parts scale with the mean centerline velocity and the jet half-width, when moving downstream. The same behavior was not observed for the vorticity profile, for which the maximum detected just within the jet boundary seems to increase with downstream position relative to a fixed universal value within the jet region.

Resumé

Nærværende afhandling har omhandlet analyse af turbulente hastighedsdata målt med Particle Image Velocimetry (PIV). PIV–teknikken er særligt anvendelig, da denne producerer øjebliksbilleder af hastighedsfelter, hvilket muliggør et studium af rumlige kohærente strømningsstrukturer. Det primært benyttede analyseværktøj har været Proper Orthogonal Decomposition (POD). Herudover er Linear Stochastic Estimation (LSE), samt klassisk statistisk analyse blevet benyttet ved undersøgelserne. Efter en indledende beskrivelse af analyseteknikkerne er tre ingeniørmæssige strømningsproblemer blevet undersøgt. Resultaterne af disse undersøgelser kan opsummeres som følger.

Det først undersøgte problem var Annex 20 rummet, et standard rum defineret med repræsentative dimensioner til brug ved undersøgelse af ventilationsproblemer. Ukorrelerede og tidsligt opløste hastighedsfelter blev målt i et plan i umiddelbar nærhed af indløbet, hvor en såkaldt væg–jet udbredes langs loftet. Under jet'en findes et større område med strømningsstrukturer, der udvikler sig langsomt i tiden. Gennem en POD analyse kunne den tidslige udvikling af indflydelsen af de dominerende strukturer følges i denne del af rummet. Herudover blev en undersøgelse af længdeskalaerne foretaget og de dominerende strukturer fundet ved POD analysen reproduceret via LSE. Resultaterne viste, at strømningsstrukturer, der afviger væsentligt fra det gennemsnitlige hastighedsfelt, er af betydning for strømningen i Annex 20 rummet.

Det andet betragtede problem var det komplicerede strømningsfelt, der opstår i "nærfeltet" af en jet i en tværstrøm (JITS). Hastighedsdata inkluderende alle tre komposanter blev målt i forskellige planer i nærheden af jet indløbet ved hjælp af Stereoskopisk PIV. Ud fra middelhastighedsfelterne kunne udviklingen af JITS'en studeres langs den bane, som jet'en følger samt nedstrøms for denne. POD analyser i en række indbyrdes ortogonale planer afslørede, at de mest dominerende strømningsstrukturer i nærfeltet af JITS'en findes umiddelbart nedstrøms for jet–banen og er forbundet med hastighedsfluktuationer i retningen vinkelret på symmetriplanet. Disse resultater har ført til den konklusion, at den maksimale produktion af turbulent kinetisk energi stammer fra initieringen af de hvirvler, der opstår i kølvandet af JITS'en. Denne initiering synes endvidere forbundet med dynamikken af det karakteristiske fænomen, der er kendt som "the counter–rotating vortex pair".

Det tredje og sidste undersøgte strømningsproblem var den frie aksesymmetriske turbulente jet. Processering af rå måledata erhvervet via PIV og Laser Induced Fluorescence (LIF) førte til et datast bestående af kombinerede hastigheds– og koncentrationsfelter i et område centreret 80 diametre nedstrøms. Middelhastighedsfeltet blev vist og sammenlignet med resultaterne af en såkaldt selv–similaritets analyse. Ved at detektere randen af jet'en fra LIF billederne kunne statistiske størrelser udledes som funktion af afstanden til den turbulent/ikke–turbulente grænseflade, der findes mellem

jet fluiden og den omgivende fluid. Resultaterne viste, at der forekommer en ændring i hastighedsgradienten henover grænsefladen. Ændringen afstedkommes af et vorticity maksimum, som sandsynligvis er relateret til den hyppige forekomst af små hvirvler i dette område. Endelig blev det vist, hvorledes hastighederne og root mean square værdierne af deres fluktuerende del skalerer med middelhastigheden på centerlinien samt den halve jet bredde, når man bevæger sig i nedstrøms retning. Samme tendens kunne ikke observeres for vorticity profilerne. Her synes en stigning i det vorticity maksimum, der findes umiddelbar indenfor randen af jet'en, at forekomme i forhold til et globalt fastlagt niveau i selve jet'en.

Contents

Chapter 1

Introduction

As the title "Analysis of Planar Measurements of Turbulent Flows" indicates, the present thesis addresses the task of analyzing turbulent velocity data obtained from experiments. More specifically, the data under consideration are obtained with Particle Image Velocimetry, which provides series of instantaneous flow realizations in a given plane of the flow at a given (finite) resolution. The main part of the analysis is carried out with regard to a study of the large scale organized motions present in turbulent flows known as coherent structures. In the present chapter, an introduction to the phenomenon of coherent structures is given together with a brief overview of the concepts of Particle Image Velocimetry. Also, a short description of the cases investigated and an outline of the contents of the thesis is provided.

1.1 Turbulence and coherent structures

Fluid mechanics represents one of the biggest areas of science today. The theoretical descriptions of fluid mechanics go all the way back to Archimedes, and a survey of its history is a whole study in its own. For a brief review, the reader may for example refer to [94]. Turbulence is closely intertwined with the general concept of fluid mechanics. Almost all flows occurring in nature are turbulent. Examples to give but a few are the flow of water in rivers, the flow in the atmosphere, boundary layers growing around vehicles and aircraft wings, ventilation systems, combustion processes, and mixing processes in general. Thus turbulence forms part of all kinds of everyday processes, which also explains the need for, and interest in, the study of this particular phenomenon.

Turbulent motions take place on a broad range of spatial scales. The largest organized scales of the flow are the scales at which most of the energy resides and are often the scales which exhibit the most discernible structure. These structures are known as the coherent structures of the flow. The existence of coherent structures (CS hereafter) has been appreciated for at least forty years and the level of interest in CS has been growing steadily in that period of time. Figure 1.1 shows an example of CS occurring in the wake created as wind–driven clouds encounter a steep island in the southern Pacific. The image of these very large scale motions was taken from the *Landsat–7* satellite. (For details please refer to the website given in the figure text.) This flow pattern is often referred to as the von Kármán vortex street in tribute to Theodore von Kármán who first explained the physics of this phenomenon. Under the right condi-

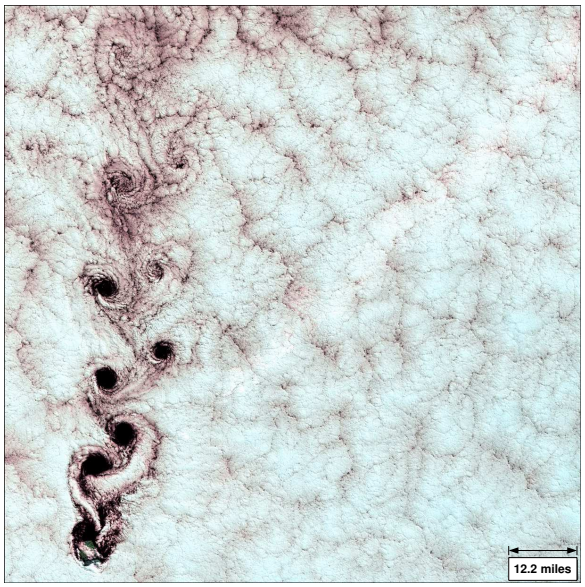

Figure 1.1: *Cloud formations in the wake of Alexander Selkirk Island in the southern Pacific Ocean.* (From http://landsat.gsfc.nasa.gov).

tions, a vortex street forms in the wake of almost all bluff bodies. The most classical example is the cylinder wake flow of which a thorough review can be found in [80].

There are two major reasons for the growing interest in CS. Firstly, as already mentioned, these large scale organized motions are the most energetic structures of the flow. The amount of turbulent energy represented by CS ranges from about 10% for boundary layers up to 25% for the near wake or jet (see e.g. [22]). Secondly, they play an important role in mixing, vibrations, noise emission, and drag and lift. (For an example of the latter see e.g. [81]). For these reasons, the study of CS aiming at control of turbulent flows to influence the parameters mentioned seems obvious.

The vortex street in figure 1.1 is an example of CS clearly visible from the instantaneous flow field. However, since turbulent CS are always embedded in a randomly distributed field, their identification may not always be as straightforward. Hence various detection methods are required. A powerful tool is visualizations which directly show how the otherwise invisible large scale organized structures occur in the flow. Figure 1.1 provides an example of visualization in nature. Typical laboratory techniques are the release of smoke in airflow and injection of dye in water at specific locations. However, as pointed out by Holmes et al. in [36] although visualizations do indeed demonstrate the existence of CS, not much is is gained with respect to the dynamics of these structures. Several other methods are available, most of which are evaluated in the comprehensive paper by Bonnet et al. on testing of eddy structure identification methods [16].

The different techniques are divided into two main categories: conditional and non-conditional. The former are characterized by their dependence on the type of CS considered and a given threshold value. Conditional averaging, for instance, where a sample is taken each time the velocity fluctuation at a given point is above a certain level (or in a certain direction), may lead to the identification of a recurring structure

at that location. Another example of a conditional identification method is actually visualization: the result depends on where in the flow the smoke/dye is injected. Thus a common feature for these conditional techniques is that they involve a certain degree of subjectivity. Only few techniques fall into the second category. The ones known to the present author are space– and time correlations (see chapter 2 of this thesis), spectral analysis [51], and last but not least Proper Orthogonal Decomposition (POD). The strength of these methods are that they are *objective*. No assumptions are made with respect to what is looked for in the flow. Since one of the primary tools used for identification of CS in the present work is the POD, a theoretical description of this technique is given independently. Hence for now the reader is referred to chapter 3 for further details. Some techniques fall into both categories. These are Pattern Recognition [77], wavelets [29], and Linear Stochastic Estimation (LSE). These techniques are characterized by the use of *candidate structures* in the analysis of the flow. For further information on the two first methods the reader may refer to the references given above. The LSE method will also be applied in the present work, hence a description of the theory behind it can be found in chapter 4.

All in all, several methods are available for the detection of CS which each have their strengths and weaknesses. Common for all is their ability to detect CS and yield information about their dynamics and hence contribution to effects of turbulent flow processes such as mixing, drag or heat transfer.

Before analyzing anything, of course a dataset has to be produced. In the present work velocity data is obtained via Particle Image Velocimetry. Hence for completeness, a short introduction to this measurement technique is now given.

1.2 Particle Image Velocimetry

The most well-established measurement techniques in the study of turbulence are the use of hot–wires and Laser Doppler Anemometry (LDA). Under given conditions, these may yield either the time–history or a series of independent realizations of one or more velocity components at a single point in the flow. An extension of these techniques is offered by Particle Image Velocimetry (PIV), which provides information on instantaneous velocities in an entire plane of the flow. Like LDA, PIV is non-intrusive and relies on the presence of seeding particles distributed in the flow to scatter laser light from which the velocities are deduced. However, by providing the velocity at many points simultaneously, PIV facilitates the study of instantaneous flow structures and further greatly reduces the time necessary to obtain statistical quantities such as the mean velocity field and turbulent kinetic energy.

The basic principle of PIV is the simplest imaginable. The velocity is given as a displacement divided by the corresponding time separation, i.e. for a single realization:

$$\mathbf{u}(\mathbf{x}) = \frac{\Delta \mathbf{X}(\mathbf{x})}{\Delta t}$$

where $\mathbf{u}$ denotes the velocity defined on the (measuring) domain $\{\mathbf{x} \in \Omega\}$, $\Delta \mathbf{X}$ is the displacement vector, and Δt the time separation. In practice, two images are taken with short time separation of a plane of the flow illuminated by a laser light-sheet. The field-of-view is divided into a number of interrogation areas (IAs) each containing a

number of particle images from the scattered laser light. Cross–correlation of the two images yields the local displacements and finally, dividing by the time separation, the instantaneous velocity field results.

A number of different parameters have to be optimized in order to produce good PIV data. Useful guidelines are given in [64] and some of the aspects are briefly discussed in connection with the applications to be presented in the following parts of this thesis. However, four basic design rules of general interest should be stated here. These rules, initially proposed by Keane and Adrian [41], pertain to optimal performance of double–pulsed planar PIV measurements using standard cross–correlation analysis[1]. The rules are stated as follows:

- Image density, $N_I \geq 10$–15
- In-plane displacements, $|\Delta X| \leq 0.25 D_I$
- Out-of-plane displacements, $|w|\Delta t < 0.25 z_0$
- Spatial gradients, $M|\Delta \mathbf{u}|\Delta t / D_I < 5\%$

Here D_I denotes the IA side length and z_0 the laser-sheet thickness. The magnification factor, M is given as the ratio of the distance between the image plane (CCD chip) and the camera lens and the lens and the object (measuring) plane (see e.g. [71]). In practice, M is determined as the side length of the CCD chip divided by the side length of the object plane. The image density, N_I, gives the number of particle image pairs of the successive recordings within an IA. A high number of particle pairs gives a higher probability of correctly determining the displacement. Following this criterion, it is clear that a high seeding density permits the use of smaller IAs and hence a better spatial resolution of the flow field. However, too much seeding may result in insufficient light intensity or overlapping of the individual particle images. In the latter case one speaks of Laser Speckle Velocimetry. Conversely, when the seeding density is very low, distinct particles may be tracked from one image to the next, and the technique known as Particle Tracking Velocimetry may be applied. For a discussion of these different cases see also [71]. The restrictions on the in- and out-of-plane displacements are obvious in the sense that if the time separation is too large, all the particles in an IA of the first image will have left this IA in the second image and then the cross–correlation will no longer make sense. A small time separation gives a large dynamic spatial range (DSR), which indicates that a large number of independent vectors can be measured across the field-of-view, i.e. a better resolution can be obtained. (For a strict definition of DSR see [2]). It should be noted however, that Δt can not be chosen arbitrarily small, as this would result in enhanced relative errors on the final result. Thus, a trade-off between accuracy and resolution is necessary in general. Finally, the restriction on the spatial gradients in the flow states that the variation of the velocity across an IA should not exceed 5%. Again, a reasonable requirement since a more or less uniform velocity within each IA must be required for the analysis to make sense.

[1] The second requirement, and to some extent the first one, may be relaxed using *adaptive correlation*, where the IAs of the second image are displaced by the local velocities. See chapters 5 and 9 for further details.

As mentioned, these design rules were first proposed by Keane and Adrian [41]. The contributions of R.J. Adrian in the development of the PIV technique are numerous. In fact, one of the very first papers to mention PIV is his work from 1984 in the journal of *Applied Optics* [5]. A paper of paramount importance is the *Theory of cross–correlation analysis of PIV images* by Keane and Adrian from 1992 [42]. Further, a review was given by Adrian on particle imaging techniques in general in 1991 [4]. Other groundbreaking work include the paper by Willert and Gharib from 1990 [96] and the Ph.D. dissertation of Westerweel from 1993 [88] which has been followed by several papers including [87, 90] and [91].

A natural extension of PIV is Stereoscopic Particle Image Velocimetry (SPIV). Using two cameras placed at given angles to the object plane, this technique makes it possible to determine all three velocity components in the plane considered. SPIV was used to obtain the data investigated in part C of this thesis and a short description of its features will be given there. Instructive papers on SPIV include the work of Prasad and Adrian from 1992 [68] and the review by Prasad from 2000 [70].

On the face of it, PIV seems to be the perfect tool for experimental fluid mechanics, but of course it also has its limitations. Until now, the prime limitation has been its inadequacy to provide temporally resolved data, because the huge amount of information stored with each image limits the speed with which the images can be acquired. The maximum acquisition rate of the PIV system used in the present work is 10 Hz, which, in fact, was enough to obtain several images of the same flow structures in the first flow case considered (see part B). Evidently, this acquisition rate would never be enough though, to determine the smallest time scales of the flow. (For a discussion of length and time scales please refer to chapter 2). However, PIV is still undergoing tremendous development both theoretically and hardwarewise. High speed acquisition systems are emerging and, at present, data rates of the order of 1 kHz are possible. Further, the extension to full 3D fields where all three velocity components are determined in a *volume* of the flow is under development. This technique has been labeled *holographic PIV* (see e.g. [28]).

To sum up, PIV is one of the most efficient tools in experimental fluid mechanics today, and it is still developing. Two and three velocity components for statistical analysis may be obtained in planes of the flow in a short period of time and the acquisition of whole–field instantaneous velocity fields facilitates the study of coherent flow structures. Especially the latter makes PIV the obvious choice for the investigations presented in this thesis.

1.3 The present work

Before outlining the contents of the dissertation, a few introductory comments are now given on the subjects to be addressed. Apart from the initial theoretical description, the following three flow cases are considered:

Ventilation problem

The Annex 20 room, due to Nielsen [61], is a standard measure room which is used for investigation of ventilation problems and indoor environment. In the present work a

scale model using water as fluid was constructed to facilitate measurements with PIV. The objectives of this study were to:

- Record and process PIV data to obtain uncorrelated and temporally resolved velocity data in a plane of the Annex 20 room near the flow inlet
- Investigate the interaction of the dominant flow structures using Proper Orthogonal Decomposition
- Apply Linear Stochastic Estimation to reproduce dominant flow structures and compare with the results of the POD analysis

Jet-in-crossflow

The jet-in-crossflow (JICF) is of great importance to mixing processes in general. For instance it is encountered in processes such as fuel injection and issuing of smoke from a chimney into the atmosphere. The JICF was modeled in the laboratory by issuing a jet perpendicularly into a uniform channel flow. The objectives of the study were to:

- Obtain uncorrelated data for all three velocity components applying SPIV in mutually perpendicular planes in the near field of the JICF
- Describe instantaneous and mean quantities and compare with previous results
- Carry out POD analyses in the different planes to investigate the dominant flow structures of the near field of the JICF

Free turbulent jet

Like the JICF, the free axisymmetric turbulent jet is of importance to mixing processes. Also, the general interest in the basic properties of flows with turbulent/non–turbulent interfaces has given rise to many investigations of the free turbulent jet. In the present studies, simultaneous PIV and LIF[2] data recorded by Fukushima et al. [31] were analyzed with the purposes of:

- Getting acquainted with processing of PIV and LIF data via non–commercial software
- Derive statistical properties of the free turbulent jet relative to the turbulent/non–turbulent interface

1.4 Outline of the thesis

In the present chapter, an introduction to the concept of coherent structures has been given. Also the basic ideas behind PIV and a few general guidelines on the application of this measurement technique were presented. The rest of the thesis is organized as follows.

[2]Laser Induced Fluorescence. For a brief description of this technique please refer to the part in question, i.e. part D, of the present work.

Part A, consisting of chapters 2–4, provides a theoretical framework for the investigations to be presented in the flow cases considered in parts B through D. Chapter 2 gives a general overview of the equations governing fluid flows as well as a discussion of some of the most important quantities in turbulence analysis. The following two chapters present a theoretical description of POD and LSE with a discussion of the physical interpretation of the outcome of these analysis techniques.

Part B comprises the results of the measurement and analysis of PIV data in the scale model of the Annex 20 room. Chapter 5 consists of a journal paper focusing on POD analysis and the following chapter presents an investigation of the length scales of the flow and the results of application of LSE.

Part C presents the investigations of the jet-in-crossflow. First a chapter is devoted to a short introduction to the JICF together with a description of the experimental setup and the concepts of SPIV. The second chapter presents the results of the investigations, yielding a comprehensive picture of the physics of the jet-in-crossflow.

In the fourth and last part of the thesis, results from an analysis of simultaneous PIV and LIF measurements of a free axisymmetric turbulent jet are presented. The analysis includes derivation of statistical quantities as a function of the distance to the jet boundary.

Finally, chapter 10 summarizes the main results and conclusions of the thesis and discusses possible topics for future investigations.

Part A

Theory

Chapter 2

General Concepts of Turbulence

The theory of turbulence includes an enormous amount of literature and a complete review would be way beyond the scope of this thesis. However, some of the most basic equations and definitions along with their physical significance should be introduced for completeness. In the following chapters, a little more space will be devoted to the description of POD and LSE, which are the primary tools used for the investigations in the present work.

2.1 The governing equations

A major breakthrough in fluid mechanics was the birth of the Navier–Stokes (NS) equations, which were formulated independently by Navier and Stokes in 1823 and 1845, respectively. A full derivation of these equations can be found in [94]. In their simplest form, leaving out body forces and assuming incompressible flow and constant viscosity, they read:

$$\frac{\partial u_i}{\partial t} + u_j \frac{\partial u_i}{\partial x_j} = -\frac{1}{\rho}\frac{\partial p}{\partial x_i} + \nu \frac{\partial^2 u_i}{\partial x_j \partial x_j} \tag{2.1}$$

where the summation convention has been used, and where $\nu = \mu/\rho$ denotes the kinematic viscosity and ρ is the density of the fluid. The indices run over $i, j = 1, 2, 3$, corresponding to the three coordinate directions (x, y, z) with velocity components (u, v, w). The second term on the left–hand side represents the non-linear convection of momentum by the flow, which is of great importance to turbulence. The terms on the right–hand side account for pressure and viscous forces, respectively. Equation (2.1) may also be written on a more compact form to obtain a single vector equation with $\mathbf{V} = [u\ v\ w]^T$ as

$$\frac{D\mathbf{V}}{Dt} = -\frac{\nabla p}{\rho} + \nu \nabla^2 \mathbf{V} \tag{2.2}$$

where the *particle* or *substantial derivative*

$$\frac{D}{Dt} = \frac{\partial}{\partial t} + (\mathbf{V} \cdot \nabla)$$

and the differential operator

$$\nabla = \left[\frac{\partial}{\partial x}\ \frac{\partial}{\partial y}\ \frac{\partial}{\partial z}\right]^T$$

have been introduced.

Supplementing these equations is the equation of conservation of mass, also known as the *continuity equation*, which reads, in the case of incompressible flow:

$$\frac{\partial u_i}{\partial x_i} = \frac{\partial u}{\partial x} + \frac{\partial v}{\partial y} + \frac{\partial w}{\partial z} = 0 \tag{2.3}$$

Given a domain of interest with suitable initial and boundary conditions, equations (2.1) and (2.3) constitute a system of four equations with four unknowns, namely u, v, w, and p. Unfortunately it seems that this system can not be solved analytically except in few extensively simplified cases. Still, as will be described in the following, some manipulation can be performed which leads to the creation of very useful quantities in the study of turbulence.

2.2 Characteristic quantities

2.2.1 The Reynolds number

Often the NS equations are made non-dimensional by dividing the individual variables by quantities characteristic of the flow under investigation. Thus, denoting a typical length scale by L and a characteristic velocity by V, non-dimensional variables are introduced as follows:

$$x_i^* = x_i/L,\ u_i^* = u_i/V,\ p^* = p/(\rho V^2)$$

Dropping the asterisks for brevity, equation (2.1) may then be rewritten to yield:

$$\frac{\partial u_i}{\partial t} + u_j\frac{\partial u_i}{\partial x_j} = -\frac{\partial p}{\partial x_i} + \frac{1}{Re}\frac{\partial^2 u_i}{\partial x_j \partial x_j} \tag{2.4}$$

where all quantities are now dimensionless. The non-dimensional form of the continuity equation is identical to (2.3). The procedure gives rise to the Reynolds number which is defined as

$$Re = \frac{VL}{\nu} \tag{2.5}$$

This dimensionless parameter is fundamental to the classification of a given flow. With velocity and viscosity appearing in the numerator and denominator, respectively, it represents the ratio of inertia forces to viscous forces in the flow, which is a good indicator of whether a given flow is laminar or turbulent. Osborne Reynolds in 1883 was the first to observe the connection between the size of the Reynolds number and qualitative flow behavior, hence the name of this quantity. For a summary of Reynolds' studies, one may refer to the introductory chapter of the book on hydrodynamic stability by Drazin and Reid [26]. Since the variables in equation (2.4) are all non-dimensional, it is

also seen that for the same value of Reynolds number the equation describing the flow is exactly the same whatever the values of V, L, and ν. Hence, as long as geometric similarity is met, scale models may be used to investigate the flow pattern of a given problem, by varying the velocity and/or viscosity. This convenient fact is utilized constantly in the study of fluid mechanics, and a current example can be found in part B of the present thesis.

2.2.2 Averaging

A common approach in dealing with the NS equations is the so-called Reynolds decomposition. Assuming that a statistically stationary mean flow exists, the velocities are split into a mean and a fluctuating part as follows:

$$u_i = U_i + u_i' \tag{2.6}$$

where $U_i = \langle u_i \rangle$ is the time or ensemble average of u_i, and $\langle u_i' \rangle = 0$. When a stationary mean flow exists, time and ensemble averages become identical. In the following, ensemble averaging is assumed. This type of averaging can always be performed. For a discussion of averages see e.g. [36] (p. 28). A similar decomposition is introduced for the pressure. Inserting these expressions in equations (2.4) and (2.3) and averaging, a system of equations governing the steady mean flow is obtained:

$$U_j \frac{\partial U_i}{\partial x_j} + \frac{\partial}{\partial x_j} \langle u_i' u_j' \rangle = -\frac{\partial P}{\partial x_i} + \frac{1}{Re} \frac{\partial^2 U_i}{\partial x_j \partial x_j} \tag{2.7}$$

$$\frac{\partial U_i}{\partial x_i} = 0 \tag{2.8}$$

where in the first equation P denotes the mean pressure and it has been utilized that continuity implies that

$$u_j' \frac{\partial u_i'}{\partial x_j} = \frac{\partial u_i' u_j'}{\partial x_j}$$

Equation (2.7) is a simplified[1] non-dimensional form of the *Reynolds momentum equation*. The system contains an unknown term in the form of $\langle u_i' u_j' \rangle$, i.e. the mean value of the product of the fluctuating part of the velocities. Modeling of this term in order to make the system solvable is a science in itself and has given rise to many so-called turbulence closure models for CFD. A thorough review of these can be found in Wilcox' *Turbulence Modeling for CFD* [95].

The term is related to the *Reynolds stress*, which (on dimensional form) is formally defined as (see [82]):

$$\tau_{ij} = -\langle \rho u_i' u_j' \rangle \tag{2.9}$$

This tensorial quantity is of great importance in any turbulent flow, as its elements represent the normal and shear stresses acting in the flow. Especially the latter are

[1] Due to the assumption of constant viscosity. For the full version, the reader is referred to Tennekes and Lumley's *A First Course in Turbulence* [82].

important because of their dominant role in the contribution to the transport of mean momentum. The former, given as the diagonal elements of τ_{ij}, represent the extra pressure contribution due to the turbulent motion. For constant density these are exactly $-\rho$ times the square of the well-known RMS–values of the three velocity components at a given point. The sum of the square of the RMS–values defines the *turbulent kinetic energy*:

$$K = \frac{1}{2}\langle u_i' u_i' \rangle \tag{2.10}$$

Non–dimensionalizing by the square of a characteristic mean velocity, this quantity is often used as a measure for the turbulence intensity of the flow. An equation may be derived for the turbulent kinetic energy which defines four major contributions to the rate of change of K (see e.g. [94]). Of these the two most dominant terms account for the production and viscous dissipation, respectively. Accordingly, the following quantities are normally defined:

$$\mathcal{P} = -\langle u_i' u_j' \rangle \left(\frac{\partial U_i}{\partial x_j} + \frac{\partial U_j}{\partial x_i} \right) \tag{2.11}$$

$$\epsilon = 2\nu \langle s_{ij} s_{ij} \rangle \tag{2.12}$$

Where the fluctuating rate of strain

$$s_{ij} = \frac{1}{2} \left(\frac{\partial u_i'}{\partial x_j} + \frac{\partial u_j'}{\partial x_i} \right)$$

has been introduced for convenience. As mentioned, these quantities are important to the rate of change of turbulent kinetic energy. The viscous dissipation is of particular importance to turbulence theory since it is related to the smallest scales of turbulence.

2.2.3 Correlation and scales

The most important classical statistical quantities in the analysis of turbulent flows are perhaps the correlation functions. Two types of correlations can be calculated: temporal and spatial. Considering a fixed location in space, the time correlation coefficients can be written as:

$$\rho_{ij}(\tau) = \frac{\langle u_i'(t) u_j'(t+\tau) \rangle}{\langle u_i'(t) u_j'(t) \rangle} \tag{2.13}$$

where the indices denote what components are considered (no summation implied). In a typical situation where the main flow is in the x–direction, the most obvious coefficient to consider is ρ_{11} which gives the *autocorrelation coefficient* for u. At zero time separation the coefficient equals one. Theoretically, as τ approaches infinity it goes to zero. However, in practice, some oscillation about the τ–axis must be expected due to the errors associated with experiments or numerical calculations. Integrating the autocorrelation coefficient from zero to infinity, the *integral time scale* is obtained. Physically, this quantity represents the average time it takes for a flow structure to

pass by the point at which the autocorrelation has been constructed. Or put in another way: as long as the fluid that passes through a given point belongs to the same structure, the velocity at that point is correlated with the velocity that was there at the time of arrival of the structure. The integral time scale plays an important role in experiments where uncorrelated samples are often desired. In practice the dead–time between measurements is set to twice the integral time scale to make sure that the measurements are uncorrelated.

The elements of the two–point space–correlation tensor are given as the ensemble average of the products of the fluctuating part of the velocities at different spatial locations. Denoting one point in space by $\mathbf{x}$ and another by $\mathbf{x}'$ it can be written

$$R_{ij}(\mathbf{x}, \mathbf{x}') = \langle u_i'(\mathbf{x}) u_j'(\mathbf{x}') \rangle \tag{2.14}$$

Or on matrix form, which will be preferred in the remainder of this thesis

$$\mathbf{R}(\mathbf{x}, \mathbf{x}') = \langle \mathbf{u}(\mathbf{x}) \mathbf{u}^T(\mathbf{x}') \rangle \tag{2.15}$$

where the primes indicating fluctuating part of the velocity have been dropped for the sake of readability.

The two–point correlation tensor turns out to be of paramount importance to both the Proper Orthogonal Decomposition and Linear Stochastic Estimation, with which the following chapters are concerned. The explanation for this is that it is closely related to the size of the coherent flow structures appearing in the flow. Just as in the case of the autocorrelation, the first element of the space correlation tensor at a given point may be normalized by the square of the local RMS–value of u. Integrating the resulting space correlation coefficient gives the *macro scale* of turbulence, which may be directly interpreted as the length scale of the coherent structures at that location.

Other length scales of interest in the study of turbulence are the Kolmogorov microscale, the smallest scale of turbulence at which dissipation takes place, and the intermediate Taylor microscale. Physically, the latter represents the scales below which "very good correlation" is found, i.e. where the spatial correlation coefficient is close to one. Hence, in practical experiments, resolving the Taylor microscale corresponds to a good spatial resolution of the flow field. As already mentioned, the focus in the present work will be on the large–scale coherent structures of turbulence, hence a further discussion of the small scales will not be given here. The interested reader may refer to chapter nine of [7].

2.3 Vorticity

The one single feature which comes closest to a definition of turbulence is the presence of high levels of fluctuating vorticity. Hence a short introduction to the role of vorticity in turbulence should also be given.

The vorticity is defined as the curl of the velocity:

$$\boldsymbol{\omega} = \nabla \times \mathbf{V} \tag{2.16}$$

Being equal to twice the angular velocity, $\boldsymbol{\omega}$ provides a measure of the rotation of a fluid element as it moves in the flow field. An equation governing the time evolution of

the vorticity can be found by applying the curl operator to the NS equations. Adopting the notation from equation (2.1) the result becomes:

$$\frac{\partial \omega_i}{\partial t} + u_j \frac{\partial \omega_i}{\partial x_j} = \omega_j \frac{\partial u_i}{\partial x_j} + \nu \frac{\partial^2 \omega_i}{\partial x_j \partial x_j} \tag{2.17}$$

(The pressure term disappears due to the basic rules of calculus, stating that the curl of the gradient is identically zero.)

The terms in (2.17) can be interpreted as follows. The second term on the left–hand side represents the convection of vorticity by the velocity field. Also arising from the convective terms in (2.1) is the first term on the right–hand side. This term represents the amplification and rotation of the vorticity vector by the strain rate [82]. The most important of the two is the amplification, which is related to the *stretching* of vorticity. For this reason the term is also often referred to as the stretching term. The last term in the equation is referred to as the viscous diffusion term (see [52]) since, in the absence of convection and stretching, equation (2.17) simply reduces to the diffusion equation. By virtue of definition, stretching of vorticity only occurs in 3D flows. It is of great importance to turbulence in general and, in particular, the stretching of vorticity fluctuations may be shown to be associated with the generation of Reynolds stress [82]. The so-called *energy cascade*, describing the transfer of energy from large eddies to small eddies, is also an effect of vortex stretching; the scale of the eddies decreases as they are stretched. For a more thorough description of these issues the reader may refer to chapter three of [82].

The concept of vorticity is of considerable interest in the context of identification of coherent structures. To illustrate this, figure 2.1 shows a vector plot of the fluctuating

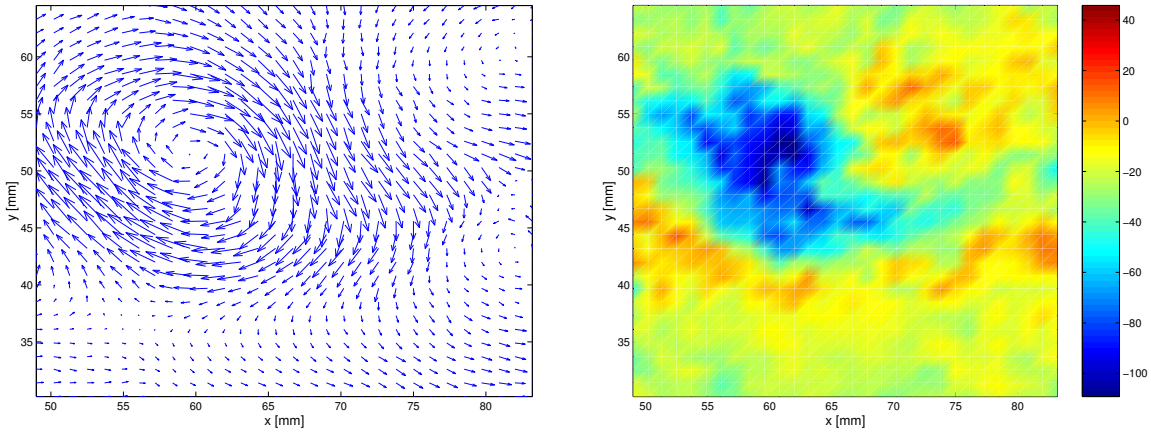

Figure 2.1: *Left: vortex structure revealed by subtraction of local mean velocity. Right: associated vorticity contours.*

part of an instantaneous flow realization and the associated vorticity contours. The subtraction of the local mean velocity reveals a vortical structure centered at $(x, y) \approx (60, 50)$ mm in the coordinate system considered. Comparing with the contour plot on the right, it is seen that a vorticity maximum is found near the vortex center and that the level of vorticity decreases away from this location. Now, imagine that the

instantaneous flow realization corresponding to this fluctuating flow field is available (e.g. from a PIV snapshot), but that the local mean velocity is not known. This is illustrated by the left plot in figure 2.2 where arbitrary constants have been added to the two velocity components. The plot on the right shows the associated vorticity

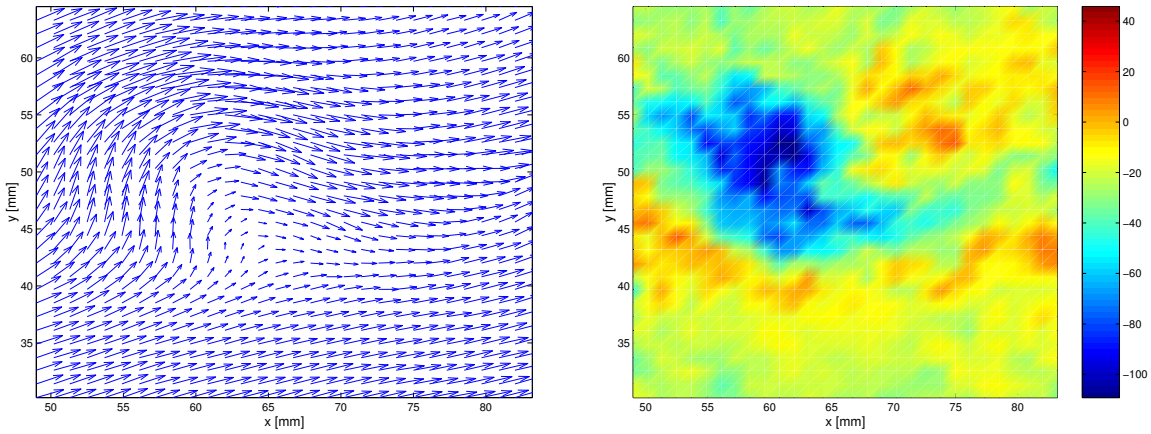

Figure 2.2: *Left: instantaneous flow realization corresponding to the fluctuating field shown in figure 2.1. Right: associated vorticity contours.*

contours. The vortical structure is no longer visible from the velocity field, but the vorticity contours still reveal the presence of a vortex at $(x, y) \approx (60, 50)$ mm.

Thus, vorticity contours can be used to identify "hidden" turbulent vortex structures in a flow field. Care should be taken however, as high levels of vorticity are found both in connection with swirling motion and shearing motion. An example is seen in the figures above where the strong velocity gradients to the right of the vortex also create a local peak in vorticity. Hence a vorticity maximum does not necessarily indicate the presence of a vortex. Various methods have been suggested to overcome this restriction. For full 3D data fields Hunt et al. introduced the so-called Q–criterion, where Q is defined as the difference between the square (inner product) of the antisymmetric and the symmetric part of the gradient tensor [37]:

$$Q = \Omega_{ij}\Omega_{ij} - S_{ij}S_{ij} \tag{2.18}$$

with

$$\Omega_{ij} = \frac{\partial u_i}{\partial x_j} - \frac{\partial u_j}{\partial x_i} \quad \text{and} \quad S_{ij} = \frac{\partial u_i}{\partial x_j} + \frac{\partial u_j}{\partial x_i}$$

In this way, high positive values of Q identify regions where the rotation rate dominates the strain rate. The technique was implemented and extended by Dubief and Delcayre in [27]. A related technique is provided by the λ_2 criterion [38], which identifies local pressure minima due to vortical motion only. A simplified version of this technique applies for 2D data, which makes it suitable for analysis of PIV data.

Finally the sum of the mean square of the vorticity fluctuations should be mentioned. Defining Z as:

$$Z = \frac{1}{2}\langle \omega_i' \omega_i' \rangle \tag{2.19}$$

this quantity, often referred to as the *enstrophy*, represents the turbulent "energy" of the vorticity. Deriving equations for $\langle \omega_i' \omega_i' \rangle$ and the square of the mean vorticity, Tennekes and Lumley showed how these quantities interact to account for the dynamics of vorticity in turbulent flows in general [82]. Furthermore they showed, how the mean square of the vorticity fluctuations may be directly associated with the dissipation of turbulent kinetic energy, ϵ (see section 2.2).

2.4 Summary

The present chapter has provided an introduction to some of the general concepts underlying the study of turbulence. First the governing equations were presented, and it was shown how the very essential Reynolds number arises from non–dimensionalization of these equations. Averaging of the governing equations was shown to lead to characteristic quantities of turbulence such as the Reynolds stress tensor and the turbulent kinetic energy, and it was remarked how an equation governing the latter gives rise to the important quantity of viscous dissipation. Thirdly, through the definition of time– and space correlations, it was discussed how these parameters relate to the time and length scales of turbulence, and the relevance of the two–point space–correlation tensor to POD and LSE was noted. Finally, the equation governing the evolution of vorticity was presented, and it was shown how the concept of vorticity is of interest in connection with identification of coherent structures. Also the important role of vorticity to the dynamics of turbulence in general was pointed out.

Chapter 3

Proper Orthogonal Decomposition

As the application of the POD comprises a large part of the investigations in this thesis, a relatively comprehensive description of this technique will now be provided. The chapter is introduced with a historical review discussing earlier applications and presenting the two main versions of the POD. Second, the basic equations are derived and the features of these two versions are discussed in relation to the nature of the dataset to be analyzed. Third, a detailed description of how to apply the POD in practice is given, before finally some comments are made on how to interpret the results of a POD analysis.

3.1 Historical review

While being introduced to the fluid mechanics society by John L. Lumley [50] already in 1967, the application of the Proper Orthogonal Decomposition (POD) has become quite frequent in the course of the last fifteen years and it is today a well established tool in the analysis of inhomogeneous turbulent flows. The technique itself was already known at the time from probability theory where Loève [48] was the first to provide a rigorous description[1]. The incentive for Lumley was the need for a formal definition of the important large scale structures observed in turbulent shear flows, described as "big eddies" by Townsend [83]. The phenomena now known as coherent structures (see section 1.1). Although Lumley is said to be the first to present the POD in this context, it had, in fact, already been applied earlier for studies of atmospheric turbulence (see discussion by A.M. Yaglom at the end of [50]). However, providing a description within an established theoretical framework, the work of Lumley was quite unique and, as it turned out, has been invaluable for the application of POD in fluid mechanics ever since.

Using the new technique Payne and Lumley [63] investigated the wake of a circular cylinder and Bakewell and Lumley [10] studied the boundary layer of turbulent pipe flow. Apart from these publications, little attention seems to have been paid to POD in the years to follow. In 1984 Moin [58] used the ideas of Lumley in Large Eddy Simulation and the year after Glauser et al. [34] used POD to analyze the axisymmetric jet mixing layer.

[1] The POD is also often referred to as the Karhunen-Loève decomposition (or expansion).

The next milestone in the application of POD to turbulence was not placed until 1987 when Sirovich [79], based on the original work of Lumley, suggested an alternative approach named *the method of snapshots*. From henceforth the method of snapshots will be referred to as "snapshot POD", whereas the original approach will be labeled "classical POD". For a detailed description of the two approaches the reader is referred to the following section, where the basic equations are derived. For now it suffices to mention that the two methods supplement each other nicely with regard to optimizing the computational effort required when applying the POD to a given dataset.

From about that time, the application of POD became a more and more frequent topic in the study of fluid mechanics and numerous publications emerged both employing the snapshot and the classical POD. An admirable piece of work involving the classical POD was published in the Journal of Fluid Mechanics by Aubry et al. [8] in 1988. Also applying the classical POD, the following year Moin and Moser [57] extracted the coherent structures of turbulent channel flow from a dataset generated from a direct numerical simulation by Kim et al. [44]. Extending the original ideas, the biorthogonal decomposition was presented by Aubry in 1991 [9]. Application of the classical POD for studying the organized structures in shear layers was described by Delville [24], a precursor to the more extensive analysis presented by Delville et al. [25] in 1999. A comment on the implications of POD on low-dimensional modeling of dynamical system was given by Rempfer [75] in 2000 and the same year Citriniti and George [21] applied the classical POD for reconstruction of the global velocity field in their elaborate studies of the mixing layer of the axisymmetric jet. Recent applications of the classical POD can be found in [39] and [32], where the axisymmetric wake and jet were studied, respectively.

Working with Sirovich some of the first applications of the snapshot POD after 1987 were presented by Kirby et al. [45] and Winter et al. [97] who considered axisymmetric jet flow and turbulent mixing, respectively. An interesting application investigating transition in a rotating flow using the snapshot POD was presented by Christensen et al. [19] in 1993. A continuation of this work was presented by the same authors a few years later, where two modified approaches namely the *weighted POD* and the *predefined POD* were suggested [18]. Pursuing the same ideas, a thorough investigation considering a more complex flow configuration was made by Jørgensen [40] in his thesis which was finished in 2000. More recently Bérengère and Le Quéré [12] investigated a differentially heated cavity by including temperature fluctuations in the analysis, and Pelliccia-Kraft and Watt [67] applied the snapshot POD to scalar fields of unsteady jet flow. Finally, the application of *extended POD* using a modified version of the snapshot POD was presented by Maurel et al. [53] in 2001. A paper of which J.L. Lumley can be found among the co-authors.

Apart from the fluid mechanics applications, it can be mentioned that Sirovich has also utilized the snapshot POD in other areas of science. Among this work some of the most interesting is perhaps the characterization of human faces [46] and the study of heart activity as recorded by echocardiography [78].

Although providing a far from complete list, the work referred to above gives an idea of the powerfulness of the POD in the study of fluid mechanics. The focus has been on actual applications. As for reviews on POD, one of the most well-known was provided by Berkooz et al. [13] in 1993. A review together with a thorough theoretical

description is found in the book by Holmes et al. [36], who also discuss the implications of POD in the theory of turbulence in general. Further, a useful overview is provided by the recent lecture notes by Cordier and Bergmann [22, 23]. The latter divide the application of POD in fluid mechanics into two main categories both of which are well represented among the work mentioned above. These are: 1) the eduction of coherent structures, and 2) low-dimensional modeling. As pointed out in the introduction, the focus in the present thesis will be on the application concerning investigation of coherent flow structures.

3.2 Basic equations

3.2.1 Classical POD

Put in words, the original ideas of Lumley ([50]) may be summed up as follows: "considering a random vector field, an equation is derived by projecting this field onto a candidate structure and determine to what extent the two are parallel in an average sense. Applying calculus of variations, an equation for the candidate structure results, whose solution constitutes the POD basis." Thus, in early derivations no assumption was made about the nature of the vector field or the averaging procedure (see [50, 49]). In the following focusing on the problem at hand, i.e. fluid mechanics, the vector field is a velocity field and ensemble averaging is applied. As a consequence of the latter, the basis modes derived are restricted to the spatial domain.

For convenience, the following notation will be adopted for the L^2 inner product and norm (see e.g. [65]):

$$(\mathbf{f}, \mathbf{g}) = \int_{\mathcal{D}} \mathbf{f}(\mathbf{x})\mathbf{g}^*(\mathbf{x})d\mathbf{x} \tag{3.1}$$

$$\|\mathbf{f}\| = (\mathbf{f}, \mathbf{f})^{\frac{1}{2}} \tag{3.2}$$

The vector functions, $\mathbf{f}$ and $\mathbf{g}$, are defined on the domain $\mathcal{D}$, ($\mathbf{x} \in \mathcal{D}$) and the asterisk indicates complex conjugation.

As mentioned, in fluid mechanics the random vector field is of course the velocity field, which is a function of space and time. More specifically, since the objective of the investigation is turbulence, what is considered is the fluctuating part of the velocity field. Denoting this by $\mathbf{u} = \mathbf{u}(\mathbf{x}, t) = \mathbf{u}(x, y, z, t)$ and the candidate basis function by $\mathbf{\Phi} = \mathbf{\Phi}(\mathbf{x})$ the quantity to optimize can then be written:

$$\frac{\langle |(\mathbf{u}, \mathbf{\Phi})|^2 \rangle}{\|\mathbf{\Phi}\|^2} = \lambda \tag{3.3}$$

where the angle brackets denote ensemble averaging. Following Lumley [49], the kernel theorem allows expression (3.3) to be rewritten in the following form[2]:

$$\frac{(\mathbf{R}(\mathbf{x}, \mathbf{x}'), \mathbf{\Phi}(\mathbf{x})\mathbf{\Phi}^*(\mathbf{x}'))}{(\mathbf{\Phi}(\mathbf{x}), \mathbf{\Phi}(\mathbf{x}))} = \lambda \tag{3.4}$$

[2]The analysis of Lumley was carried out with generalized functions, where the present analysis is restricted to projection of a velocity field. Further, a somewhat more modern notation is used.

where $\mathbf{R}(\mathbf{x},\mathbf{x}')$ is the two-point space-correlation tensor, defined as:

$$\mathbf{R}(\mathbf{x},\mathbf{x}') = \langle \mathbf{u}(\mathbf{x})\mathbf{u}^T(\mathbf{x}') \rangle \tag{3.5}$$

Now, in order to apply calculus of variations suppose that $\mathbf{\Phi}(\mathbf{x})$ does maximize (3.3). Introducing a perturbation by considering the solution $\mathbf{\Phi}(\mathbf{x}) + \epsilon\mathbf{\Upsilon}(\mathbf{x})$ it then has to be shown that the resulting expression has a true maximum for $\epsilon = 0$ for all $\mathbf{\Upsilon}(\mathbf{x})$. Thus, inserting the perturbed solution and setting the first derivative with respect to ϵ equal to zero the following equation results (for the sake of readability the calculations have been placed in appendix A):

$$(\mathbf{R}(\mathbf{x},\mathbf{x}'), \mathbf{\Upsilon}(\mathbf{x})\mathbf{\Phi}^*(\mathbf{x}')) = \lambda(\mathbf{\Phi}(\mathbf{x}), \mathbf{\Upsilon}(\mathbf{x})) \tag{3.6}$$

Rewriting the left hand side of (3.6) yields:

$$((\mathbf{R}(\mathbf{x},\mathbf{x}'), \mathbf{\Phi}^*(\mathbf{x}')), \mathbf{\Upsilon}(\mathbf{x})) = \lambda(\mathbf{\Phi}(\mathbf{x}), \mathbf{\Upsilon}(\mathbf{x}))$$

$$\Leftrightarrow \qquad ([(\mathbf{R}(\mathbf{x},\mathbf{x}'), \mathbf{\Phi}^*(\mathbf{x}')) - \lambda\mathbf{\Phi}(\mathbf{x})], \mathbf{\Upsilon}(\mathbf{x})) = 0 \tag{3.7}$$

For this expression to be valid for all $\mathbf{\Upsilon}(\mathbf{x})$, it must be required that:

$$(\mathbf{R}(\mathbf{x},\mathbf{x}'), \mathbf{\Phi}^*(\mathbf{x}')) = \lambda\mathbf{\Phi}(\mathbf{x}) \tag{3.8}$$

and hence using (3.1) an integral equation for the determination of $\mathbf{\Phi}(\mathbf{x})$ can finally be written:

$$\int_\Omega \mathbf{R}(\mathbf{x},\mathbf{x}')\mathbf{\Phi}(\mathbf{x}')d\mathbf{x}' = \lambda\mathbf{\Phi}(\mathbf{x}) \tag{3.9}$$

where Ω denotes the spatial domain considered, $\{\mathbf{x} = (x, y, z) \in \Omega\}$.

The fact that $\mathbf{R}(\mathbf{x},\mathbf{x}')$ is symmetric and that the integration domain is bounded leads to a number of useful properties for equation (3.9). These properties which are due to Hilbert–Schmidt theory are referred to as the proper orthogonal decomposition theorem [50] and can be summarized as follows (see also e.g. [20] or [22]). Firstly, a denumerable set of solutions exist:

$$\int_\Omega \mathbf{R}(\mathbf{x},\mathbf{x}')\mathbf{\Phi}^i(\mathbf{x}')d\mathbf{x}' = \lambda^i\mathbf{\Phi}^i(\mathbf{x}) \ , \quad i = 1, 2, \ldots \tag{3.10}$$

These solutions may be chosen mutually orthonormal such that:

$$(\mathbf{\Phi}^j, \mathbf{\Phi}^k) = \delta_{jk} \tag{3.11}$$

As the set formed by the $\mathbf{\Phi}^i$ is complete, it may be used as a basis for expanding the velocity field:

$$\mathbf{u}(\mathbf{x}, t) = \sum_{i=1}^{\infty} a^i(t)\mathbf{\Phi}^i(\mathbf{x}) \tag{3.12}$$

where the coefficients $a^i(t)$ are determined by:

$$a^i(t) = (\mathbf{u}(\mathbf{x},t), \mathbf{\Phi}^i(\mathbf{x})) \ , \quad i = 1, 2, \ldots \tag{3.13}$$

and satisfy:

$$\langle a^i(t) a^{j*}(t) \rangle = \delta_{ij} \lambda^i \tag{3.14}$$

Finally, the eigenvalues, λ^i, are nonnegative and their sum is finite:

$$\lambda^i \geq 0 \ , \quad i = 1, 2, \ldots \tag{3.15}$$

$$\sum_{i=1}^{\infty} \lambda^i < \infty \tag{3.16}$$

One of the most important features of the POD is revealed by calculating the total turbulent kinetic energy of the flow field from the expansion (3.12):

$$\begin{aligned} \int_\Omega \big\langle \mathbf{u}(\mathbf{x},t)\mathbf{u}^*(\mathbf{x},t) \big\rangle d\mathbf{x} &= \int_\Omega \Big\langle \sum_{i=1}^{\infty} a^i(t)\mathbf{\Phi}^i(\mathbf{x}) \sum_{i=1}^{\infty} a^{i*}(t)\mathbf{\Phi}^{i*}(\mathbf{x}) \Big\rangle d\mathbf{x} \\ &= \sum_{i=1}^{\infty} \langle a^i(t) a^{i*}(t) \rangle \int_\Omega \mathbf{\Phi}^i(\mathbf{x}) \mathbf{\Phi}^{i*}(\mathbf{x}) d\mathbf{x} \end{aligned}$$

Which using equation (3.14) and the orthonormality condition (3.11) leads to:

$$\int_\Omega \big\langle \mathbf{u}(\mathbf{x},t)\mathbf{u}^*(\mathbf{x},t) \big\rangle d\mathbf{x} = \sum_{i=1}^{\infty} \lambda^i \tag{3.17}$$

This result shows that the total turbulent kinetic energy of the flow field is given by the sum of the eigenvalues of the POD. Since each λ corresponds to a structure, the interpretation is that the degree to which a structure, $\mathbf{\Phi}^i$ contributes to the total kinetic energy is given by the magnitude of its eigenvalue λ^i. Hence, solving for the largest eigenvalues and corresponding basis functions the most energetic and hence largest structures of the flow can be derived from the POD.

3.2.2 Snapshot POD

The snapshot POD introduced by Sirovich [79] takes its starting point in an ensemble of uncorrelated flow realizations. Thus the velocity fields considered are written:

$$\mathbf{u}^n = \mathbf{u}(\mathbf{x}, t^n) = \mathbf{u}(\mathbf{x}, n\tau) \ , \quad n = 1, \ldots, N \tag{3.18}$$

with τ sufficiently large (in practice approximately twice the integral time scale). For a large number of samples the two-point space-correlation tensor is well approximated by:

$$\mathbf{R}(\mathbf{x}, \mathbf{x}') = \frac{1}{N} \sum_{n=1}^{N} \mathbf{u}(\mathbf{x}, t^n) \mathbf{u}^T(\mathbf{x}', t^n) \tag{3.19}$$

Now assume that the basis modes may be written in terms of the original data as:

$$\mathbf{\Phi}(\mathbf{x}) = \sum_{i=1}^{N} A(t^i)\mathbf{u}(\mathbf{x}, t^i) \tag{3.20}$$

Inserting (3.19) and (3.20) into the original POD equation, equation (3.9), then yields:

$$\int_\Omega \frac{1}{N}\sum_{n=1}^{N} \mathbf{u}(\mathbf{x}, t^n)\mathbf{u}^T(\mathbf{x}', t^n) \sum_{i=1}^{N} A(t^i)\mathbf{u}(\mathbf{x}', t^i)d\mathbf{x}' = \lambda \sum_{i=1}^{N} A(t^i)\mathbf{u}(\mathbf{x}, t^i) \tag{3.21}$$

which as the integration is only with respect to $\mathbf{x}'$ may be written as:

$$\sum_{n=1}^{N}\left(\sum_{i=1}^{N}\left(\frac{1}{N}\int_\Omega \mathbf{u}^T(\mathbf{x}', t^n)\mathbf{u}(\mathbf{x}', t^i)d\mathbf{x}'\right)A(t^i)\right)\mathbf{u}(\mathbf{x}, t^n) = \lambda\sum_{i=1}^{N} A(t^i)\mathbf{u}(\mathbf{x}, t^i)$$

$$\Updownarrow$$

$$\sum_{i=1}^{N}\left(\frac{1}{N}\int_\Omega \mathbf{u}^T(\mathbf{x}', t^n)\mathbf{u}(\mathbf{x}', t^i)d\mathbf{x}'\right)A(t^i) = \lambda A(t^i) \tag{3.22}$$

Introducing the coefficient vector $\mathbf{A}$

$$\mathbf{A} = [A(t^1)\ A(t^2)\ \ldots\ A(t^N)]^T \tag{3.23}$$

the resulting eigenvalue problem can then be written:

$$\mathbf{CA} = \lambda\mathbf{A} \tag{3.24}$$

where the elements of the matrix $\mathbf{C}$ are given by:

$$C_{jk} = \frac{1}{N}(\mathbf{u}(\mathbf{x}, t^j), \mathbf{u}(\mathbf{x}, t^k)) , \qquad j, k = 1, \ldots, N \tag{3.25}$$

(The superscript "T" has been left out, since the transpose is implicit in the notation for the inner product).

Solving the problem given by (3.24) a complete set of N orthogonal eigenvectors results, $\{\mathbf{A}^i,\ i = 1, \ldots, N\}$. The elements of these eigenvectors may be used in the construction of the POD modes according to (3.20). Normalizing to obtain an orthonormal basis, the final expression for the POD basis then becomes:

$$\mathbf{\Phi}^i(\mathbf{x}) = \frac{\displaystyle\sum_{n=1}^{N} A^i(t^n)\mathbf{u}(\mathbf{x}, t^n)}{\left\|\displaystyle\sum_{n=1}^{N} A^i(t^n)\mathbf{u}(\mathbf{x}, t^n)\right\|} , \qquad i = 1, \ldots, N \tag{3.26}$$

It is clear from the above that the size of the eigenvalue problem depends on the number of snapshots ($\text{rank}(\mathbf{C}) = N$). As a consequence the snapshot POD may provide a huge reduction of the computational costs compared to the classical POD depending on the nature of the flow problem considered. In practice the velocity field is defined on

a discrete domain either from measurements or a numerical computation. Considering for instance an ensemble with two velocity components and 500 snapshots of a domain consisting of 100×100 data points, the size of the discrete eigenvalue problem resulting from the classical POD would be 20000×20000 (= the size of $\mathbf{R}$) while the size of the corresponding snapshot POD problem, given by (3.24), would only be 500×500. Which method to choose in a given situation depends on the problem in question. To exemplify, Delville et al. [25] applied the classical POD to their hot-wire measurements of the mixing layer, an obvious choice due to the limited spatial resolution and the high temporal resolution, while Christensen et al. [19] chose the snapshot POD in their numerical simulations, which were performed at high spatial resolution and where relatively few snapshots were included.

Implications for the present work

The primary experimental tool used to obtain data for the flow cases analyzed in the present work, is PIV. Contrary to other experimental techniques for measuring velocity, PIV is characterized by high spatial resolution and limited temporal resolution. Further, the number of flow realizations which may be sampled in a given experiment is limited due to the large amount of data contained in each snapshot. Hence it is clear that the most feasible method for analyzing PIV data is the snapshot POD and consequently the snapshot POD will be applied for the investigations presented in this thesis.

3.3 Application in practice

The equations derived in the previous section were based on a continuous description (except for the time variable in the snapshot POD). However, as already mentioned, the flow problems encountered in practice are of course discrete, which causes the nature of the equations to change. Hence, for completeness, a description of how the POD is applied in practice is now given.

3.3.1 The data ensemble

Consider a domain (experimental or numerical) of $l \times m$ points. A realization of a given quantity is denoted by $\mathbf{q}^n$:

$$\mathbf{q}^n = [q_1(t^n)\ q_2(t^n)\ \ldots\ q_{lm}(t^n)]^T \tag{3.27}$$

With N snapshots the fluctuating part of the quantity is calculated as:

$$\mathbf{q}'^n = \mathbf{q}^n - \frac{1}{N}\sum_{j=1}^{N}\mathbf{q}^j\ , \quad n = 1, \ldots, N \tag{3.28}$$

Note that until now no assumption has been made about the nature of the ensemble. In principle any thermodynamical property (and combinations hereof) could be included in the POD analysis. In the following, to keep things simple, a 2D velocity field is

considered. Denoting the fluctuating parts by u and v the data may then be organized in a matrix $\mathbf{U}$ as follows:

$$\mathbf{U} = [\mathbf{u}^1 \ \mathbf{u}^2 \ \dots \ \mathbf{u}^N] = \begin{bmatrix} u_1^1 & u_1^2 & \dots & u_1^N \\ \vdots & \vdots & \vdots & \vdots \\ u_{lm}^1 & u_{lm}^2 & \dots & u_{lm}^N \\ v_1^1 & v_1^2 & \dots & v_1^N \\ \vdots & \vdots & \vdots & \vdots \\ v_{lm}^1 & v_{lm}^2 & \dots & v_{lm}^N \end{bmatrix} \tag{3.29}$$

where the subscripts refer to coordinate position and the superscripts indicate snapshot number, i.e. for instance $u_1^1 = u(x_1, y_1, t^1)$.

As revealed by equation (3.29), the size of the data matrix is the product of the number of (velocity) components and the total number of points in the domain times the number of snapshots. In the present case $2lm \times N$. The ordering of the elements in the columns of $\mathbf{U}$ can be chosen quite freely as long as a quantity corresponding to a given position has the same position in each column. Having derived the POD modes, care just has to be taken which element in a given mode corresponds to which coordinate position.

3.3.2 Deriving the POD modes

The discretized versions of equations (3.10) and (3.24) read

$$\widetilde{\mathbf{R}}\boldsymbol{\phi}^i = \lambda^i \boldsymbol{\phi}^i \tag{3.30}$$

and

$$\widetilde{\mathbf{C}}\mathbf{A}^i = \lambda^i \mathbf{A}^i \tag{3.31}$$

Where the two matrices $\widetilde{\mathbf{C}}$ and $\widetilde{\mathbf{R}}$ are now conveniently calculated from the data matrix $\mathbf{U}$ as:

$$\widetilde{\mathbf{R}} = \mathbf{U}\mathbf{U}^T \tag{3.32}$$

and

$$\widetilde{\mathbf{C}} = \mathbf{U}^T\mathbf{U} \tag{3.33}$$

In principle, the latter should be normalized by N. However, the operation is rendered superfluous by the subsequent normalization of the POD modes and hence is left out. Again the difference in size of the two problems is displayed as from the size of $\mathbf{U}$ it follows that: $\text{rank}(\widetilde{\mathbf{R}}) = 2lm$ and $\text{rank}(\widetilde{\mathbf{C}}) = N$. Further the discrete POD modes, $\boldsymbol{\phi}^i$, are now given as vectors of length $2lm$ each element corresponding to a velocity component at a given position.

Solving the two problems and ordering the solutions according to the size of the eigenvalues:

$$\lambda^1 > \lambda^2 > \dots > \lambda^N = 0 \tag{3.34}$$

the POD modes result directly from the normalized eigenvectors of (3.30), while the eigenvectors of (3.31) make up a basis for constructing the POD modes according to equation (3.26). Adopting the notation from equation (3.29) the expression for the discrete POD modes of the snapshot POD thus becomes:

$$\boldsymbol{\phi}^i = \frac{\sum_{n=1}^{N} A_n^i \mathbf{u}^n}{\left\| \sum_{n=1}^{N} A_n^i \mathbf{u}^n \right\|}, \qquad i = 1, \ldots, N \tag{3.35}$$

Where A_n^i is the n'th component of the normalized eigenvector corresponding to λ^i and the discrete 2–norm is defined as

$$\|\mathbf{y}\| = \sqrt{y_1^2 + y_2^2 + \cdots + y_{2lm}^2}$$

3.3.3 POD coefficients

Recalling the basic properties of the POD, the original velocity field may be expanded in a series of the basis modes. The expansion coefficients are determined by projecting the velocity field onto the POD basis and are labeled the POD coefficients. In the discrete case the expansion reads:

$$\mathbf{u}^n = \sum_{i=1}^{N} a_i^n \boldsymbol{\phi}^i = \boldsymbol{\Psi} \mathbf{a}^n \tag{3.36}$$

where $\boldsymbol{\Psi} = [\boldsymbol{\phi}^1 \ \boldsymbol{\phi}^2 \ \ldots \ \boldsymbol{\phi}^N]$ has been introduced. From the orthonormality of the POD basis it directly follows that

$$\mathbf{a}^n = \boldsymbol{\Psi}^T \mathbf{u}^n \tag{3.37}$$

from which the POD coefficients are determined. It may be shown (see [40]) that the coefficients can also be derived directly from the eigenvalues and eigenvectors resulting from (3.31).

Thus, for each snapshot a coefficient vector is found whose elements correspond to the different basis modes. The POD coefficients are important for two major reasons. Depending on the solution procedure, the signs of the eigenvectors resulting from solution of the problems (3.30) or (3.31) may not be consistent. Hence, when considering a given POD mode, the sign of the associated coefficient should also be taken into account. For instance, if one wants to determine the qualitative influence of a given POD mode in a specific snapshot, the sign of the coefficient associated with this snapshot should be considered. Secondly, and more importantly, the size of the different POD coefficients in the expansion directly shows the influence of the different POD modes in a given snapshot. Although the first modes represent the most energetic structures of the flow, some of the less energetic modes may contribute more strongly or frequently to instantaneous flow realizations. Further, for flows of little complexity, very few modes may be sufficient to completely describe the physics. Therefore, an investigation of

the POD coefficients is crucial to correctly describe the dynamical behavior of the flow under investigation. A practical example of the the variation of the POD coefficients and the implications for the behavior of the flow field considered can be found in part B of this thesis.

3.3.4 Numerical accuracy

From a theoretical point-of-view, there is no difference between applying POD to a dataset obtained experimentally, from PIV measurements, and computationally by for instance LES. In practice there is a substantial difference in numerical accuracy, however, which is reflected in the behavior of the eigenvalues resulting from the POD analysis. When performing a numerical calculation the accuracy of the data is limited by machine accuracy, while the accuracy of the PIV data is typically 0.1 pixel per 10 pixels, i.e. about 1%. Introducing a measure for the relative energy of the POD mode at energy level i as

$$\varepsilon_i = \frac{\lambda^i}{\sum_{j=1}^{N} \lambda^j} \tag{3.38}$$

and assuming that a number of snapshots sufficient for statistical convergence have been sampled the value of ε_i at large i will be of the order of 10^{-16} for the LES data, while the smallest values of ε_i for a dataset obtained with PIV will typically be in the range of 10^{-3} to 10^{-2} (cf. parts B and B of the present thesis). In both cases, as the energy level decreases, the size of the structures revealed in the modes also becomes smaller. For the numerical data the modes corresponding to the smallest eigenvalues are representative of noise only and thus cannot be assimilated to coherent structure. For the PIV data random errors *reminiscent* of coherent structure may affect some of the modes at lower energy levels. This implies that to obtain a satisfactory description of a given velocity field more snapshots may be required from PIV measurements than from a numerical simulation of the same flow. If only PIV data are available the big question to address is which modes are representative of coherent structure and which modes are representative of noise. Fortunately the most dominant structures are normally far more energetic than possible systematic errors, so the primary outcome of the POD analysis is the same. Of course the ideal situation is when both data from measurements and simulation are available. In this case, POD could also be used as a tool for comparison and validation of the numerical data. Although this idea seems obvious, no attention seems to have been paid to it in the literature so far.

3.4 Interpretation of the POD modes

An interesting point to address when carrying out a POD analysis is when, and to what extent, the POD modes can be interpreted as representative of actual physical structure in the flow. An instructive example is found in the work of Kevlahan et al. [43], who compared different analytical techniques for identifying structures in turbulence. They

considered a test function given by

$$u(x) = (a + bx)\exp(-x^2) \tag{3.39}$$

with the coefficients a and b taken as normally distributed random variables with zero mean, this asymmetric function being considered to be representative of a typical eddy appearing in a turbulent flow. Performing the POD an analytical solution could be obtained to yield

$$\phi^1 = \sqrt{2}\pi^{-1/4} x \exp(-x^2), \quad \phi^2 = \pi^{-1/4}\exp(-x^2)$$

with the eigenvalues

$$\lambda^1 = \lambda^2 = \sqrt{\pi}(\sigma_a^2 + \sigma_b^2)$$

where σ_a^2 and σ_b^2 denote the variances of the coefficients a and b, respectively. Figures

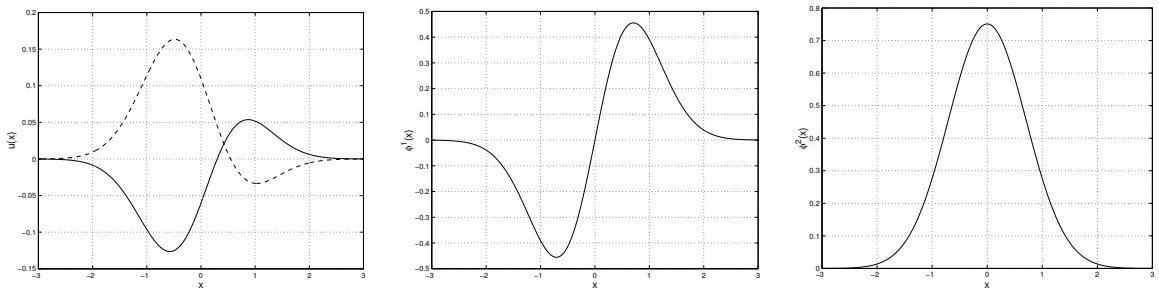

(a) (b) (c)

Figure 3.1: (a) *Realizations from equation* (3.39) – *asymmetric.* (b) *Mode 1 – anti-symmetric.* (c) *Mode 2 – symmetric.*

3.1(a) and 3.1(b)–3.1(c) show two typical realizations from equation (3.39) and POD modes 1 and 2, respectively. The two POD modes are anti–symmetric and symmetric, respectively and hence neither captures the asymmetrical shape of the eddy given by (3.39). Adding the two modes, however, a function behaving like the original signal results. The explanation is that the energy contained in the modes is the same for both. It is unlikely in practice that identical eigenvalues are found among the first POD modes. It is quite common though, that two modes are found at *approximately* the same level of energy. This situation arises in convectively dominated flows where pairs of modes represent essentially the same spatial structure, but shifted in the streamwise direction. The phenomenon is seen, for example, in Rempfer's investigation of boundary layer transition [74] and in the work of Graham et al. [35], who addressed optimal control of vortex shedding in the wake of a cylinder. The analysis by Kevlahan et al. shows that in such cases a better representative of flow structure at the energy level in question is likely to be obtained by adding together the two modes. This was also reported by Rempfer and Fasel [73], who suggested that the coherent structure, representing a level of energy at which two POD modes are found, should be given as

the sum of the two POD modes multiplied by their respective coefficients. Thus, the sum

$$a_i^n \boldsymbol{\phi}^i + a_{i+1}^n \boldsymbol{\phi}^{i+1}$$

should be interpreted as the coherent structure at time t^n associated with the energy $\lambda^{i+1} \approx \lambda^i$. For a further discussion, see also [23].

3.5 Summary

In the present chapter a comprehensive introduction to the application of the Proper Orthogonal Decomposition (POD) in the study of turbulence has been provided. First, the two main version of the POD i.e. the "classical POD" and the "snapshot POD" were introduced through a historical review, describing some of the many applications since the technique was first introduced to the fluid mechanics society in 1967. Second, the basic equations of the two approaches were derived and it was shown how, in general, the classical and the snapshot POD applies to experimental and numerical datasets, respectively. An exception is data obtained from PIV where the spatial resolution is high and the temporal resolution low compared to other experimental techniques. As a consequence, the snapshot POD will be applied for the investigations in the present thesis.

Having derived the basic equations, a detailed description was given of how to implement the POD in practice when considering a given ensemble of flow realizations. Discrete versions of the equations were stated for calculation of the POD modes and their coefficients. Also a short comment was made on numerical accuracy. Finally, an analytical example was used to illustrate how care should be taken when interpreting the POD modes in the context of coherent structures.

Chapter 4

Linear Stochastic Estimation

The following sections provide an introduction to the application of Linear Stochastic Estimation (LSE) in the study of turbulence. The concept of a conditional eddy is discussed and the basic equations of LSE are derived. Further, an analytical example is given to illustrate the strengths and weaknesses of LSE for extraction of coherent structures.

4.1 Introduction

The LSE was first introduced by Adrian (see [1]), who defined a conditional eddy (CE) as a conditional field specifying a velocity field given an event:

$$\langle \mathbf{u}' | \mathbf{E} \rangle \tag{4.1}$$

Where in general $\mathbf{u}' = \mathbf{u}(\mathbf{x}', t')$ denotes the velocity field and $\mathbf{E} = (E_1, \ldots, E_N)$ is an appropriate set of event data. In the following, since the topic of investigation is turbulence, the conditional field will represent the fluctuating part of the velocity field. The CE may or may not be truly representative of coherent structure. Hence, it should be interpreted only as an average field associated with the occurrence of the event $\mathbf{E}$. Obviously, the choice of event vector is critical to the formation of the CE. With very complex $\mathbf{E}$ a perfect reconstruction of an entire velocity field could be obtained. However, this would not be a coherent structure. Too little data on the other hand may lead to a field bearing little resemblance to a coherent realization. All in all, the CE is only an imperfect representative of coherent structure and thus should not be treated as more than that.

The LSE provides a first order estimate of the conditional average given by (4.1). In general, this estimate is conditional upon time as well as spatial position. However, in most applications, only the spatial dependence is considered. Accordingly, in the following the conditional velocity field will simply be $\mathbf{u}' = \mathbf{u}(\mathbf{x}')$. The nature of the event vector depends on the problem at hand. Adrian and Moin, for example, used both the velocity and deformation tensor as event data in their study of organized turbulent structure in homogeneous shear flow [3]. More recently, Naguib et al. used the wall pressure fluctuations in a turbulent boundary layer [59]. In many cases the velocity at one or more points is enough to obtain a good estimate of the conditional

velocity field. An interesting example is provided by [100], where Zhou et al. used LSE to generate initial conditions for a direct numerical simulation of the evolution of vortex structures in channel flow. An overview of the choices of event data up to 1991 can be found in [6]. The investigations in the present work are based on events given as velocity vectors at one or several points in the domain considered.

4.2 Basic equations

The LSE is defined by expanding the CE in a Taylor series around $\mathbf{E} = 0$ retaining only the first order term. Marking the estimated velocities by a tilde the result is written

$$\widetilde{u}_i' = A_{ij} u_j \tag{4.2}$$

where the indices i and j refer to the coordinate directions and the elements of the (velocity) event vector, respectively. The $A_{ij} = A_{ij}(\mathbf{x}, \mathbf{x}')$, which remain to be determined are labeled *estimation coefficients*. These are found by minimizing the mean square errors,

$$e_i = \langle [u_i' - A_{ij} u_j]^2 \rangle \tag{4.3}$$

for each component of $\mathbf{u}'$. The resulting expression derived in appendix B becomes:

$$\langle u_j(\mathbf{x}) u_k(\mathbf{x}) \rangle A_{ij}(\mathbf{x}, \mathbf{x}') = \langle u_i(\mathbf{x}') u_k(\mathbf{x}) \rangle \tag{4.4}$$

where k is a dummy index running from one to the number of event elements. From equation (4.4) it follows that the A_{ij} are determined from two–point correlations and Reynolds stresses. This result is one of the most interesting features of LSE: the estimation coefficients used in the approximation of the conditional average are calculated from unconditional moments. Thus, the LSE makes it possible to extract conditionally averaged behavior without performing conditional sampling.

How to implement LSE in practice is most easily illustrated by a specific example. Considering a two-point event in a 2D domain yields a system corresponding to $i = 1, 2$ and $j, k = 1, 2, 3, 4$, as follows:

$$\begin{bmatrix} \langle u_1 u_1 \rangle & \langle u_1 u_2 \rangle & \langle u_1 u_3 \rangle & \langle u_1 u_4 \rangle \\ \langle u_1 u_2 \rangle & \langle u_2 u_2 \rangle & \langle u_2 u_3 \rangle & \langle u_2 u_4 \rangle \\ \langle u_1 u_3 \rangle & \langle u_2 u_3 \rangle & \langle u_3 u_3 \rangle & \langle u_3 u_4 \rangle \\ \langle u_1 u_4 \rangle & \langle u_2 u_4 \rangle & \langle u_3 u_4 \rangle & \langle u_4 u_4 \rangle \end{bmatrix} \begin{bmatrix} A_{11} & A_{21} \\ A_{12} & A_{22} \\ A_{13} & A_{23} \\ A_{14} & A_{24} \end{bmatrix} = \begin{bmatrix} \langle u_1' u_1 \rangle & \langle u_2' u_1 \rangle \\ \langle u_1' u_2 \rangle & \langle u_2' u_2 \rangle \\ \langle u_1' u_3 \rangle & \langle u_2' u_3 \rangle \\ \langle u_1' u_4 \rangle & \langle u_2' u_4 \rangle \end{bmatrix} \tag{4.5}$$

Note that in this case u_1 and u_2 represent the u– and v–velocity, respectively, at the first event point and analogously for u_3 and u_4 at the second event point. Thus, in order to obtain the system corresponding to only the first event point all elements involving subscripts ≥ 3 should simply be removed.

In general, the number of unknowns in the system to be solved is given by the number of velocity components times the number of event elements. The system is then solved for each point in the domain. Once having determined the A_{ij} for given event points many different events may be investigated in a short amount of time, whereas conventionally obtained conditional averages would require tedious calculations including all the available data for each choice of event.

4.3 Analytical example[1]

In the following it will be shown how LSE applies to the case of homogeneous isotropic turbulence. While nicely illustrating the strength of LSE for reproduction of coherent structure, the example also shows some of its limitations.

For homogeneous isotropic turbulence an exact expression for the two–point velocity correlation tensor, R_{ij} can be derived. The original derivation can be found in [11] (see also e.g. [7] or [52]). Normalized by the mean–squared turbulence velocity, $\langle u_i u_i \rangle / 3$ (or in terms of turbulent kinetic energy $\frac{2}{3}K$), the expression reads:

$$R_{ij}(\mathbf{r}) = \frac{f(r) - g(r)}{r^2} r_i r_j + g(r)\delta_{ij} \tag{4.6}$$

where f and g are the longitudinal (uu) and transverse (vv or ww) correlation coefficients, respectively, and δ_{ij} is the Kronecker delta. Restricting the analysis to 2D, the distance from the origin becomes:

$$r = \sqrt{x^2 + y^2}$$

and the two components of $\mathbf{r}$:

$$r_i = r\cos(\phi), \quad r_j = r\sin(\phi)$$

where

$$\phi = \begin{cases} \frac{\pi}{2} & \text{for } x = 0 \\ \arctan\left(\frac{y}{x}\right) & \text{otherwise} \end{cases}$$

Further, the spatial correlation functions, f and g, are related as follows [7]:

$$g(r) = f(r) + \frac{1}{2} r \frac{df}{dr} \tag{4.7}$$

For homogeneous isotropic turbulence, f is well approximated by an exponential function. Thus:

$$f(r) = \exp\left(-\frac{1}{2}r^2\right) \tag{4.8}$$

and hence from (4.7):

$$g(r) = \left(1 - \frac{1}{2}r^2\right) \exp\left(-\frac{1}{2}r^2\right) \tag{4.9}$$

Now, inserting equations (4.8) and (4.9) into (4.6) and using the above expressions for r, r_i and r_j, an analytical expression for R_{ij} as function of the spatial position, (x, y), can be obtained. For each value of (x, y) the four elements of a 2×2 matrix gives the spatial correlation between the velocities at the point in question and the velocities at the origin.

[1] Based on private communication with prof. dr. ir. J. Westerweel.

Referring to section 4.2 the LSE coefficients are obtained from:

$$\langle u_j u_k \rangle A_{ij} = \langle u_i' u_k \rangle \tag{4.10}$$

Specifying a velocity event vector at the origin the prime refers to position (x, y). As isotropy has been assumed, the Reynolds stress matrix is equal to $\langle u_i u_i \rangle / 3$ times the identity matrix at all points and it follows that the LSE coefficients are identical to the elements of the two-point correlation matrices except for a constant. Thus, specifying an event vector at the origin the LSE may now be found.

Figure 4.1 shows two estimates based on event vectors (marked by red circles) specified at the origin. Both LSEs yield a ring vortex, which is one of the most basic

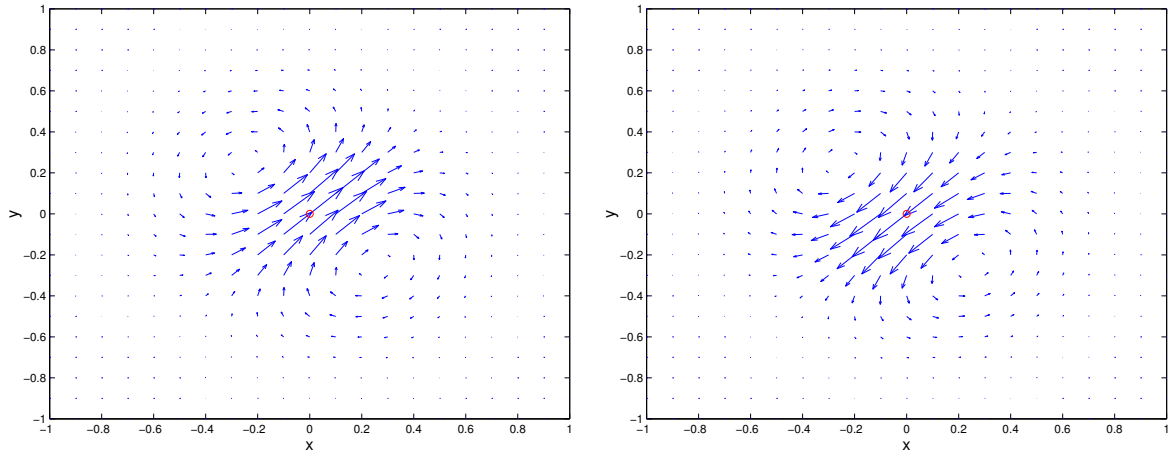

Figure 4.1: *Single-point LSEs in homogeneous isotropic turbulence.*

structures of homogeneous isotropic turbulence, and hence the result makes perfect sense physically. The velocities are seen to go to zero at large separations. This is in agreement with the fact that the LSE provides an estimate of the *conditional* average of the velocity field. Far away from the specified event the velocity field is independent of the event and thus illustrated by the definition of the CE

$$\langle \mathbf{u}' | \mathbf{E} \rangle \rightarrow \langle \mathbf{u}' \rangle = 0 \tag{4.11}$$

where the last equality results from the fact that the data considered is the fluctuating part of the velocity field.

The event vectors used are $(u_0, v_0) = (1, 1)$ and $(u_0, v_0) = (-1, -1)$, respectively. Since isotropy has been assumed it is not surprising that the two results are identical except for a sign reversal. This is by no means unique for the present flow, however. Writing out the basic LSE equation, equation (4.2), it becomes clear that changing the sign of the event vector simply also causes the LSE to come out with the opposite sign. Thus, for any flow, the structure identified by a single-point LSE is independent of the sign of the event vector. As a result, single-point LSEs in e.g. turbulent pipe flow can not discriminate between the two fundamentally different flow structures 'ejections' and 'sweeps', as was pointed out by Meyer and Westerweel [56]. This is one of the most obvious limitations of the LSE. Another related limitation has to do with the

fact that the length of the event vector has no influence on the qualitative outcome. Multiplying the event vector with a factor of e.g. 2 just causes the vectors in the LSE to become twice as long. In real flows it must be expected that velocity vectors of different magnitudes are associated with different flow structures. The two limitations are related in the sense that scaling the event vector by any factor, including -1, has no effect on the result from a qualitative point of view. This shortcoming was already pointed out by Adrian [1]. He also showed, however, that including quadratic terms in the estimate of the conditional eddy, thus obtaining a 'QSE' which would eliminate the problem, normally has a minor effect on the final result. An observation which has been well confirmed since [6].

It is noted that these limitations can be partly overcome by introducing several event points. With more than one event point the directions and length ratio of the different vectors both influence the final result. This again underlines the fact that the correct choice of event vector is crucial to the outcome of the LSE.

4.4 Summary

The concept of a conditional eddy has been introduced, and it has been discussed to what extent this quantity may be representative of coherent structure. Introducing an approximate expression for the CE leads to the LSE, which provides a first order estimate of a conditional average given an event. The basic equations for the LSE have been derived and it has been shown how to implement the method in practice. Finally an analytical example has been provided, which illustrates the strengths and weaknesses of the LSE in reproducing coherent structure of turbulent flows.

Part B

Ventilated room

Chapter 5

POD Analysis of Flow Structures in the Annex 20 Room

The contents of the present chapter were published in *Experiments in Fluids* under the title "POD analysis of flow structures in a scale model of a ventilated room" [66]. Although the section containing the review of the POD slightly overlaps with the theory from the previous chapters, it has been chosen to reproduce the article in full. The only changes made are with respect to layout and references.

Abstract Measurements with particle image velocimetry (PIV) have been carried out in a scale model of the Annex 20 room. Data were taken in a plane near the inlet. The flow consisted of a wall jet ($Re \approx 5000$) and a low–velocity region below the jet. Proper Orthogonal Decomposition (POD) was used to analyze dominant flow structures. The analysis showed that the flow some of the time has flow structures very different from the mean velocity field. A time–resolved data series was projected onto the orthonormal basis derived from the POD for analysis of the time variation of the POD amplitudes.

5.1 Introduction

The Annex 20 room [61] is a standard measure room which is used for investigation of ventilation problems and indoor environment. It has been constructed such that its shape and the inlet/outlet conditions are representative of a typical room in an office building. Of special interest are human comfort parameters such as draught (maximum local velocities) and transport of pollutants. From a fluid mechanics point-of-view the flow poses a great challenge. A turbulent wall jet is formed by the inlet. For a review of the turbulent wall jet, see [33]. The jet region is highly turbulent, while other regions of the room are characterized by very low velocities. Thus, the flow involves laminar-turbulent transition, which makes numerical investigation by turbulence modeling for the Reynolds–averaged Navier–Stokes equations (RANS) difficult, see e.g. [17]. The flow evolves quite slowly in time and low sampling rates are required for the measured data to be statistically uncorrelated. Hence, measurement of mean quantities

becomes very time consuming with point-wise measurement techniques like hot-wire and laser doppler anemometry (LDA). These features suggest that great advantage may be derived from the use of PIV for investigation of the flow in the Annex 20 room. Mean quantities are determined at many locations simultaneously, greatly reducing the amount of time necessary compared to e.g. LDA. Having sampled appropriate data, another obvious application would be comparison with numerical data to verify results from different turbulence models or Large Eddy Simulation (LES).

A way to extract the dominant structures of a flow is by application of the Proper Orthogonal Decomposition (POD) technique [49, 57]. This technique is interesting for several reasons. It may be used to compare the instantaneous flow structures found from PIV data to results from LES. It is a powerful tool in the context of data reduction and hence may also be used to create databases with e.g. inlet conditions for use in numerical simulations. In the studies presented here, the PIV data obtained are analyzed with regard to a study of the flow structures appearing in the flow of the Annex 20 room. Thus the POD is used to find the dominant structures of the flow in the measuring domain considered. Due to the large time scales, a satisfactory time resolution of the flow may be obtained from PIV data taken at high sampling rate (10 Hz). This is utilized in the last part of the paper, where the temporal evolution of the flow is studied by projecting the temporally resolved velocity data onto the POD basis obtained from the statistical analysis.

5.2 Experimental setup

A Perspex 1:15 scale model of the Annex 20 room has been constructed, using water as fluid, to facilitate measurements with PIV. Figure 5.1 shows a 2D sketch of the model.

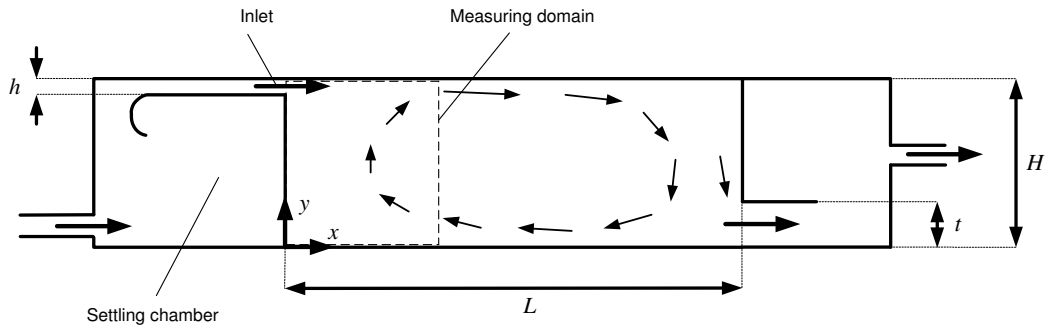

Figure 5.1: *A 2D sketch of the model with inlet and outlet chambers and definition of coordinate system.*

Flow chambers were placed before and after the actual Annex 20 part to ensure appropriate inlet and outlet conditions. Fluid is supplied at the upper left of the room and leaves at the lower right. The dimensions of the model room are: length: $L = 600$ mm, height: $H = 200$ mm, width: $W = 200$ mm, inlet height: $h = 11.2$ mm, and outlet height: $t = 32$ mm. The Reynolds number, $Re \approx 5000$, is based on the mean inlet velocity, $u_0 \approx 0.45\frac{\mathrm{m}}{\mathrm{s}}$, and the inlet height. Earlier studies, both experimental and

numerical, have used Reynolds numbers of a similar magnitude [60, 17]. For this Re value, the mean flow is characterized by a large recirculation zone (indicated by arrows in figure 5.1) in the center of the room and two small recirculation zones appearing in the corners to the lower left and the upper right. The measurements were taken in a square section in the region $0 < x < 200$ mm and $0 < y < 200$ mm at $z = 0$, as indicated in figure 5.1 by the dashed square right after the inlet. Figure 5.2 shows the whole setup with placement of model, camera, and the light-sheet optics forming the laser-sheet in the measuring domain. The pipes indicated at both ends of the model were connected to a circulation unit placed below the model. The circulation unit consisted of a pump and an orifice flow meter connected to a manometer for controlling the flow rate. The flow rate was adjusted by changing the number of revolutions per minute of the pump. The measuring equipment was a Kodak MegaPlus ES 1.0 camera

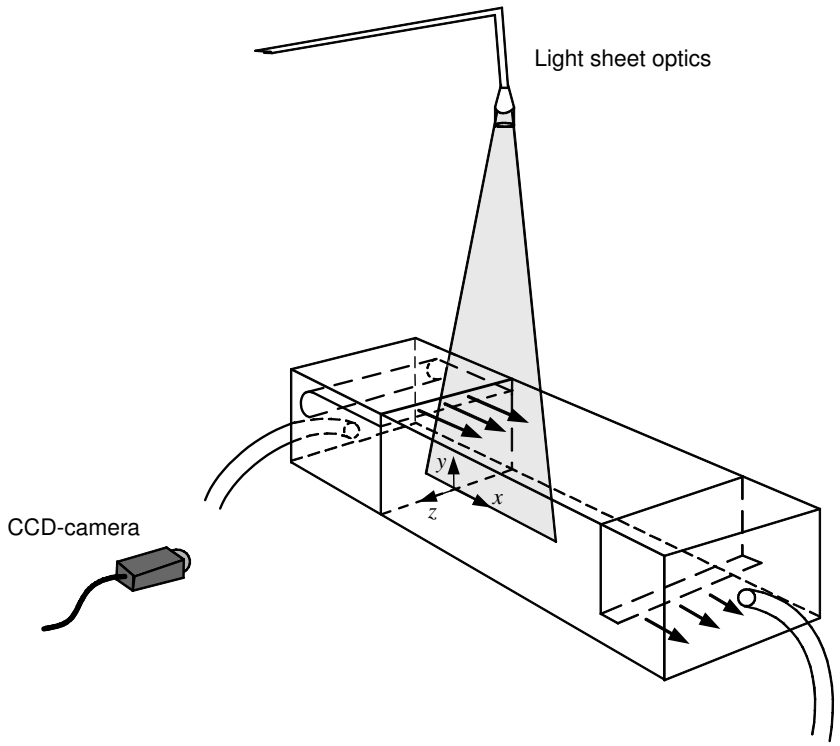

Figure 5.2: *Experimental setup with scale model, camera, and light-sheet optics.*

and a double cavity Nd-YAG laser delivering 100 mJ per light pulse. The data collection was controlled by a Dantec PIV2100 processor. Polyamid particles with a mean diameter of 20 μm was used as seeding. The Kodak Megaplus ES 1.0 has a resolution of 1008×1016 pixels with a pixel size of 9 μm giving a total chip size of approximately 9.1×9.2 mm^2. During the measurements the camera was placed such that the image covered exactly the object plane. Thus with a measuring domain of 200×200 mm^2, a magnification factor of $M = \frac{9.2}{200} = 0.046$, based on image height, was used in the measurements. Using the following formula for calculation of the diffraction limited minimum image diameter [71]:

$$d_{\mathrm{d}} = 2.44 f^{\#}(M + 1)\lambda \tag{5.1}$$

where $f^{\#}$ (the f-number) is the numerical aperture of the camera and $\lambda = 532$ nm the wavelength of the laser light, it was found that using an f-number of $f^{\#} = 11$ was appropriate to ensure that a particle image covered 1-2 pixels on the CCD chip, thus minimizing the measurement errors caused by pixel locking, see [89]. Having chosen an appropriate f-number, three parameters were optimized in order to obtain high quality recordings:

- Image density, N_I
- Time between pulses, Δt
- Time between recordings, t_0

Following [41], the image density, N_I, should be at least 15 to get a good PIV recording. Further the in-plane and out-of-plane displacements should not exceed 25% of the interrogation area (IA) side length or the laser-sheet thickness, respectively. An IA size of 32×32 pixels was used for the analysis of the PIV images. Thus to make sure that the requirement $N_I \geq 15$ was met, seeding was added to the flow until a zoom of the image maps containing an area of approximately 32×32 pixels showed a density of about 20 particle pairs. The time between pulses was set to $\Delta t = 3500$ μs. This yielded an in-plane displacement slightly higher than 25% of the IA side length in the jet region. However, good velocity data in this region was still obtained by use of *adaptive correlation*. The laser-sheet thickness was approximately 1 mm corresponding to about 20% of the IA side length. Thus, assuming the out-of-plane displacement to be less than 20% of the in-plane displacements, the requirement of less than 25% out-of-plane displacement was also met. Measurements with LDA were performed in representative points of the domain prior to the PIV measurements. Integrating the autocorrelation function it was found that the integral time scales in the jet region are on the order of 10 ms. In the bottom region of the domain, however, time scales as high as 1.5 seconds were found. Thus, to make sure that the measurements for use in the statistical analysis were independent, the time between recordings was set to $t_0 = 3$ s. A total of 500 images were sampled. The data used for the study of the temporal evolution of the flow were taken at the maximum frequency of the system, namely 10 Hz. The total number of images recorded was 100.

5.3 Data reduction

In the following, a brief explanation of the processing of the PIV data and a short review on the theory behind the POD is given.

5.3.1 Image processing

The images were processed with Dantec FlowManager ver. 3.40 using adaptive correlation. Adaptive correlation is especially well suited for flow fields where big differences in mean flow velocities are present. This is the case for the flow in the Annex 20 room, where the velocities in the wall jet region are significantly larger than in the regions away from the jet. The images were processed using one refinement step going from

initially 64 × 64 pixels to the final resolution of 32 × 32 pixels per interrogation area. After each step, the vector maps were filtered to remove spurious vectors by substituting each vector with the uniformly weighted average of the vectors in a neighborhood of 3 × 3 vectors. A 25% overlap was used in the processing, yielding vector maps of 41 × 42 vectors each in total.

5.3.2 Proper orthogonal decomposition

The Proper Orthogonal Decomposition also known as the Karhunen-Loeve expansion was first introduced in fluid mechanics by Lumley [49] and is based on energy considerations. Several versions of the POD have been developed and used since then. In the present analysis, the so-called snapshot method suggested by Sirovich [79] is applied. The discrete PIV data from each vector map (snapshot) are arranged in vectors, $\mathbf{x}_i$. By subtracting the ensemble average from each realization, vectors, $\mathbf{v}_i$, containing the fluctuating part of all velocities in the domain for the i'th snapshot, are obtained. Thus with n snapshots:

$$\mathbf{v}_i = \mathbf{x}_i - \frac{1}{n}\sum_{j=1}^{n}\mathbf{x}_j \quad , \quad i = 1 \dots n \tag{5.2}$$

From these vectors an $n \times n$ auto-covariance matrix, $\mathbf{R}$, is formed with elements:

$$R_{ik} = \mathbf{v}_i \cdot \mathbf{v}_k \tag{5.3}$$

Solving the algebraic eigenvalue problem for this matrix an orthonormal basis can be constructed as:

$$\boldsymbol{\phi}^k = \frac{\sum_{i=1}^{n} g_i^k \mathbf{v}_i}{\left\| \sum_{i=1}^{n} g_i^k \mathbf{v}_i \right\|} \tag{5.4}$$

where g_i^k is the i'th component of the normalized eigenvector corresponding to the k'th eigenvalue, λ_k. An eigenvalue represents the total energy contained in the corresponding mode given by (5.4). Hence, ordering the eigenvalues as $\lambda_1 > \lambda_2 > \cdots > \lambda_{n-1} > 0$, the first modes found are the most energetic ones. In this way, interpreting a given mode as a coherent structure, the first modes represent the largest, most dominant structures of the flow.

Having constructed the orthonormal basis, the original flow field may be reconstructed by:

$$\mathbf{V} = \boldsymbol{\Phi}\mathbf{A} \tag{5.5}$$

where $\boldsymbol{\Phi}$, $\mathbf{V}$ and $\mathbf{A}$ are matrices containing the $\boldsymbol{\phi}^k$, the $\mathbf{v}_k$ and $\mathbf{a}^k$ vectors columnwise, respectively, the latter being the coefficient vector associated with $\mathbf{v}_k$. With velocity data sampled at a given frequency this can be utilized to determine the coefficients, or

amplitudes, $\mathbf{a}$, of the POD modes as a function of time. Since the POD modes form an orthonormal basis, equation (5.5) leads to:

$$\mathbf{A} = \mathbf{\Phi}^{\mathrm{T}}\mathbf{V} \tag{5.6}$$

Knowing the coefficients, $\mathbf{a}^k$, a given snapshot may then be reconstructed as follows:

$$\mathbf{x}_k \approx \sum_{i=1}^{m} \boldsymbol{\phi}^i a_i^k + \frac{1}{n}\sum_{j=1}^{n} \mathbf{x}_j \tag{5.7}$$

The value of m specifies the number of basis modes included in the reconstruction. The number of modes needed to get a satisfactory representation depends on the complexity of the flow. What is of interest in the present case, however, is the behavior of the amplitudes, $\mathbf{a}$. Investigation of the temporal evolution of $\mathbf{a}$ yields a picture of how the influence of the different POD modes varies in time.

5.4 Results and discussion

5.4.1 Vector maps and flow statistics

Figure 5.3 shows the ensemble average of the 500 independent instantaneous vector maps and the contours of the turbulent kinetic energy estimated as $(\langle u'u'\rangle + \langle v'v'\rangle)$ normed with u_0^2. The mean field velocities have been scaled by a factor of 0.1 to yield

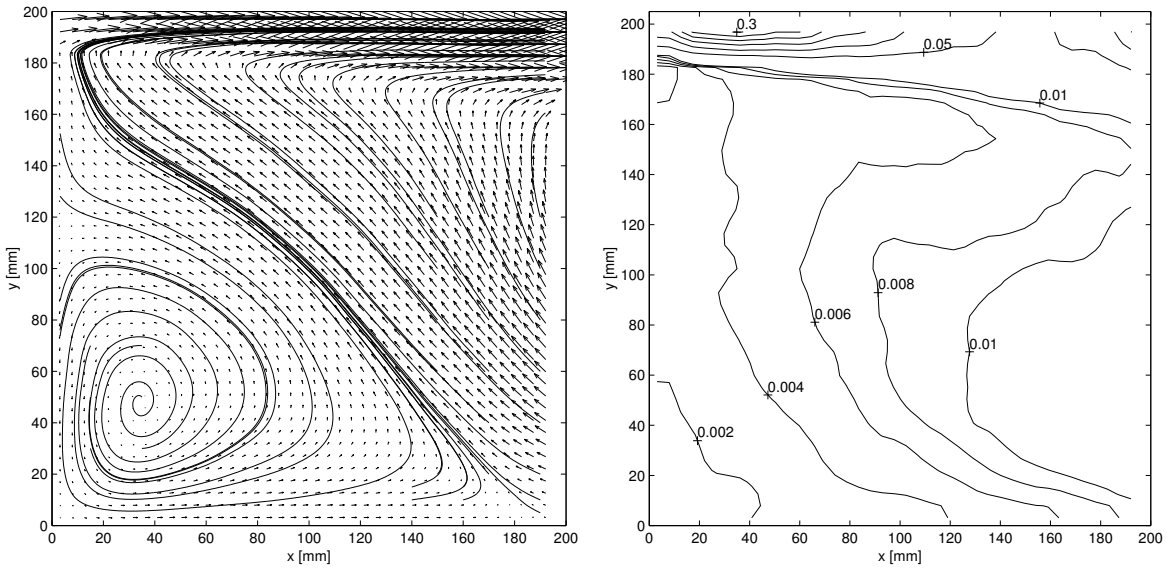

Figure 5.3: *Left: ensemble average with sectional streamlines of the 500 instantaneous vector maps. Right: distribution of turbulent kinetic energy given by* $(\langle u'u'\rangle + \langle v'v'\rangle)/u_0^2$.

suitable vector lengths. Using this scaling, the mean inlet velocity, u_0, corresponds to 45 mm or just below one fourth of the domain width. The flow is divided into a

high–velocity wall jet in a thin region at the upper boundary and a large low–velocity region below the wall jet. The velocities in the low–velocity region are on the order of 5% of u_0.

Sectional streamlines have been added to the mean flow vector map. The streamlines clearly reveal the characteristic recirculation zone which appears at the lower left corner of the Annex 20 room. The size of the recirculation zone is well defined by the singular points on the left and bottom walls at $y \approx 110$ mm and $x \approx 180$ mm. It is noted that this is a significantly larger recirculation zone than indicated by recent results from numerical simulations with RANS employing the k-ϵ model [85]. Qualitatively, however, the present results and the simulations in [85] are in good agreement.

The contours of the estimate of turbulent kinetic energy show that the highest turbulence levels are found in the regions with the highest mean velocities. The levels of the turbulent kinetic energy in the low–velocity region are on the order of 2% of the levels found in the wall jet. Thus, the velocity fluctuations are a factor of seven smaller in this region than in the jet region. In the low–velocity region, the velocity fluctuations are therefore larger than the local mean velocities. This indicates that other flow structures than the ones found in the mean velocity field are important for the flow in this region.

Figure 5.4 shows two examples of instantaneous vector maps (snapshots). Also here the velocities have been scaled by a factor of 0.1. The first snapshot has a flow field

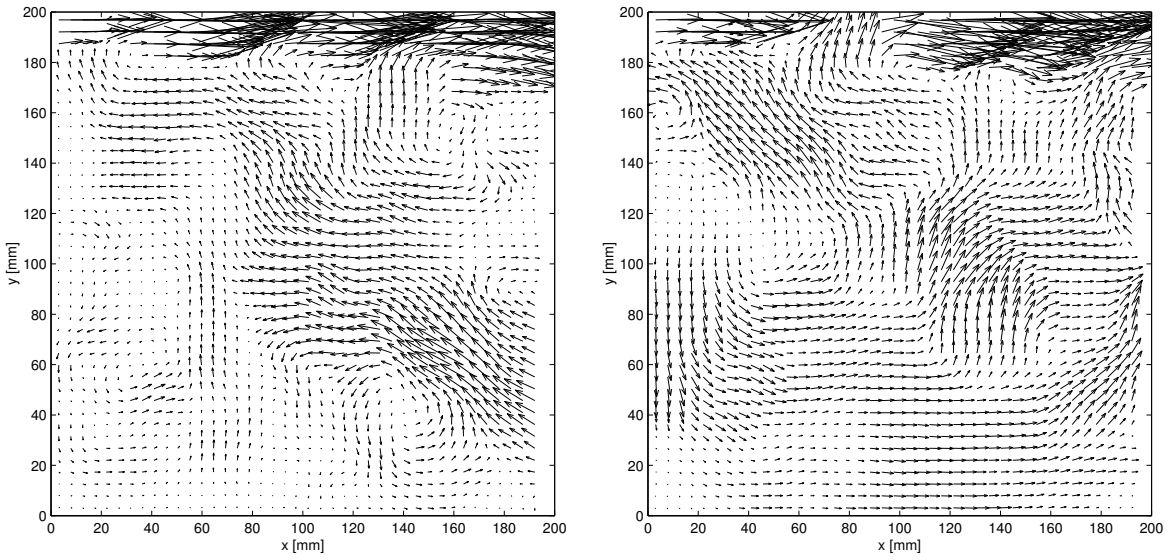

Figure 5.4: *Examples of instantaneous vector maps.*

similar to the mean velocity field shown in figure 5.3 with a general movement from the lower right directed towards the inlet. This is the case for many of the snapshots. However, a significant part of the snapshots show flow structure very different from the mean velocity field. An example is the second snapshot shown in figure 5.4. Here several small regions with different flow directions are present. In both examples the wall jet region seems to consist of "bursts" of small regions with high velocities. These bursts are seen in the majority of the snapshots and typically cover x–intervals of about

0.2–0.4H.

It might be suspected that the bursts observed in the jet region are a result of the experimental conditions (pump etc.) rather than an actual feature of the flow in the domain considered. To check the inlet conditions, LDA measurements were performed in the center of the jet region 50 mm up- and downstream of the inlet. The frequency spectra did not reveal any peaks indicating a periodic variation in the inlet conditions. This supported the assumption that the bursts observed in the PIV data are indeed a characteristic feature of the flow in the Annex 20 room, and not just an artifact of the experimental setup.

5.4.2 Dominant structures

The Proper Orthogonal Decomposition technique has been applied to extract the dominant structures of the flow in the measuring domain. Figure 5.5 shows the relative energy of POD modes 1-20 compared to the total energy of the data set. The first 20

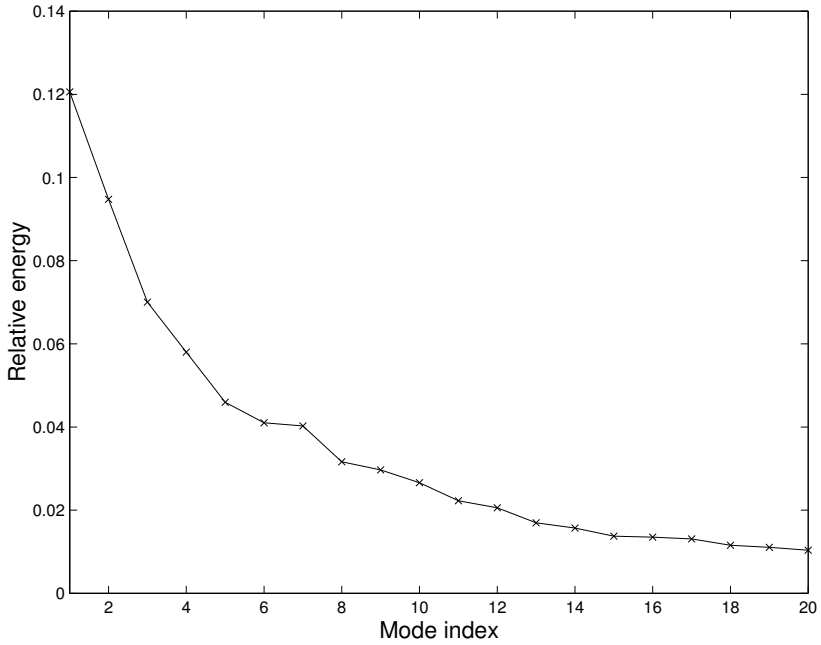

Figure 5.5: *Relative energy of first 20 POD modes.*

modes capture approximately 71% of the total energy. The curve decays rapidly in the beginning, but becomes less and less steep the higher the mode number. The lower energy levels indicate smaller flow structures, or equivalently, more detailed information about the flow. The first, most energetic modes represent the dominant, large structures of the flow. For instance, it can be seen from figure 5.5 that mode number 1 alone contains more than 12% of the total energy.

A selection of POD modes is shown in figure 5.6 (the vectors have been scaled by a factor of 0.2). The first ten modes can roughly be divided in modes related to the wall jet and modes related to the large scale flow structures in the low–velocity region. Modes 1, 3, 4 and 8 have large vectors in the wall jet region compared to the low–

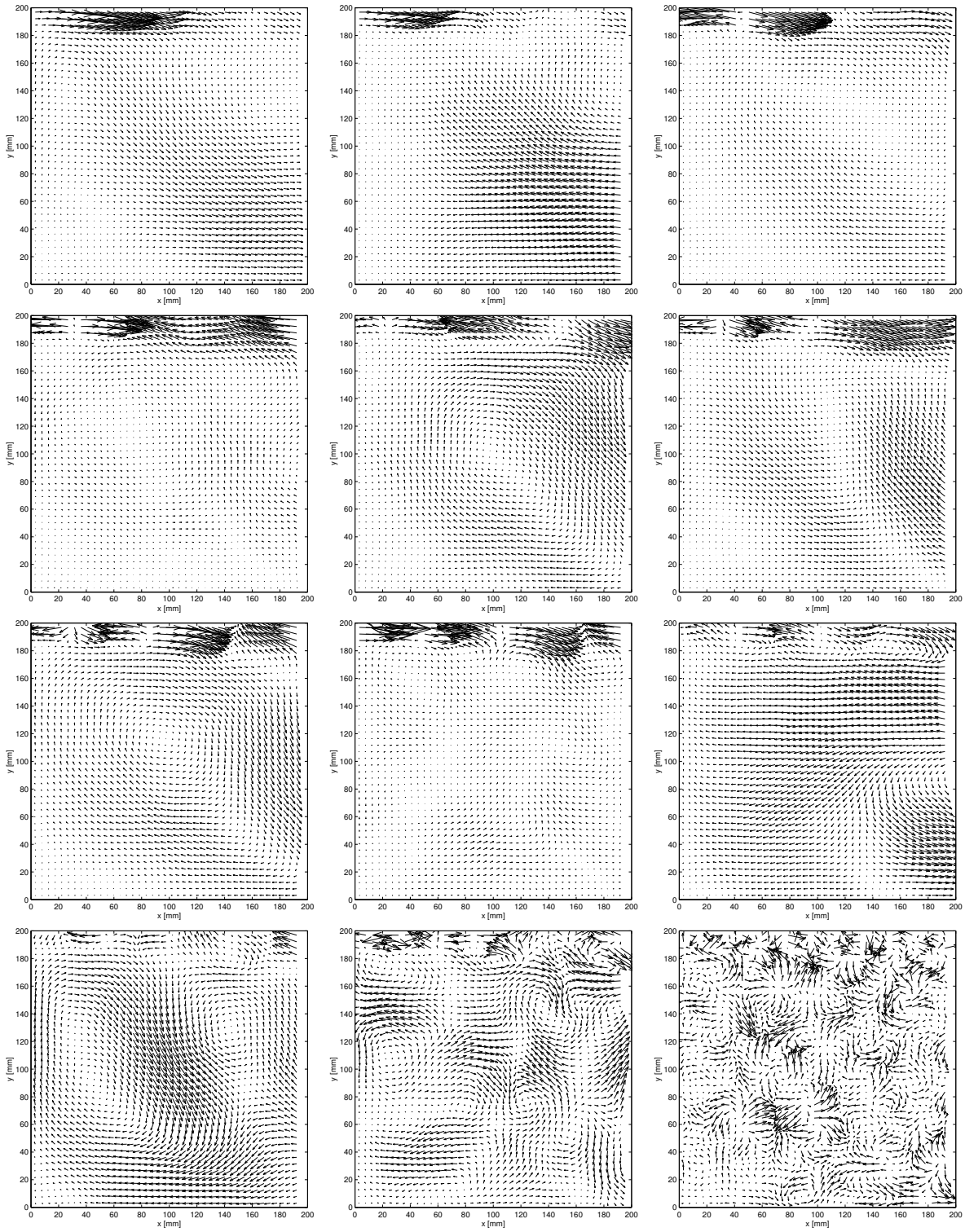

Figure 5.6: *From left to right: POD modes 1–10, 50 and 200.*

velocity region, while modes 2, 5, 6, 7, 9 and 10 have similar vector lengths all over the domain. This suggests that the dynamics of the wall jet region and the low–velocity region are different. Modes 1 and 2 both have similar flow structures with a single "burst" of large vectors in the positive x–direction appearing in the wall jet region. The burst in mode 1 is situated at $x/H \approx 0.2$ and the low–velocity region vectors are in the opposite direction of the mean flow velocities. In mode 2, the burst is very close to the inlet and there is a strong flow into the domain at the lower part of the right boundary. Both modes therefore show a correlation between a velocity burst at the inlet and an inflow/outflow in the lower right part of the domain.

Modes 3 and 4 have vectors in negative x–direction at the inlet and a region of long vectors in the downstream part of the wall jet region. Mode 3 has a burst at $x/H \approx 0.3$ and mode 4 has a negative burst at $x/h \approx 0.8$. Thus modes 3 and 4 relate to the dynamics of bursts in the downstream part of the wall jet. Modes 5 and 7 both consist of a single large vortex in the low–velocity region. This flow structure is completely different from the mean velocity field. Modes 5 and 7 also have significant vectors in the downstream part of the wall jet region, but in opposite directions. Mode 6 contains a part of a vortex with opposite sign of the one in modes 5 and 7, but also has a burst at the downstream part of the wall jet region. All in all, these three modes suggest that there is some correlation between the large vortex structure and the dynamics of the downstream part of the wall jet region. Mode 9 has a large inflow at the upper part of the right boundary and a smaller outflow at the lower part of the same boundary. A complex flow pattern is found in POD mode number 10. Compared to the other modes related to the low–velocity region, this mode offers a greater level of detail. It consists of three vortices and a separation point. Two of the vortices are situated on the left side of the domain and the third one, which appears in connection with the separation point, on the right. Like modes 2, 5, 6, and 7, modes 9 and 10 are connected to the dynamics of the low–velocity region, but are now representing flow structure at a lower energy level.

To elaborate on the behavior of the POD modes with decreasing energy level, the last two pictures show POD modes 50 and 200. Considering the first ten POD modes in figure 5.6, it seems that the level of detail increases with the mode number. Modes 1 and 2, which together capture 21.6% of the total energy, consist of large regions with uniform velocities, while mode 10, which represents 2.7% of the total energy, contains information about the presence of vortices and separation points in the low–velocity region. Mode number 50 represents only 0.3% of the total energy, but shows a very high level of detail with several small vortices scattered over the domain. This is in agreement with the theoretical description of the POD as well as the general observation that the lower the energy level, the more flow detail is offered in a given POD mode. However, depending on how many snapshots are included in the analysis there may be an upper limit of mode number to which it makes sense to talk about flow structures in the modes. The last POD mode shown, number 200, is an example of this. This mode contains information about small–scale motion only and as such cannot be interpreted as representative of flow structure.

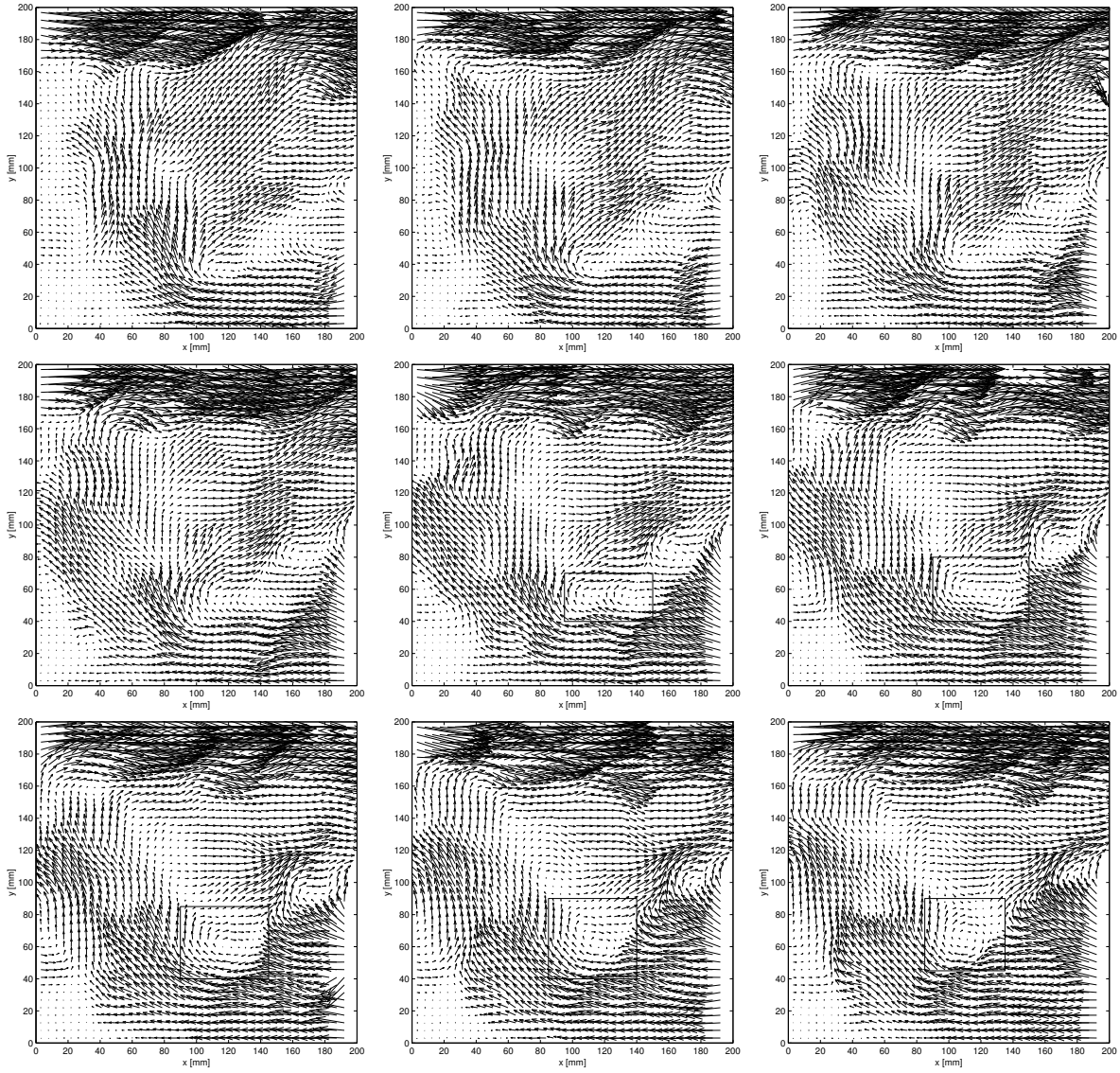

Figure 5.7: *From left to right: sequence of snapshots taken at 10 Hz. The merging of two small vortices into one is marked with a rectangle.*

5.4.3 Temporal evolution

The study of the temporal evolution of the flow is based on 100 images taken at 10 Hz. Several snapshots of each flow structure are obtained with this time resolution. A sequence from the series consisting of 9 successive snapshots (0.8 s) is shown in figure 5.7. The vectors have been scaled by a factor of 0.1 as in figures 5.3 and 5.4. Evidently, the velocities for this particular sequence are larger than on average and the wall jet region is somewhat wider than normal. As explained below, the general structure of the flow field involves a large inflow at the bottom part of the domain, which is probably the cause of the enhanced jet flow, simply due to continuity.

The overall structure of the sequence is uniform jet motion in the positive x–direction balanced by a large region with vectors pointing in the negative x–direction in the bottom of the domain and a small region to the lower left with zero velocities.

In the rest of the domain the flow changes throughout the sequence. One example is the merging of two small vortices into one, which occurs in the neighborhood of $(x, y) \approx (120, 50)$ mm. The process is marked with rectangles in figure 5.7. This example shows how small–scale changes may be followed directly from the PIV data in the low–velocity region.

The 100 snapshots taken at 10 Hz were not included in the POD analysis. However, by projecting the fluctuating part of the velocity fields onto the POD basis, the amplitudes, a_i, representing the relative influences of the different modes in a given snapshot, may still be obtained. Figure 5.8 shows the POD amplitudes of the first ten modes as functions of time for the 100 snapshots taken at 10 Hz. The amplitudes of mode 1, 3, 4 and 8 are relatively small and have rapid fluctuations. As discussed earlier, these modes are related to the dynamics of the wall jet. The amplitudes of mode 2, 5, 6, 7, 9 and 10, which were found to be related to the dynamics of the low–velocity region, are generally larger and have slower variations. Evidently, there are two different time scales for the two regions. In fact, the time scale of the dominant structures in the low–velocity region seems to be longer than the 1.5 s found from the autocorrelation of an LDA signal in a single point (cf. section 5.2).

The two vertical lines imposed on the plots indicate the start and ending point of the sequence shown in figure 5.7. As mentioned above, the large scale motion of the flow sequence shown in figure 5.7 is characterized by a movement in positive x–direction in the upper part of the domain, negative x–direction in the lower part, and a small region to the lower left with vanishing velocities. This overall flow pattern is reflected in the amplitudes of the POD modes. The coefficients of modes 5, 7 and 10 are all large and positive throughout the interval considered. Combining this with the flow structures represented in the first ten modes of figure 5.6 reveals that the contributions from these three modes act to cause this overall flow pattern. Further, the amplitude of mode 9 is large and negative, which is connected to the region of vectors just below the jet region to the right, all pointing in the positive x–direction.

Another interesting interaction between a number of the first modes is discovered by looking at the coefficients a_1, a_2, and a_6. In the beginning of the sequence, the amplitude of mode 1 is large and positive, the amplitude of mode 2 close to zero, and the amplitude of mode 6 is large and negative. During the 0.8 seconds of the time sequence, a_1 and a_6 decrease towards zero, while the coefficient of mode 2 grows from zero to a large positive value. The corresponding change in flow pattern is evident in figure 5.7. In the first vector maps, the region slightly below the middle to the right is characterized by very low velocities. With positive and negative coefficients, respectively, modes 1 and 6 both act in the opposite direction of the mean flow in this area. With a_1 and a_6 decreasing towards zero and a_2 growing to a large positive value, the situation is changed. A large uniform region with velocities directed towards the center of the domain emerges to the lower right, clearly showing the dominance of POD mode number 2 in the last snapshots of the sequence.

The present example is a specific case of the behavior of a few of the POD coefficients related to a change in the corresponding flow pattern. It was found that the overall flow pattern for the time sequence considered was dominated by POD modes 5, 7, and 10 apart from the mean flow field. In general, the large scale motions of a particular flow is determined by the mean field and a number of the first few POD modes. For simple

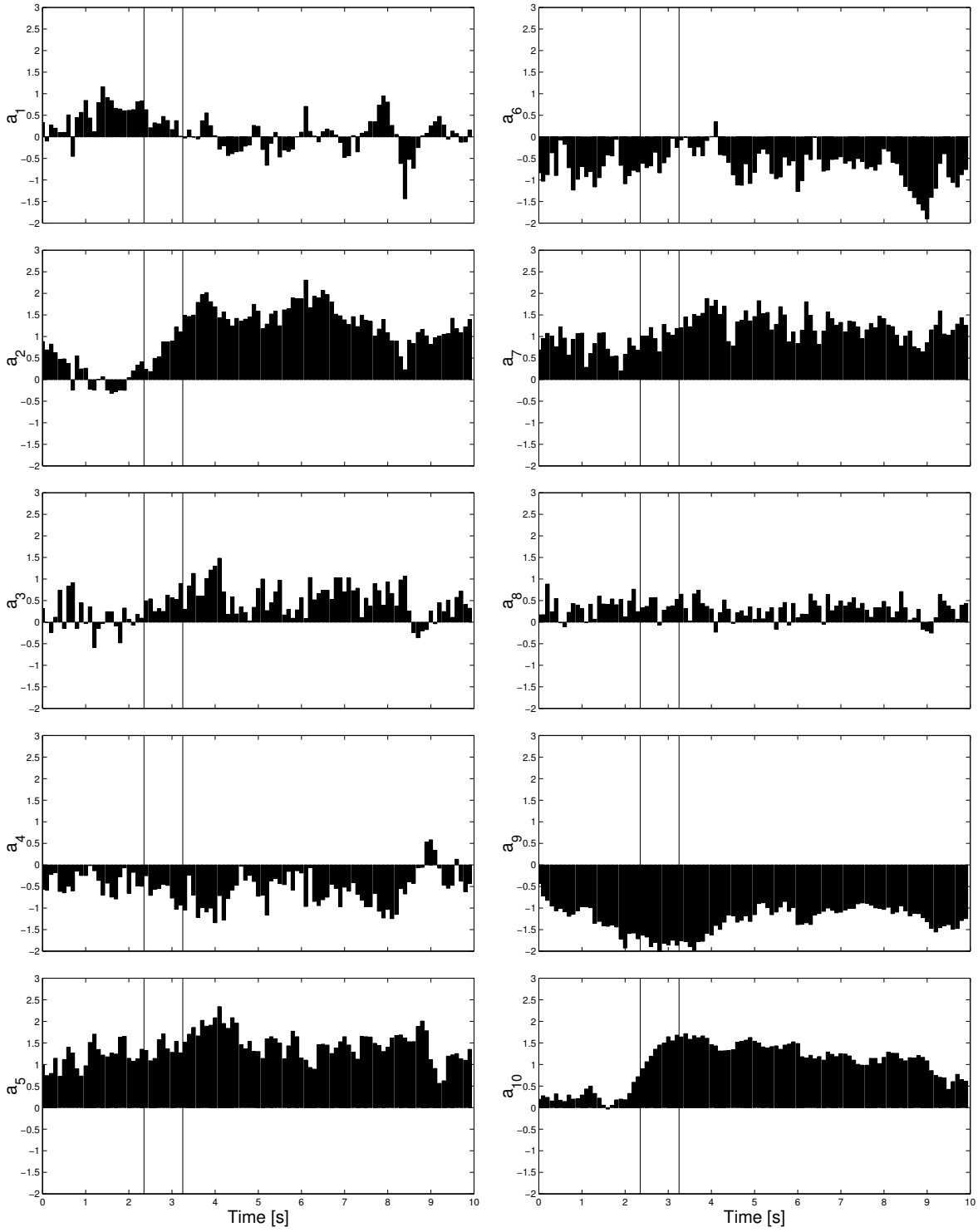

Figure 5.8: *Time history of amplitudes of first 10 POD modes. Vertical lines mark the time interval of the snapshots shown in figure 5.7.*

flows, the large scale deviations from the mean flow field may be governed by just a few modes, while complex flows like the flow in the Annex 20 room require a larger number. Due to the limited amount of energy contained in the small–scale motions, these are not captured until very high mode numbers (cf. mode 50 in figure 5.6). Thus, while the first few modes determine the large scale motions, the small–scale structures, such as the vortices marked in figure 5.7, appear as a combination of contributions from the higher order modes.

5.5 Conclusions

Velocity data has been obtained with particle image velocimetry in a domain covering a square region near the inlet of a scale model of the Annex 20 room. The flow near the inlet of the Annex 20 room can be divided in two flow regions: the high–velocity wall jet region at the top boundary and the low–velocity region in the domain below the wall jet. The latter is of special interest because this is where persons will be influenced by the air movements. In the low–velocity region, the velocity fluctuations are larger than the mean velocities. The reason for this is that the low–velocity region sometimes has flow patterns very different from the mean flow.

POD analysis offers new insight into the flow structures. The first ten POD modes can roughly be divided into modes mainly related to the wall jet and modes that relate to the complete domain. The first two modes (which contain most energy) have horizontal in- or outflow at the lower part of the right boundary of the domain. This shows that fluid often enters (and sometimes leaves) the low–velocity region in "bursts" of nearly horizontal velocity. This is in contrast with the mean velocity field, where fluid enters at an angle of about 45 degrees to the boundary. The next modes representing flow structure in the low–velocity region are modes 5-7, which all more or less show a single large vortex centered in the middle of the domain. This flow pattern is very different from the mean velocity field, but is often seen in the complete series of snapshots from the measurements.

The wall jet region contains "bursts" of small regions with high velocities, which normally cover x–intervals of about 20–40% of the domain width. These bursts are seen at different positions in all the first eight POD modes. In the first two modes, the bursts are situated near the inlet. This indicates that there is a connection between the appearance of the burst and an inflow (positive or negative) into the domain near the bottom wall. The bursts could be related to three-dimensional flow structures in the wall jet and to the pressure fluctuations in the room. A more thorough investigation of this would require measurements in the z–direction and probably longer time series.

The investigation of the POD mode coefficients for a time series show that there are two different time scales in the flow: a rapid time scale related to the wall jet and a slow time scale related to flow structures in the low–velocity region. It is interesting to note that the slow time scale can be many seconds. This is significantly longer than the integral time scale of 1.5 s found by integration of the autocorrelation of an LDA signal in a single point. This stresses the fact that the flow structures have their own dynamics and that they can not be explained alone by the flow being turbulent. A problem is that the long time scales indicate that a longer time between recordings

would possibly yield statistically more accurate results of the POD-analysis.

A traditional CFD simulation using Reynolds–averaged Navier–Stokes equations and a turbulence model like the k-ϵ model has difficulty in predicting the actual flow in the room. However, even a perfect Reynolds–averaged calculation yielding the result presented in figure 5.3 would not represent the actual flow very well. For human comfort, parameters like draught (maximum local velocities) and transport of pollutants are important. To estimate such factors correctly by calculations, it is necessary to make time-dependent simulations. This makes Large Eddy Simulation (LES) an obvious choice. Results from LES calculations could then be compared to the present measurements e.g. by comparison of the results of a POD analysis.

Chapter 6

Further Investigations of the Annex 20 PIV Data

The investigations of the present chapter were carried out for the same PIV data as in chapter 5 and hence the following should be read as parallel to the contents of this chapter. The first section addresses the length scales of the flow and the second section discusses the results of application of LSE. Both subjects are shown to be connected to the results of the POD analysis of chapter 5.

6.1 Length scales

As discussed in chapter 5, the number of POD modes necessary to capture all details of a given flow depends on the complexity of the flow. The flow in the Annex 20 room is quite complex and hence it makes sense to consider a high number of modes for a thorough investigation. In many applications the accuracy of the measured data may be the limiting parameter. Of course the numerical accuracy of the data is in itself limited, but what defines the upper limit of detail in practice is most likely the resolution of the flow field. To verify this the characteristic length scales (macro scales) of the flow have been calculated for two representative y–values in the measurement domain considered. Figure 6.1 shows the spatial correlation coefficients for u and v in the x–direction, defined by:

$$f(\Delta x) = \frac{\langle u'(x)u'(x+\Delta x)\rangle}{\langle u'(x)^2\rangle} \tag{6.1}$$

and

$$g(\Delta x) = \frac{\langle v'(x)v'(x+\Delta x)\rangle}{\langle v'(x)^2\rangle} \tag{6.2}$$

at $y \approx 192$ mm and $y \approx 102$ mm. For a given separation, Δx, the values of f and g were found as the average of $f(\Delta x)$ and $f(-\Delta x)$ and $g(\Delta x)$ and $g(-\Delta x)$, respectively, starting in the middle of the domain with $\Delta x = 0$ for $x \approx 100$ mm. It is noted that the spatial correlation for u at $y \approx 192$ mm does not reach zero. Although small scale structures frequently appear in this region, large scale motions are also present due to the bursts appearing in the wall jet, which explains this behavior.

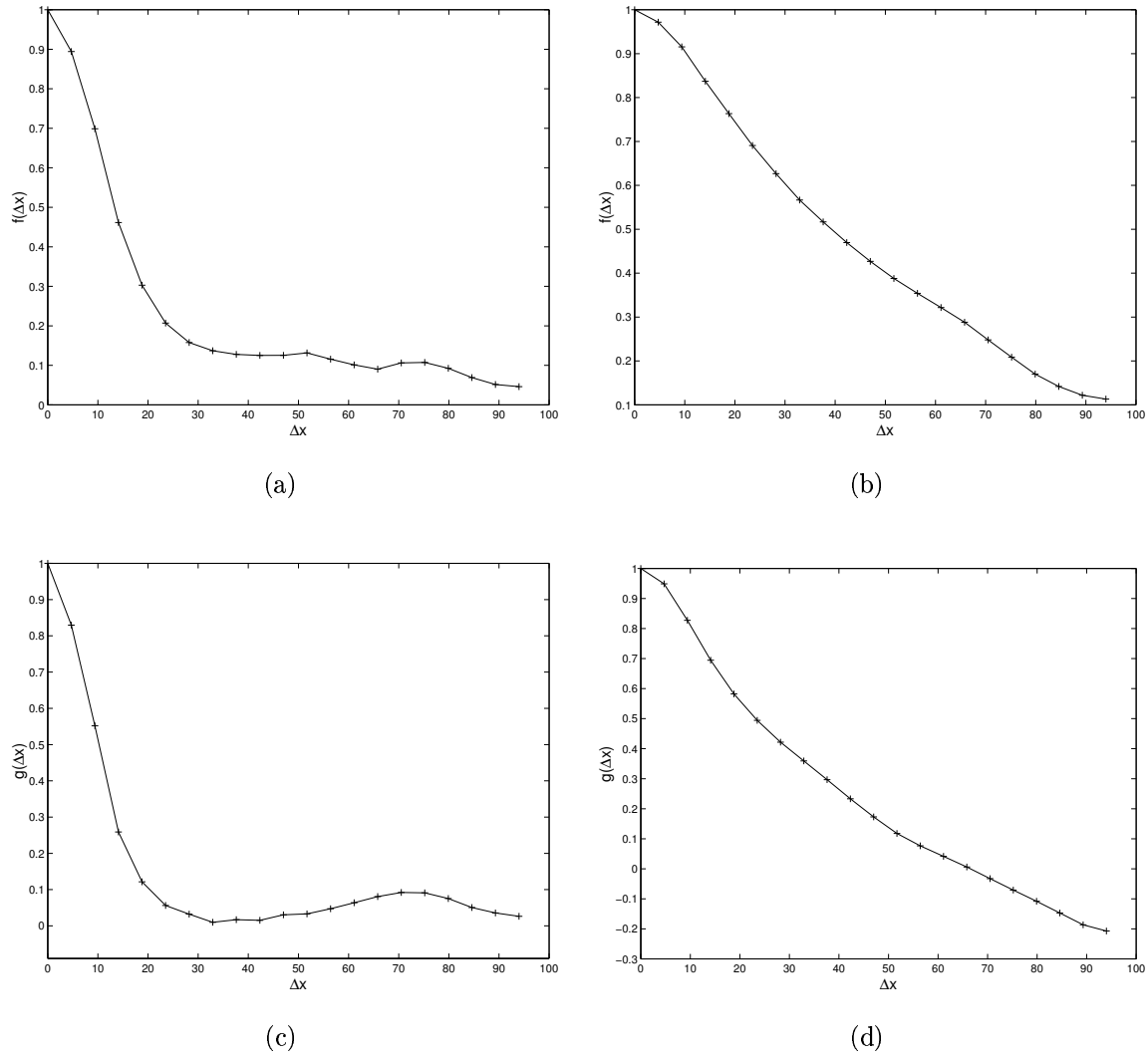

Figure 6.1: *Spatial correlations in x–direction.* (a) *uu–correlation at* $y \approx 192$ *mm.* (b) *uu–correlation at* $y \approx 102$ *mm.* (c) *vv–correlation at* $y \approx 192$ *mm.* (d) *vv–correlation at* $y \approx 102$ *mm.*

The characteristic length scales, Λ_f and Λ_g, at the given y–values were determined by numerical integration of the functions given in (6.1) and (6.2), yielding:

$$\Lambda_f = \begin{cases} 21.7 \text{ mm} & \text{at} \quad y \approx 192 \text{ mm} \\ 45.0 \text{ mm} & \text{at} \quad y \approx 102 \text{ mm} \end{cases}$$

and

$$\Lambda_g = \begin{cases} 14.1 \text{ mm} & \text{at} \quad y \approx 192 \text{ mm} \\ 24.1 \text{ mm} & \text{at} \quad y \approx 102 \text{ mm} \end{cases}$$

The scales at $y \approx 192$ mm are smaller than the ones at $y \approx 102$ mm. This was to be expected since the larger value of y corresponds to a position within the wall jet, just below the ceiling where the high turbulence levels indicate smaller length scales. At

$y \approx 102$ mm the turbulence levels are lower and hence the length scales of the flow larger.

As described in section 5.3 of chapter 5, the flow field consists of 41×42 vectors in total. This gives a velocity vector about every 4.8 mm. Theoretically, four (two by two) vectors are needed to resolve a given eddy. However, this is an absolute minimum value and nine (three by three) are more suitable in practice. With one vector each 4.8 mm this requirement gives a minimum detectable eddy size of 14.4 mm, which corresponds very well to the length scale found from the vv–correlation at $y \approx 192$ mm. Thus, as the spatial correlations are directly related to the derivation of the POD, the results suggest that the spatial resolution of the flow field is the limiting factor when considering the level of detail which may be extracted from the POD modes.

6.2 Extraction of dominant structures using LSE

As explained in chapter 4, the LSE provides an estimate of a conditional velocity field given an event. In this way, if a recurring, dominant flow structure can be related to a given event it must be expected that the LSE given this event will (at least to some extent) reproduce this structure. Further, since it is based on two–point spatial correlations, the LSE will also reveal whether events at certain positions are correlated with events at other positions. Referring to the discussions of section 5.4.2 of chapter 5, this makes LSE a perfect tool for a verification of the results found from the POD analysis.

6.2.1 Most energetic structures

In order to investigate to which degree the LSE will reproduce the most energetic structures of the flow, the two first POD modes i.e. 1 and 2 are considered.

Figures 6.2(a) and 6.2(c) show single-point LSEs with event vectors specified near the inlet of the Annex 20 Room at position $(x, y) \approx (40, 190)$ mm. The two event vectors were taken from the data fields specifying POD modes 1 and 2, respectively. These are displayed to the right of the LSEs in figures 6.2(b) and 6.2(d). The single-point estimates produce bursts near the location of the event point, while the velocities vanish in the rest of the domain and hence fail to capture the overall flow patterns of the two POD modes. Bearing in mind that the LSE provides an estimate of a conditional average given a specified event, this indicates that several different flow patterns are associated with the single vectors specified at this point. Indeed, as already pointed out, the two first POD modes indicate a correlation between inflow as well as outflow at the lower right boundary and a burst in positive x–direction near the inlet. The frequent appearance of bursts near the inlet in the data ensemble, combined with the complexity of the flow in general, suggests that other flow structures may also be related to this particular event. Consequently, the single-point LSE does not lead to an explicit result. It should still be noted, however, that although the single-point LSEs fail to capture the overall shape of the two POD modes, they still confirm the dominant nature of the bursts in the jet region. The results shown in figures 6.2(a) and 6.2(d) would not have been found from an event vector pointing in positive x–direction just downstream of the jet inlet if a burst had not been a frequently occurring structure in this region.

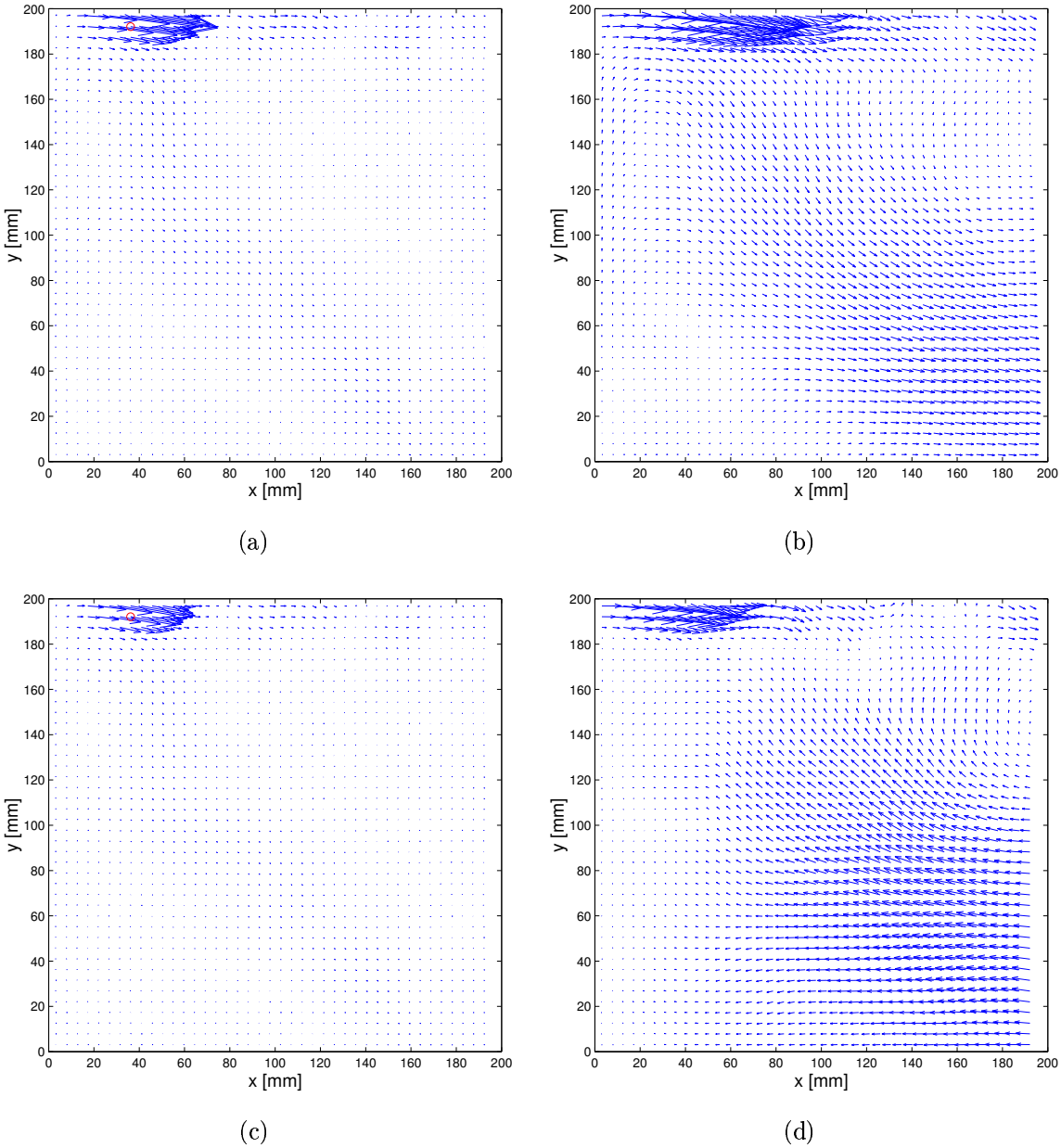

Figure 6.2: *Single-point LSEs with event vector at* $(x, y) \approx (40, 190)$ *mm.* (a) *Event data taken from POD mode 1.* (c) *Event data taken from POD mode 2.* (b) *and* (d) *POD modes 1 and 2, respectively.*

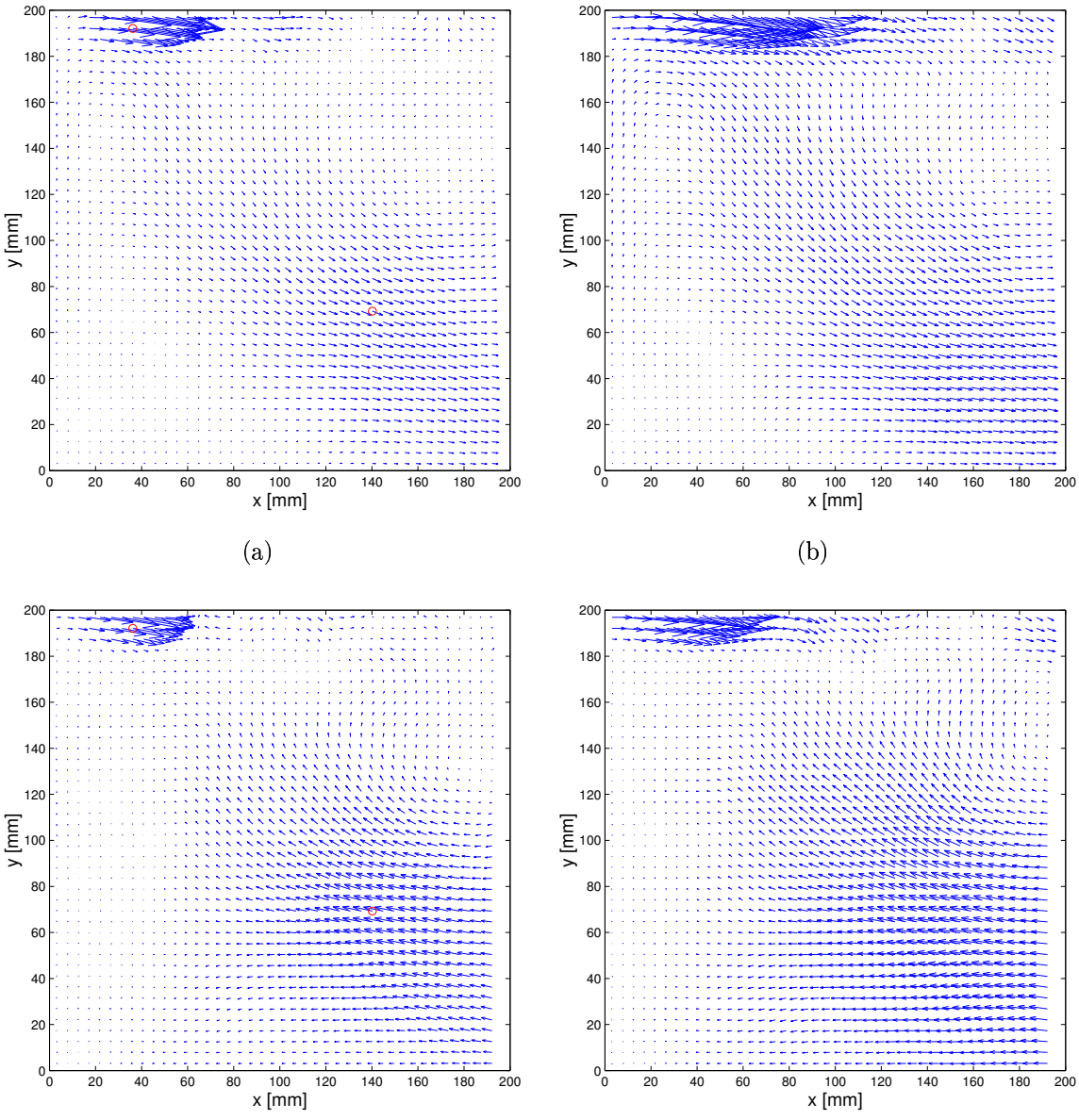

Figure 6.3: *Two-point LSEs with event vectors at* $(x, y) \approx (40, 190)$ *mm and* $(x, y) \approx (140, 70)$ *mm, respectively.* (a) *Event data taken from POD mode 1.* (c) *Event data taken from POD mode 2.* (b) *and* (d) *POD modes 1 and 2, respectively.*

The plots in figure 6.3 present two-point LSEs with an event vector specified in the lower left part of the domain at $(x, y) \approx (140, 70)$ mm as well as near the inlet. The event data at the second point, which again were taken directly from the POD modes, consist of vectors pointing towards and away from the inlet, respectively. The two-point LSEs do a much better job in reproducing the flow patterns captured by the first two POD modes. Including a second event vector, the ambiguity associated with the single-point event is eliminated and the result confirms the correlation between inflow/outflow at the lower right boundary and a burst in positive x–direction near the inlet.

6.2.2 Increasing level of detail

Although a correlation between them has been verified, the two connected flow regions (burst at inlet + bulk flow at lower right) in POD modes 1 and 2 must be characterized as individual flow structures. To investigate the performance of LSE with an increasing number of individual flow structures, the flow pattern in POD mode 10 including three vortices is now considered.

Figure 6.4 shows POD mode 10 together with LSEs based on events of increasing complexity. It is noted that the vectors have been scaled by a factor of 1.5 compared to the plots in figure 5.6 to intensify the details. The event data were taken directly from the POD mode at the specified locations. Yielding but a hint of a vortex, above and to the right of the center of the domain, the single-point LSE in figure 6.4(b), with a vector specified at $(x, y) \approx (100, 100)$ mm, fails to capture the overall flow pattern of the tenth POD mode. Interestingly, the single-point event indicates the presence of a small burst in the wall jet region a little downstream of the inlet reminiscent of the ones found in POD modes 1 and 2. Referring to the observations above, this can be explained by the fact that the primary outcome of the single-point event is a bulk flow region representing an outflow from the domain at the lower part of the right boundary.

To improve the estimate a second event point has been added in the LSE of figure 6.4(c). With an event vector at $(x, y) \approx (140, 20)$ mm pointing downwards and in the negative x–direction, the outflow at the lower part of the right boundary is reversed and the burst like event right after the inlet is suppressed. Further, the two-point LSE now qualitatively reproduces both the vortices in the left part of the domain: one just below and to the left of the middle and one at the lower left corner.

The vortex at the upper right appearing in combination with an inflow at the middle part of the right boundary was not revealed by the two-point LSE. This has been overcome in figure 6.4(d) where a three-point LSE, with the third event point specified at $(x, y) \approx (180, 100)$ mm, now completely reproduces the overall flow pattern of POD mode 10. Although the vectors are shorter than in the original POD mode far away from the event points, the three vortical structures as well as the singular point just below the middle to the right are all captured by the three-point LSE.

More event points would further improve the reconstruction, but the three-point event LSE suffices for a representation of the three vortices. Assuming that this is not a unique feature of the particular flow pattern, the result leads to the conclusion that the minimum number of event points needed to reconstruct a given flow field is equal to the number of individual flow structures in this field. It should be noted,

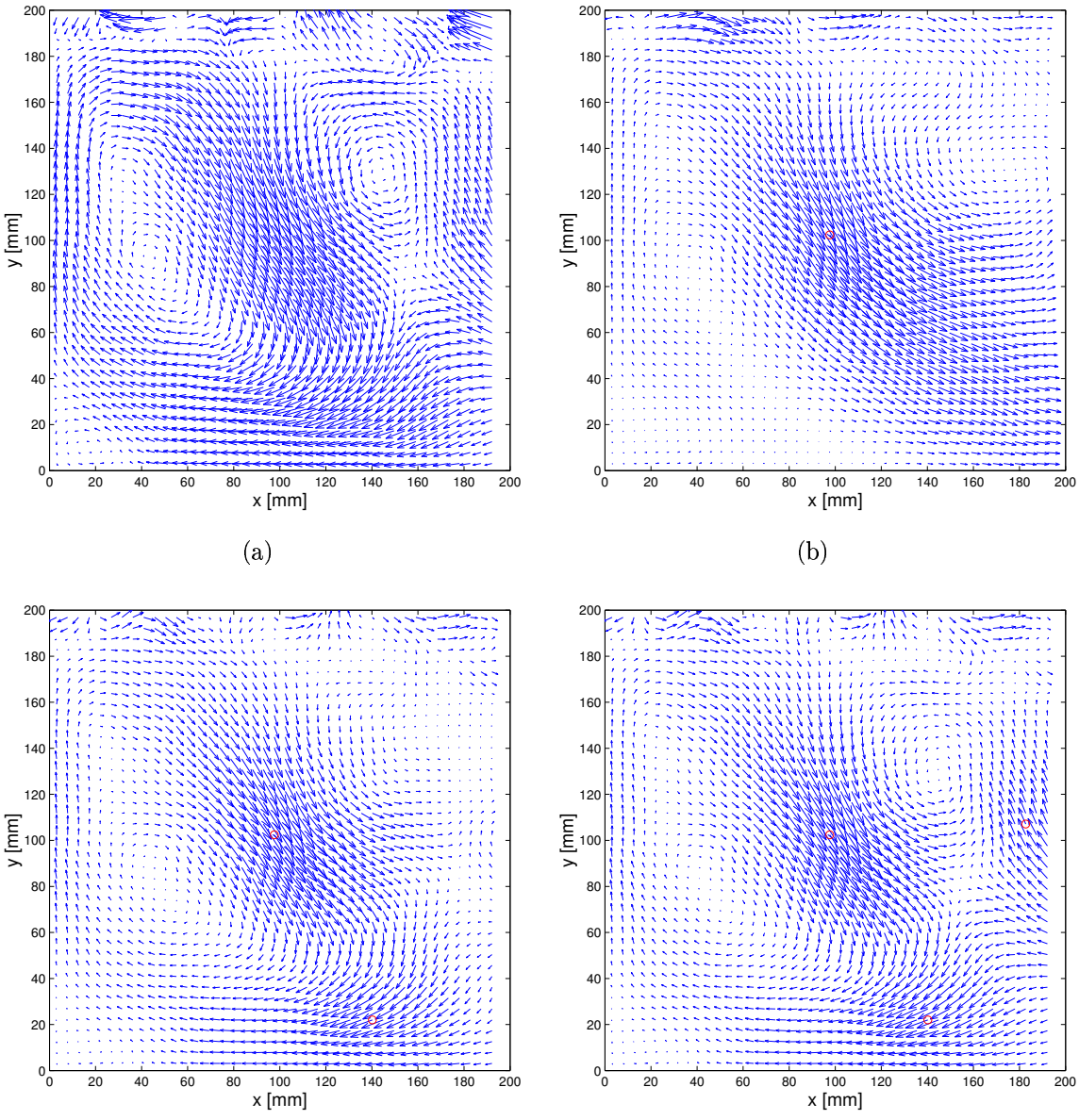

Figure 6.4: *LSEs of POD mode 10 using events of increasing complexity.* (a) *POD mode 10.* (b) *Single-point estimate with event at domain center.* (c) *Two-point estimate with events at center and lower right.* (d) *Three-point estimate with events at center, lower right, and middle right.*

however, that this rule of thumb will apply only if the events are chosen optimally with respect to location and strength. Some optimization was required to determine the locations used for the LSEs in figure 6.4. Further, the numerical values of the data were chosen optimally in the sense that they were taken directly from the POD mode. These observations again stress the fact, which was already pointed out in chapter 4, that the choice of event vector is critical to the outcome of the LSE.

6.3 Summary

This chapter presented further investigations of the PIV data which were analyzed in detail from a POD point-of-view in chapter 5.

A conventional determination of the characteristic length scales was made by integrating the spatial correlation functions in the domain considered. As expected, the results showed that the smallest length scales are found in the regions with the highest turbulence levels. Further, the results indicated that the resolution of the flow field sets the lower limit for the level of detail which may be extracted from the POD modes.

Secondly, LSE was applied to extract the dominant structures found from the POD analysis. Considering the first two modes, it was found that the ambiguity connected with a burst in the jet region right after the inlet necessitated the use of two-point events for the LSE to fully reproduce the flow patterns of the two modes. In order to investigate the performance of LSE for flow fields containing several individual flow structures, the more detailed flow pattern of POD mode 10 was considered. While again demonstrating the vital importance of the choice of event vector, the results also showed that as a rule of thumb, the minimum number of event points, necessary for the LSE to satisfactorily reproduce a given flow pattern, is equal to the number of individual flow structures in this flow pattern.

Part C

Jet-in-crossflow

Chapter 7

Jet-in-crossflow Introduction

The present chapter may be viewed as an extended introduction to the following chapter, where the results of the analysis of SPIV measurements of a jet-in-crossflow (JICF) are presented. The first section introduces the JICF and includes a short review of previous work, some of which is based on methods conceptually different from the current approach, and some using data acquired from the same test facility as the dataset used for the present investigations. Secondly, a description of the experimental setup is given, and the conditions under which the data to be analyzed in chapter 8 were obtained are briefly discussed. Finally, the concepts of SPIV are explained including a short description of the application of this measurement technique in practice.

7.1 The jet-in-crossflow

A JICF, sometimes also referred to as a transverse jet (see e.g. [30]), covers basically any flow where a jet is issued transversely into a more or less uniform crossflow. When the incoming jet is deflected by the crossflow, a complex flow pattern results. This is of great importance to the mixing process that takes place between the two fluids. The phenomenon is encountered in a variety of practical problems like fuel injection, chemical unit operations, and V/STOL aircrafts[1]. An everyday example of a JICF is the issuing of smoke from a chimney into the atmosphere. Together with waste disposal into water bodies such as rivers, this makes it interesting also from an environmental point of view.

The JICF has been a topic of interest for about sixty years and numerous investigations have been carried out to describe the physics of this very complex flow problem. Some of the most important references numerical as well as experimental are listed in [62]. Only a few of these will be mentioned in the following. A comprehensive study was presented by Fric and Roshko in 1994 [30], who used visualization and hot-wire anemometry. Following their description, the existence of four different types of coherent structure are characteristic for the near field of the JICF. These are:

1. The jet shear–layer vortices

2. The system of horseshoe vortices

[1] Vertical and Short Take–Off and Landing aircrafts.

3. The (bound) counter–rotating vortex pair

4. The wake vortices

A sketch of the structures can be seen in figure 7.1. As the name suggests, the first

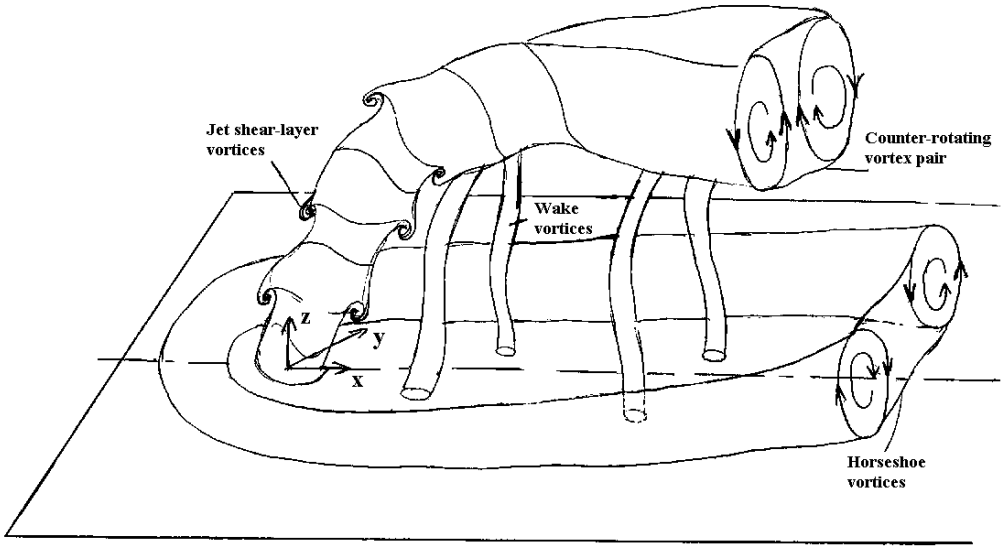

Figure 7.1: *The four types of coherent structures in the near field of the JICF. (From [62] by courtesy of the authors.)*

type of vortices originate at the shear–layer, which forms between the jet and the crossflow. With a crossflow from left to right and the jet pointed upwards the rotation will generally be counterclockwise upstream of the jet trajectory and clockwise on the downstream side. The second type of vortices arise near the wall and wrap around the jet core in a horseshoe–shape extending several jet diameters downstream. The third type, probably the most important of the four, is the counter–rotating vortex pair (CVP). A more thorough description of the CVP will be given in sections 8.2 and 8.3. Finally, the wake vortices, which were treated in particular detail by Fric and Roshko, extend vertically from the wall to the jet and are reminiscent of (but not equivalent to[2]) the classical wake vortices of, for example, flow around a cylinder (cf. section 1.1).

The work of Fric and Roshko has been accentuated due to its very informative nature regarding the different types of flow structures occurring in the JICF. Illustrative visualizations were also provided by Lim et al. [47], who, however, considered laminar flow only. As for numerical work, the large eddy simulations by Yuan and Street [99] and Yuan et al. [98] deserve to be mentioned. These were used, among other things, to study the entrainment of the JICF. More recently, elaborate LDA measurements were carried out by Özcan and Larsen [62] in the same test facility as the one used for the

[2]The flow around the jet does not separate from the jet, and hence no vorticity is shed into the wake [30].

present study. This work has acted as a precursor to a series of SPIV measurements, which were reported by Meyer et al. in [54] and [55]. In these papers the strength of SPIV in obtaining complete velocity statistics for an given flowfield in a short amount of time was illustrated, and it was shown how the classical Boussinesq approximation fails for a complex flow like the JICF. The work presented in this thesis focuses on structure identification based on velocity measurements (SPIV) and thus nicely supplements the work which has been done on the JICF so far.

7.2 Experimental setup

The data used for the present investigations were recorded in three mutually orthogonal planes at different positions in the flow near the jet exit. The configuration shown in figure 7.2 was used to obtain data in the x–z planes, referred to as y = const. planes. To acquire data in the x = const. planes (y–z planes), the cameras were kept in the same position as on figure 7.2 and the light sheet optics were placed above the wind tunnel to form a vertical laser–sheet parallel to the jet pipe. Keeping the light sheet optics in that position with the sheet turned 90° and moving the cameras up in front of the wind tunnel (to the original position of the light sheet optics), the final configuration was established and data for the z = const. planes (x–y planes) could be sampled. In all three cases the cameras and light sheet optics were mounted on the

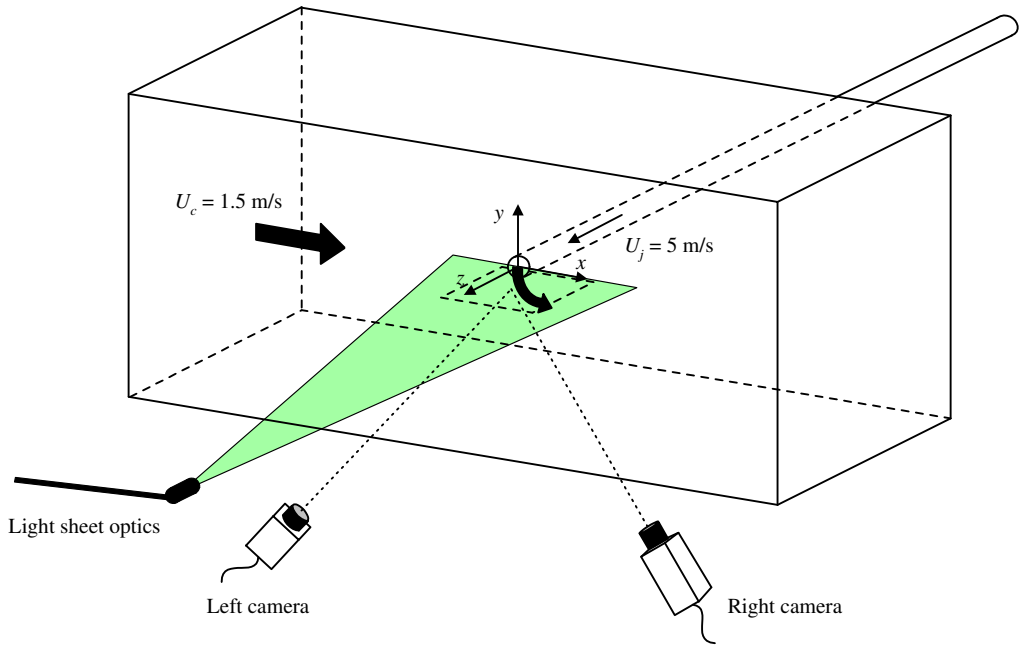

Figure 7.2: *Experimental setup for SPIV measurements of the JICF. The configuration shown corresponds to data acquisition in y = const. planes.*

same traversing unit. This way only one calibration (see section 7.3) had to be made for each configuration.

Figure 7.2 also shows the definition of the coordinate system of which the z–axis is chosen parallel to the jet and the x–axis in the direction of the mean crossflow. The mean crossflow velocity, U_c, was kept at $U_c = 1.5\frac{\mathrm{m}}{\mathrm{s}}$ and the mean jet velocity, U_j was equal to $5\frac{\mathrm{m}}{\mathrm{s}}$. With these values the jet-to-crossflow ratio, R, was fixed at $R = 3.3$, equivalent to the value used in earlier studies [62, 55, 98]. The jet diameter was $D = 24$ mm yielding a Reynolds number of 2400 based on U_c and D. The pipe flow forming the jet was turbulent and fully developed and the turbulent crossflow boundary layer approaching the jet exit was three jet diameters thick upstream of the jet. For further details the reader is referred to [62], where these conditions are documented and a thorough description of the component parts of the flow system is also provided.

The SPIV measuring equipment consisted of two Kodak MegaPlus ES 1.0 cameras and a double cavity Nd-YAG laser delivering 100 mJ energy per light pulse. The data collection was controlled by a Dantec PIV2100 processor. Seeding was supplied to the jet and crossflow separately from atomizers generating particles with a mean diameter of 1–3 μm from glycerine containing 15% water. The amount of seeding was adjusted to obtain a homogeneous distribution of particles in such a way that the presence of more than one flow source could not be detected from the PIV images. The sampling rate was limited by the acquisition system and was thus fixed at 0.33 Hz, evidently small enough to ensure uncorrelated measurements. Several positions were considered for each SPIV configuration of which only some will be treated the following chapter. Because of the different calibrations, the number of velocity vectors in a given vector map was different for each configuration. Table 7.1 summarizes the details of the 3D velocity data which are analyzed in chapter 8. The datasets marked with $^{(*)}$ have been treated in earlier publications [54, 55]. The unmarked data are previously unreported. Common for all datasets is that the images were processed using adaptive correlation

Measuring plane	Number of velocity vectors	Total number of samples
$y = 0$	33×36	999
$x = 4$ mm$^{(*)}$	34×35	200
$x = 10$ mm$^{(*)}$	34×35	200
$x = 16$ mm$^{(*)}$	34×35	200
$x = 24$ mm	34×35	1000
$x = 28$ mm$^{(*)}$	34×35	200
$x = 34$ mm$^{(*)}$	34×35	200
$x = 46$ mm$^{(*)}$	34×35	199
$z = 16$ mm	33×37	1000
$z = 32$ mm$^{(*)}$	36×35	658
$z = 48$ mm	33×37	1000

Table 7.1: *Overview of analyzed datasets.*

because of the large differences between the mean velocity in the jet core and the mean velocities in the regions away from the jet. The results presented in chapter 8 are related partly to mean flow characteristics and partly to investigation of dominant flow

structures. One of the tools used in connection with the latter is the proper orthogonal decomposition. As shown in table 7.1, some of the datasets consist of 200 samples each. These datasets will be used to describe mean flow statistics only, as a higher number is required to ensure a reliable result of a POD analysis.

The final section of the present chapter provides an introduction to the concepts of stereoscopic PIV.

7.3 Stereoscopic PIV

The basic principle of SPIV is the same as for ordinary PIV. Cross–correlation of two successive images of tracer particles in a given plane yields the local displacements and dividing by the time separation between the two images the velocity field results. In SPIV two cameras record the successive images simultaneously. Two different 2D velocity fields are obtained and from these all three velocity components can be derived. The two most common configurations are the translation method and the angular displacement method. In the former, the optical axes of the two cameras are both kept orthogonal to the object plane, simply displaced a certain distance from each other. In the latter approach, the cameras are tilted with respect to the object plane. This method has been used for the present study. The configuration distinguishes itself by being flexible with respect to positioning of the two cameras in space. Also a larger overlap area between the field-of-views of the two cameras can be obtained using the angular displacement method. One drawback is that the inclined viewing angles cause a defocusing of the images. To remedy this the image planes have to be tilted slightly as well. The optical configuration is then said to satisfy the *Scheimpflug condition.*

Figure 7.3 sketches the principle of the angular displacement method. The angular

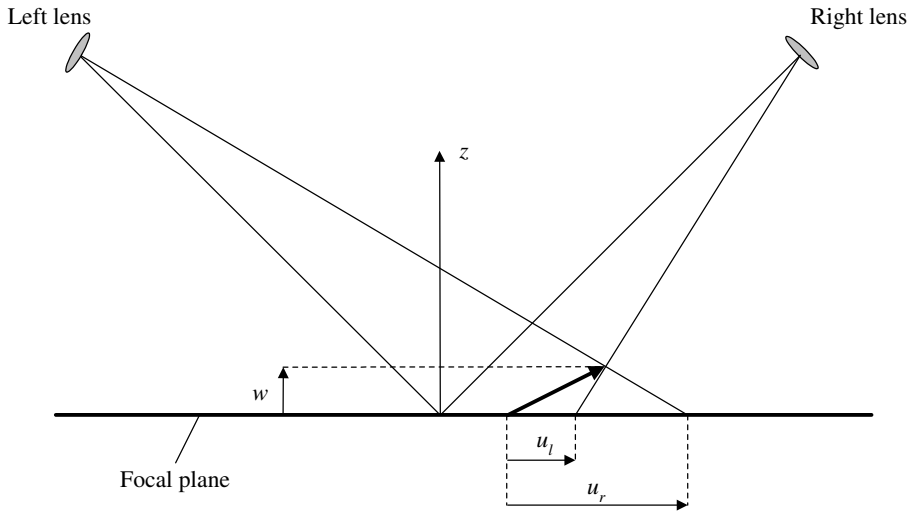

Figure 7.3: *Principle of the angular displacement method in SPIV.*

displacement shown is close to 90°. Theoretically, the best results are obtained with an angle of exactly 90°. Sometimes this may not be possible due to restrictions from

the physical setup. However, smaller angles are usually acceptable in practice. The figure shows a 2D view in a plane orthogonal to the y axis. The vector corresponding to the true displacement, (u, v, w), is represented by the arrow in bold. The left and the right camera see the in-plane displacements (u_l, v_l) and (u_r, v_r), respectively. Having measured these displacements knowing all relevant geometrical parameters (angles, distances, etc.), in principle, the true displacement can be calculated. However, in an actual experiment it is often very difficult if not impossible to measure lengths and angles with sufficient accuracy. Hence, in practice, the true velocity field is reconstructed from a "calibration", which is calculated prior to the measurements. This technique can be summarized as follows.

First a *calibration target* is placed in the object plane and carefully aligned with the laser-sheet. The calibration target defines the x and y axes with origin at the center of the target. It may not be possible to place the target in such a way that the origin defined by the calibration is coincident with the origin of the "physical" coordinate system. This has indeed been the case for the JICF where the physical origin is defined at the jet center. Hence the distance from the target to the jet center was carefully measured before each calibration in the present experiments. With the target in place, images are recorded at different positions traversing through the light-sheet. From these images a linear or higher order calibration is calculated and stored. The linear calibration based on simple geometrical optics was used for the present measurements. Higher order schemes are necessary if non-linear effects such as image distortion (due to poor camera lenses) or refraction (e.g. measuring from air into water) are present. Having obtained the calibration, PIV images are recorded with the two cameras and processed to yield (u_l, v_l) and (u_r, v_r). For each measurement series the velocity fields from the two cameras are finally processed using the calibration and the reconstructed 3D velocity fields result. In theory the reconstruction corresponds to solving four equations with three unknowns in a least-squares manner at each point in the domain.

The present section serves as an introduction to the concepts of SPIV and on how to use this technique in practice. For a more thorough theoretical description the reader may want to refer to chapter seven of the textbook by Raffel et al. [71] or the review papers by Prasad [70] and Prasad and Adrian [68]. The latter focuses on SPIV applied to liquid flows, which is particularly complicated due to the refraction of light at the liquid-air interface.

7.4 Summary

In this chapter the JICF has been introduced and the four most characteristic flow structures appearing in the near field of the jet exit have been briefly discussed. These are the jet shear–layer vortices, the system of horseshoe vortices, the counter rotating vortex pair, and the wake vortices. Also a short review of previous work on the JICF and its relation to the current investigations was provided.

Secondly, the experimental setup used to obtain the data for the present study was described and it was explained how different configurations has facilitated acquisition of data in mutually orthogonal planes near the jet exit. The different flow parameters were stated and the experimental equipment described. Furthermore, an overview of

the data to be analyzed in chapter 8 was given in table 7.1.

Finally, for completeness, a description of the concepts of SPIV was provided. The description served as an introduction to SPIV focusing on the application of this measurement technique in practice.

Chapter 8

Jet-in-crossflow Results

The present chapter reports the results of the analysis of the SPIV measurements of the JICF. As mentioned in the previous chapter, data was obtained at different positions in three mutually orthogonal planes. The first section focuses on the symmetry plane, $y = 0$, and the following two sections are devoted to a description of the data obtained in a number of $x = \text{const.}$ and $z = \text{const.}$ planes. In all three cases the mean velocity fields are displayed and POD analyses carried out aiming at a complete description of the mean properties and dominant structures of the JICF.

8.1 The symmetry plane ($y = 0$)

The x–z plane at vertical position $y = 0$ is symmetric in a mean flow sense. The instantaneous flow realizations are highly three-dimensional as a result of the crossflow encountering the jet flow. In the following, the mean velocity field near the jet exit in the $y = 0$ plane is shown and it is discussed how the jet trajectory can be determined from this field. Secondly, the jet shear–layer vortices are discussed, and finally a comparison of POD analyses is made using two and three velocity components, respectively.

8.1.1 Mean field and jet trajectory

Figure 8.1 shows the mean velocity field, (U, W), obtained from SPIV measurements in the $y = 0$ plane. The coordinates are given on dimensionless form as $(x, z)/D$ and the velocities have been scaled by a factor of 0.1, so that e.g. $5\frac{\text{m}}{\text{s}}$ corresponds to 0.5 units on the x axis thus yielding suitable vector lengths. In the top right corner a vector of length equal to the mean crossflow velocity, $U_c = 1.5\frac{\text{m}}{\text{s}}$, has been included for reference.

Very low velocities are found just after the jet exit (first two rows of vectors for $-0.5 < x/D < 0.5$). This erroneous result is due to a shortcoming of PIV for this particular flow situation. In the two successive PIV images the particles just outside the jet exit on the second image are still inside the jet pipe on the first image. This causes a velocity bias towards zero and hence the wrong result. However, the error is limited to this small area and does not affect the data in the rest of the domain.

The thick red line extending from the origin to the top of the field at $x/D \approx 1.4$, indicates the *jet trajectory*. The jet trajectory is determined as the locus of points traced

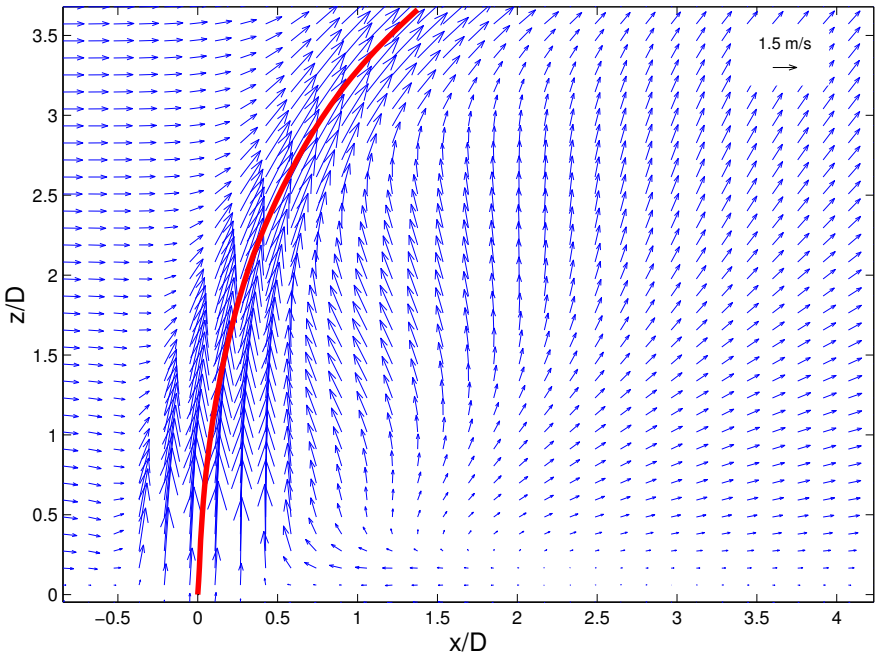

Figure 8.1: *Mean velocity field in $y = 0$ plane with indication of jet trajectory.*

out by the mean streamline[1] originating from the center of the jet. The approach was introduced by Yuan and Street [99], who concluded it to be superior to other definitions. For the jet-to-crossflow ratio in the present study the streamline trajectory is practically coincident with the locus of points describing the maximum velocity magnitude. With lower R the maximum velocity trajectory rises above the streamline trajectory because the crossflow fluid is accelerated over the jet [62]. This also explains why the streamline trajectory is superior to a trajectory determined, for instance, by the maximum velocity magnitude.

On close inspection the velocity vectors near the wall just upstream of the jet exit are seen to be pointing slightly downwards. This is connected to the formation of the horseshoe vortices which result from separation of the boundary layer. The actual vortex is not visible in the current plot due to insufficient spatial resolution. For a nice illustration the reader may refer to [62]. The fact that a horseshoe vortex can be identified from the mean flow field leads to the conclusion that it has mean flow definition. This is also the case for the counter rotating vortex pair (CVP) as will become apparent in the following sections. In fact, the large region with negative velocities in the x–direction downstream of the jet, seen in figure 8.1, is a direct consequence of the presence of the CVP. Contrary to these two types of vortices the jet shear–layer vortices (JSV) and the wake vortices are intrinsically unsteady and can not be discerned from the mean velocity fields. In the following subsection the mean vorticity field of the $y = 0$ plane is described and the existence of the JSV is illustrated by means of vorticity contours from an instantaneous flow realization and its fluctuating part.

[1]Mean streamline: streamline educed from the mean velocity field. As the mean velocity normal to the $y = 0$ plane is zero, the sectional streamlines and streamlines are identical.

8.1.2 Vorticity and the JSV

Figure 8.2 displays contours of the y–component of vorticity in the symmetry plane. The jet trajectory is represented by a thick black line. The vorticity has been made

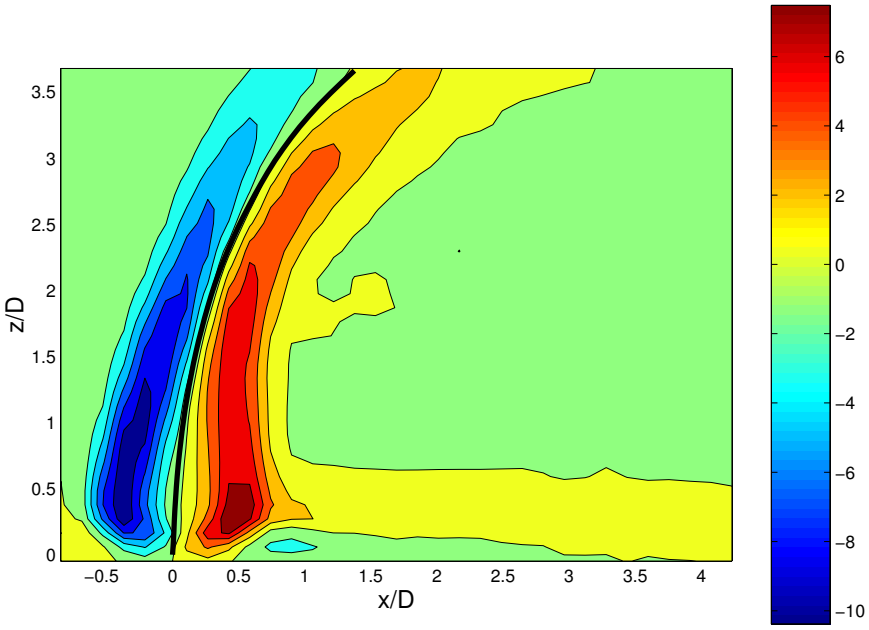

Figure 8.2: *Mean vorticity field, $\omega_y^*(x^*, z^*)$, in $y = 0$ plane.*

non-dimensional by the jet diameter and the mean crossflow velocity so that:

$$\omega_y^* = \frac{\partial U^*}{\partial z^*} - \frac{\partial W^*}{\partial x^*} \tag{8.1}$$

where

$$U^* = U/U_c,\ W^* = W/U_c,\ z^* = z/D,\ \text{and}\ x^* = x/D$$

Referring to equation (8.1) and comparing with the mean velocity field shown in figure 8.1 it is clear that the sudden increase in W with x at the upstream side of the jet trajectory is responsible for the global vorticity minimum at this location. Contrarily, the mean velocity in the z–direction drops with x downstream of the jet trajectory resulting in positive values of ω_y^*. Just below $z/D = 0.5$ the mean u–velocity grows from negative values to about zero when moving upwards. This further contributes to the increase in vorticity thus creating the local maximum at $(x/D, z/D) \approx (0.5, 0.5)$.

Using the dimensionless variables defined by equation (8.1) the result can be compared with the results derived from the LDA measurements performed by Özcan and Larsen [62]. The plot showing the ω_y^*–contours found by these authors has been reproduced in figure 8.3. Evidently, the two results are virtually identical both qualitatively and quantitatively. This observation indicates that the SPIV data produced for the present investigations is of high quality.

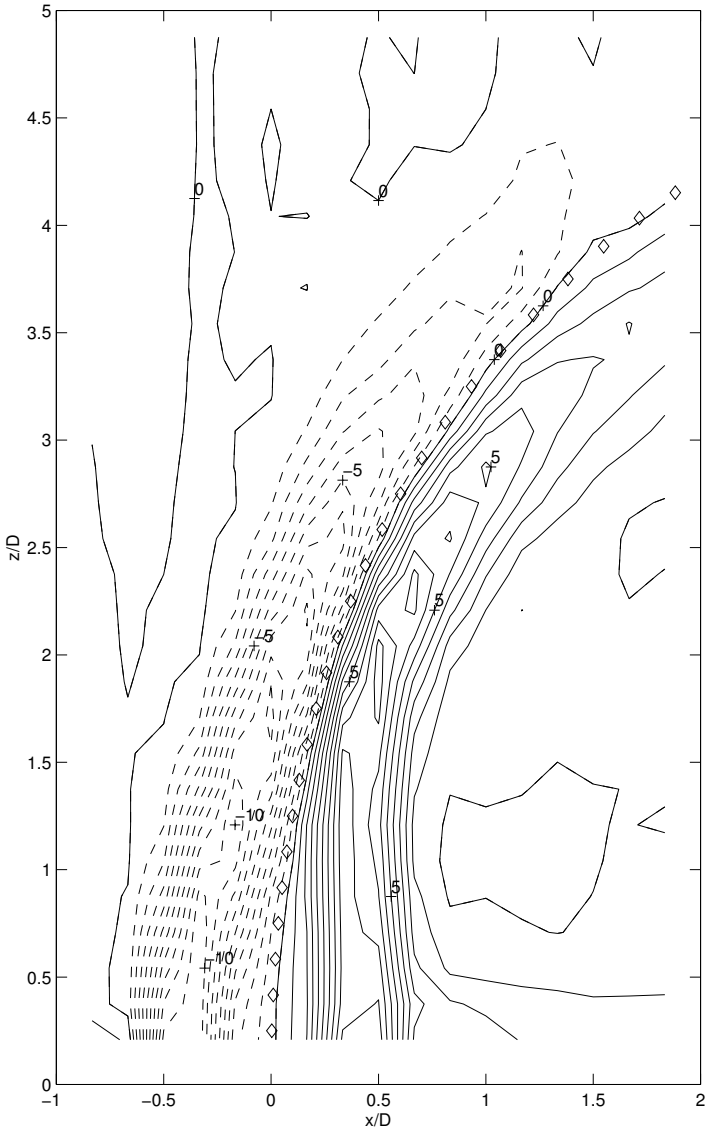

Figure 8.3: *Mean vorticity field, $\omega_y^*(x^*, z^*)$, in $y = 0$ plane determined from LDA measurements by Özcan and Larsen [62]. (Reproduced with permission).*

The shear–layers forming up– and downstream of the jet trajectory cause a continuous production of jet shear–layer vortices (JSV). The identification of the JSV is complicated by the strong shearing motion of the mean flow field. Figures 8.4(a) and 8.4(b) show an example of a vector plot of an instantaneous flow realization (vector lengths scaled by 0.1) and the associated vorticity contours. No vortical structures can be distinguished from the instantaneous velocity field which is dominated by the mean jet flow. The instantaneous vorticity contours reveal several maxima (negative and positive, respectively) on each side of the jet which may be related to the presence of JSV. However, these maxima result both from the presence of the JSV and the mean shearing motion. The plots in figures 8.4(c) and 8.4(d) show the fluctuating part of the instantaneous velocities (vector lengths scaled by 0.1) and the

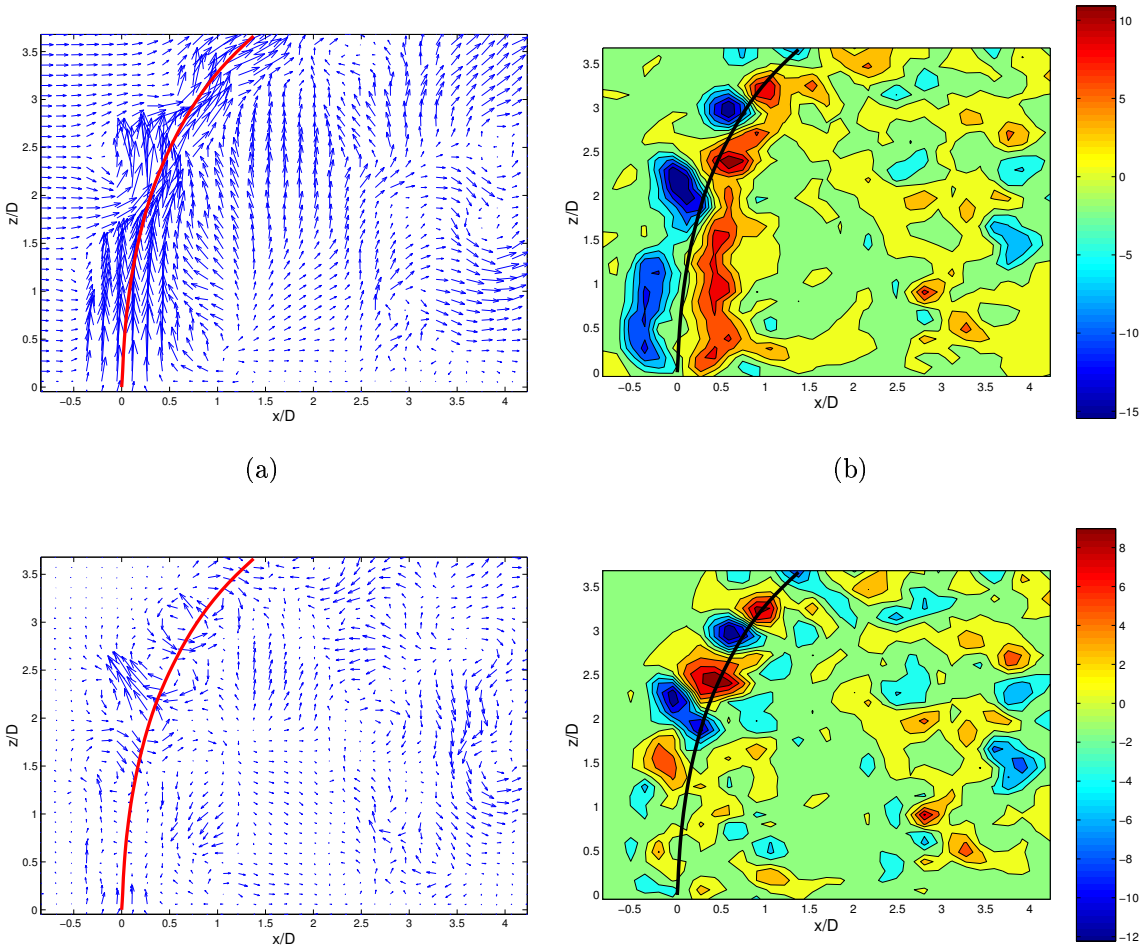

Figure 8.4: *Visualization of JSV.* (a) *Instantaneous velocity field.* (b) *Instantaneous vorticity contours.* (c) *Fluctuating velocity field.* (d) *Fluctuating vorticity contours.*

vorticity contours derived from this vector field. Comparing the two results leads to the following conclusions. Firstly, the negative and positive vorticity maxima found in figure 8.4(c) up– and downstream of the jet trajectory right after the jet exit are due to shearing motion only. Vortical structures in this region are neither revealed by the fluctuating velocity field in figure 8.4(c) nor by the fluctuating vorticity contours shown in figure 8.4(d). Secondly, the vorticity maxima in figure 8.4(b) at positions $(x/D, z/D) \approx (-0.2, 2.2)$, $(x/D, z/D) \approx (0.5, 2.4)$, $(x/D, z/D) \approx (0.5, 3)$, and $(x/D, z/D) \approx (0.9, 3.2)$ are all representative of true vortical motion. The negative vorticity peaks at $(x/D, z/D) \approx (-0.2, 2.2)$ and $(x/D, z/D) \approx (0.5, 3)$ are simply enhanced by the mean shear (cf. the colorbars). Further, the vorticity maximum caused by the vortex at $(x/D, z/D) \approx (-0.2, 2.2)$ is slightly displaced downstream in the contours of the instantaneous vorticity field. Finally, a vortical structure with positive rotation is found at $(x/D, z/D) \approx (-0.2, 1.5)$. Being situated upstream of the jet trajectory this vortex was obscured by the mean shear when considering the full instantaneous velocity field.

The current example is representative of many of the realizations of the complete dataset in the $y = 0$ plane. An interesting observation is that counterclockwise and clockwise rotating JSV are not necessarily situated up– and downstream of the jet trajectory, respectively. The explanation is that the position of a vortical structure in a given realization depends on the instantaneous velocities. The vortices are created as a result of the shearing motion and are convected and stretched by the local mean as well as fluctuating velocity. Common for the JSV is that they are all of the same spatial extent and that they are situated *near* the jet trajectory.

As a final point, it should be mentioned that the JSV are not to be compared with the classical ring vortices which are seen for instance shortly after the exit of a free circular jet. This fact was pointed out by Lim et al. [47] who showed that the CVP, which is initiated right after the jet exit in the JICF, inhibit the formation of ring vortices.

To further analyze the dominant structures of the JICF as viewed in the $y = 0$ plane POD analyses including two and three velocity components, respectively, have been carried out. In the the following, where the results of these investigations are presented, the POD modes resulting from the 2D and 3D analysis will be referred to as 2D and 3D POD modes, respectively.

8.1.3 2D POD analysis

The eigenvalue spectrum showing the relative energy content of the first 20 2D POD modes is shown in figure 8.5. The first 20 2D modes capture just above 51% of the total energy in all. The energy content of the individual modes is seen to be quite low. Also the curve decays relatively slowly. This indicates that many modes are needed to fully describe the details of a given snapshot. A reasonable result considering that the fluctuating part of the velocity field is dominated by small scale structures related to the dynamics of the JSV.

Figure 8.6 shows the first 2D POD mode and the variation of the corresponding POD coefficient with the first 50 uncorrelated snapshots of the dataseries taken in the $y = 0$ plane. The vectors have been scaled by a factor of 2 to yield suitable lengths

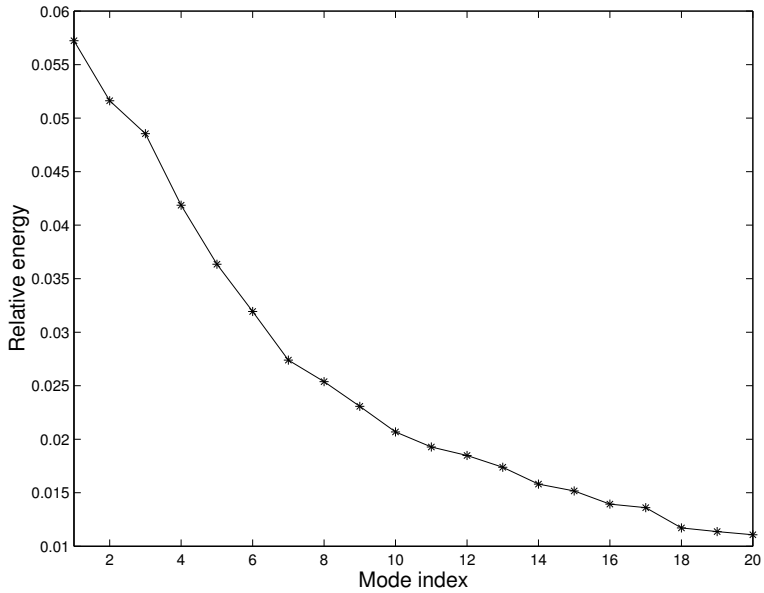

Figure 8.5: *Relative energy of 2D POD modes in $y = 0$ plane.*

when plotted against $(x/D, z/D)$. The large scaling factor (compared to the velocity plots) is necessary because of the normalization carried out when constructing the POD modes. The mean streamline jet trajectory is indicated by a thick red line.

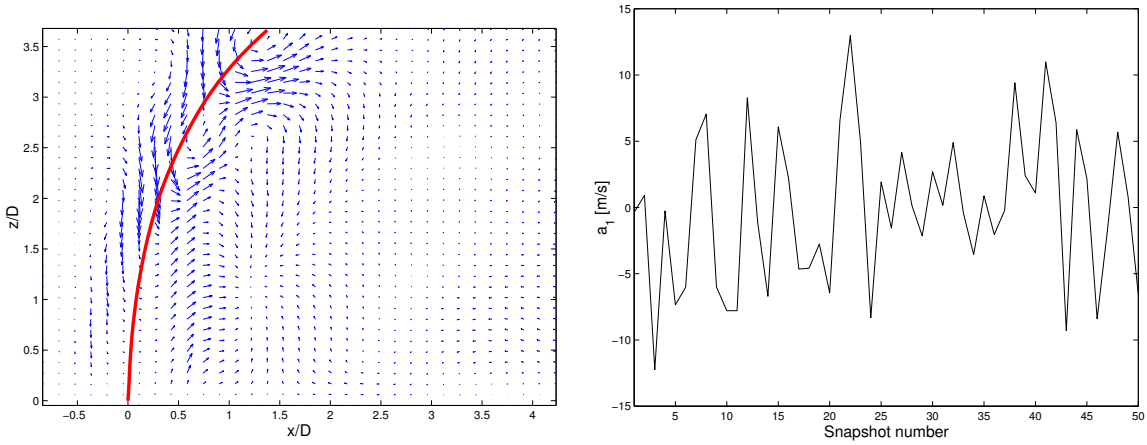

(a) (b)

Figure 8.6: (a) *2D POD mode 1 in $y = 0$ plane.* (b) *Variation of corresponding POD coefficient.*

Two large regions of vectors with uniform orientation are seen in the first 2D mode. Upstream of the jet trajectory the vectors point toward the jet region and downstream the vectors point away from the jet region. It is obvious to assume that this flow pattern is related to the incessant entrainment process that takes place in connection with any jet flow. This assumption is supported by the behavior of the first POD coefficient, a_1, which is displayed in figure 8.6(b). The plot shows that a_1 alternates between positive

and negative values throughout the data series. Sometimes fluid is entrained from the upstream region and sometimes fluid is entrained from the downstream region.

The plots in figures 8.7(a) and 8.7(b) show the second and third 2D POD mode in the $y = 0$ plane. Again the vectors have been scaled by a factor of 2 and the jet trajectory is indicated by the red line. Clearly, both modes are related to the

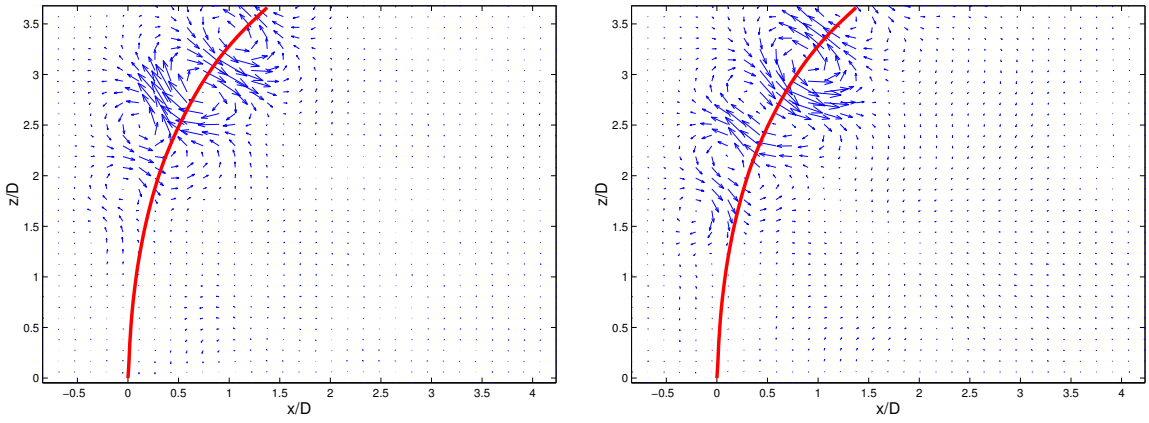

(a) (b)

Figure 8.7: (a) *2D POD mode 2 in* $y = 0$ *plane.* (b) *2D POD mode 3 in* $y = 0$ *plane.*

existence of the JSV. The structures revealed are almost identical, but are shifted along the jet trajectory. As explained by Cordier and Bergmann [23] this phenomenon is common for many POD applications. The flow in the jet region is of a convective nature and hence the turbulent structures appearing in this region are not tied to a fixed position. Therefore, two POD modes are found to represent the same type of structure at approximately the same level of energy (cf. section 3.4). This is also confirmed by the eigenvalue spectrum (figure 8.5), which shows that the decrease in energy from the second to the third mode is small compared to the changes from the first to the second mode and from the third to the fourth mode. An estimate of the spatial length scale of the flow related to the JSV may be obtained from the modes in figure 8.7. Interpreting the structures as a periodically varying vortex street, the length scale is given by the distance between the centers of vortices with the same orientation. Inspection of the two modes thus reveal that the spatial length scale is of the order of D both in the x– and in the z–direction.

The relation of the second and third 2D modes to the JSV is quite distinct. However, as noted in connection with the discussion of the eigenvalue spectrum several modes are necessary to fully describe the details of the 2D flow in the symmetry plane. The region around the jet trajectory is the part of the domain where most of the turbulence production takes place. Hence the most energetic modes are related to this area. In fact, the vast majority of the first about 25 2D modes are found to be dominated by flow structures situated in the neighborhood of the jet trajectory. From this point the modes are characterized by smaller flow structures, which are more or less equally distributed over the domain.

The above analysis was based on the in–plane velocities only. To see whether the fluctuations in the third direction are of importance a POD analysis was carried out

using all three velocity components, the results of which turned out as follows.

8.1.4 3D POD analysis

Figure 8.8 shows the eigenvalue spectrum for the 3D POD modes derived in the $y = 0$ plane. The result differs fundamentally from the one found in the 2D case. The energy

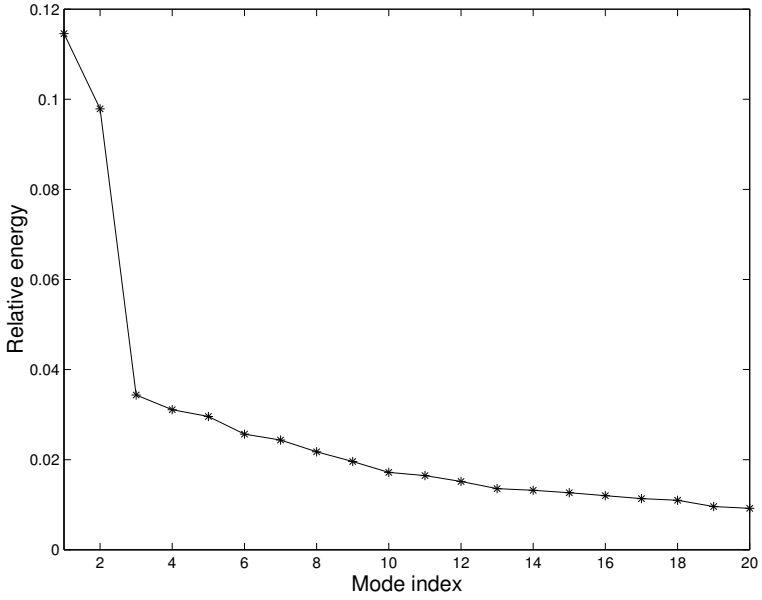

Figure 8.8: *Relative energy of 3D POD modes in $y = 0$ plane.*

content of the first two modes is about twice the values found before and a significant drop of energy from the second to the third mode can be observed. The explanation for this behavior is found by considering the plots of the most dominant 3D POD modes, which are shown in figure 8.9. The 3D POD modes are depicted by a contourplot of the out-of-plane component with the in-plane vector field plotted on top. The in-plane vectors have been scaled by a factor of 2, as in the 2D POD modes, to facilitate comparison of the two results. The jet trajectory is indicated with a black line.

The first two 3D modes are characterized by large regions with significant out-of-plane motion and practically no motion in the x–z plane. As the modes have been normalized in the POD analysis, information on the absolute values of the out-of-plane component e.g. in form of a colorbar is meaningless. However, a measure of the relative size of the out-of-plane motion may be obtained by comparing the spatial mean "velocities". Thus, the relative out-of-plane motion is defined as:

$$V_{\text{rel}} = \frac{\sum_i |\widetilde{v}_i|}{\sum_i \sqrt{\widetilde{u}_i^2 + \widetilde{w}_i^2}} \tag{8.2}$$

where i runs through all points in the domain and a tilde is used to indicate velocities in POD space. Correspondingly, the relative out-of-plane motion in the $x = \text{const.}$ and

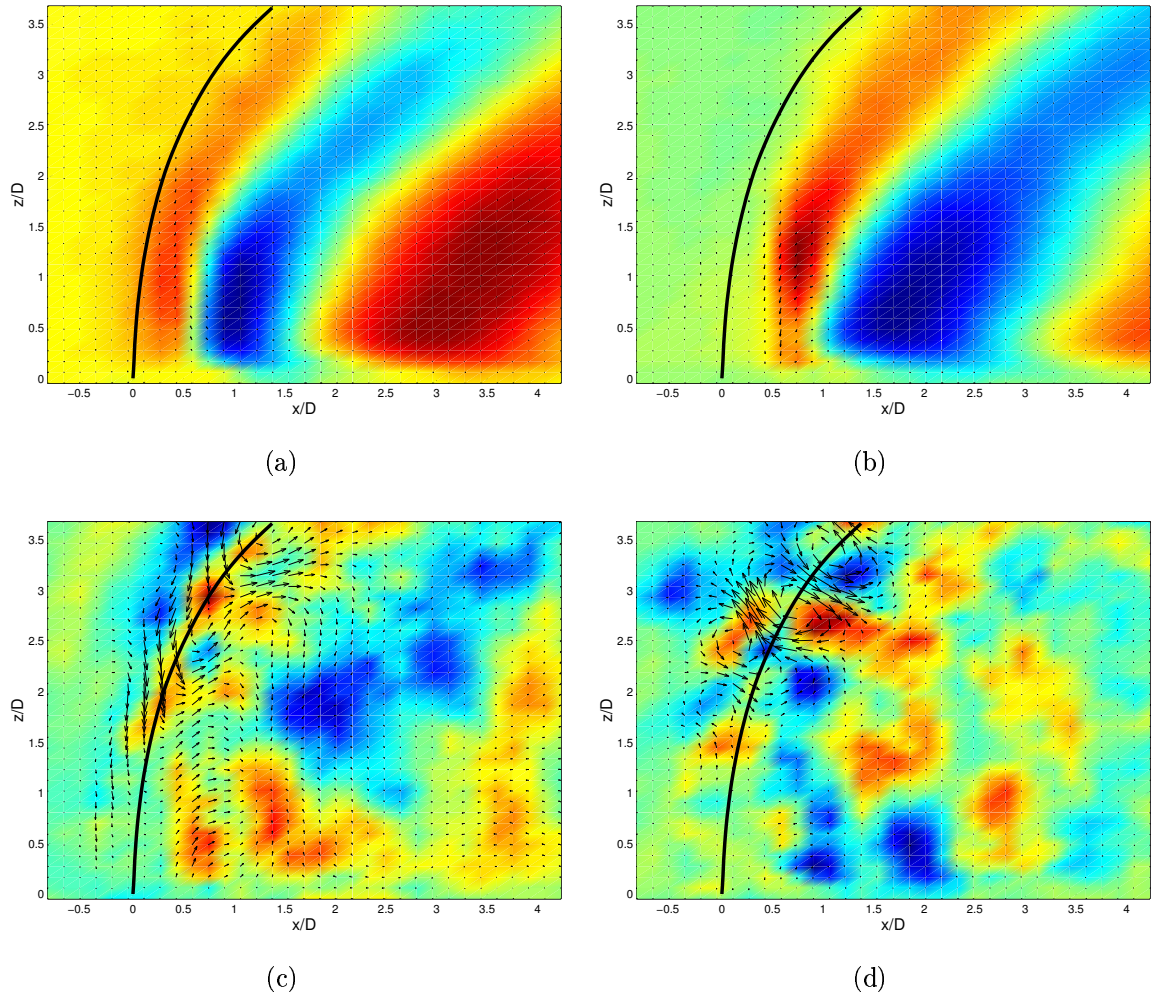

Figure 8.9: *Dominant 3D POD modes in $y = 0$ plane.* (a) *Mode 1.* (b) *Mode 2.* (c) *Mode 3.* (d) *Mode 4.*

$z =$ const. planes are defined as

$$U_{\text{rel}} = \frac{\sum_i |\widetilde{u}_i|}{\sum_i \sqrt{\widetilde{v}_i^2 + \widetilde{w}_i^2}} \tag{8.3}$$

and

$$W_{\text{rel}} = \frac{\sum_i |\widetilde{w}_i|}{\sum_i \sqrt{\widetilde{u}_i^2 + \widetilde{v}_i^2}} \tag{8.4}$$

respectively. Equations (8.3) and (8.4), will be applied in the following sections.

The values of V_{rel} for the four modes shown in figure 8.9 are summarized in table 8.1. The results show that using definition (8.2) the mean out-of-plane motion is almost

Mode number	1	2	3	4
V_{rel} [–]	7.7	6.8	0.2	0.2

Table 8.1: *Relative out-of-plane motion in 3D POD modes in the $y = 0$ plane.*

an order of magnitude larger than the in-plane motion for the first two 3D modes. Contrary to this, the out-of-plane motion in the third and fourth 3D mode is almost an order of magnitude smaller than the in-plane motion. This implies that in physical space the velocity fluctuations normal to the symmetry plane are more intense than the in plane fluctuations. An interesting result which would not have been revealed from an analysis of traditional PIV measurements with only two velocity components.

The interpretation of the flow patterns described by the first two 3D POD modes in the $y = 0$ plane is not straightforward. However, the following sections will show that the flow pattern revealed by the first POD modes in the $x =$ const. and $z =$ const. planes are in perfect agreement with the result found in figures 8.9(a) and 8.9(b). Hence, for further comments the reader is referred to these sections. For now, it should be mentioned that the POD coefficients, corresponding to the first two 3D modes, behave in the same way as the coefficient of the first 2D mode, alternating between positive and negative values (cf. figure 8.6(b)). Thus, the sign of the out-of-plane motion in the large connected regions of the first two modes is not fixed. Also it is interesting to notice that the first two modes indicate that the most energetic motions take place almost exclusively downstream of the jet trajectory. Following this observation, it seems reasonable to assume that the interaction between the jet and the crossflow induces turbulent fluctuations primarily in the downstream part of the domain.

The in-plane motion of the third and fourth 3D POD modes are seen to be identical to that of the first and second 2D POD modes. Also, the vector field of the fifth 3D POD mode (not shown) is the same as the one found in the third 2D POD mode. For increasing mode number the in-plane motion of 2D mode n and 3D mode $n + 2$ begin

to look less alike as the in-plane and out-of-plane motion become equally important. Interestingly, the flow structures revealed by the in-plane motion of the 3D modes are more or less equally distributed over the domain already from mode 15. In the 2D case the first 25 modes were almost exclusively connected to the jet region. This again underlines the importance of including all three velocity components to obtain a satisfying description of the dominant structures of the JICF as viewed in the $y = 0$ plane.

The following two sections present selected results from the analysis of the SPIV data obtained in the x = const. and z = const. planes. The emphasis will mostly be on the CVP and the important part it plays in the JICF.

8.2 Downstream evolution (x = const. planes)

The present section provides a description of the behavior of the JICF as viewed in the x = const. planes. First the development of the mean velocity field with increasing x is considered. The obtained results nicely supplement the information provided by the mean field in the symmetry plane to gain a full picture of the mean properties of the JICF. Second the results of 2D and 3D POD analyses are presented and the results discussed in relation to those obtained in section 8.1.

8.2.1 Mean flow development

Figures 8.10(a)–8.10(f) show the development of the mean flow with downstream position. The plots were created as contour plots of $U(y, z)$ with (V, W)–vectors plotted on top. Due to physical restrictions on the calibration for this configuration, data could not be obtained in the region closest to the wall. Hence the white area in the bottom part of the plots. The colorbars on the right show the magnitude of the out-of-plane velocity and a vector of length $3\frac{\mathrm{m}}{\mathrm{s}}$ has been added as reference for the in-plane velocities. To ease the comparison with the mean flow in the $y = 0$ plane, a circular symbol has been added at the position where the mean streamline jet trajectory penetrates the x = const. planes. Due to the limited extent in the z–direction of the domain considered for the $y = 0$ plane, this position is only available for $x < 33$ mm and hence is only seen in the first four plots.

Figure 8.10(a) shows the mean velocity field in the $x = 4$ mm plane ($x/D \approx 0.17$), very near the center of the jet. Hence, large vertical velocities are found in the region with $-0.5 < y/D < 0.5$ and $z/D \lesssim 2$. As a consequence the U–velocity in the region right after the jet exit is close to zero (see also figure 8.1). Further, the U–contours just left and right of the center at $0.5 < |y|/D < 1$ and $z/D \lesssim 1$ show that the crossflow velocity in this region is larger than the mean freestream crossflow velocity. The enhanced U–velocity in this region is a result of an acceleration of the crossflow as it moves around the "obstacle" created by the mean jet.

On close inspection the initialization of the CVP can be observed in connection with the U–velocity maxima in figure 8.10(a). In the second plot corresponding to $x = 10$ mm the presence of the CVP is more clearly evidenced with two distinct vortex centers at $|y|/D \approx 0.8$ and $z/D \approx 1$. The vectors closest to the wall in figure 8.10(b) are a bit shorter than the ones in the $x/D \approx 0.17$ plane. This agrees with the fact that

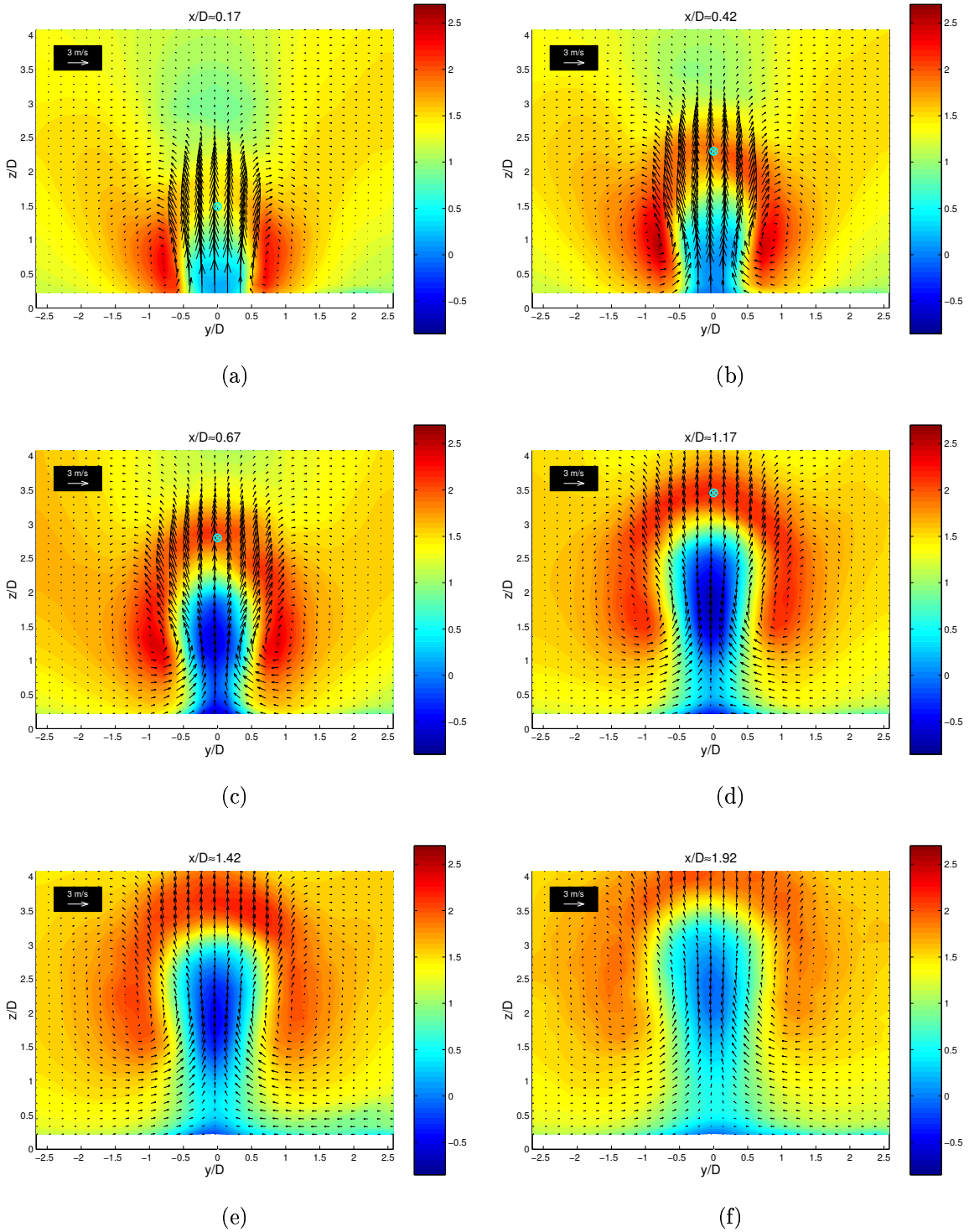

Figure 8.10: *Evolution of mean flow field with downstream position.* (a) $x = 4$ *mm.* (b) $x = 10$ *mm.* (c) $x = 16$ *mm.* (d) $x = 28$ *mm.* (e) $x = 34$ *mm.* (f) $x = 46$ *mm.*

the $x = 10$ mm plane is closer to the periphery of the jet orifice than the one in figure 8.10(a).

At $x/D \approx 0.67$ the deflection of the jet has become so pronounced that the crossflow velocity at the position of the jet trajectory has reached the level of the accelerated flow in the regions to the left and to the right of the jet region. Figure 8.10(c) also shows that the U–velocity in the region enclosed by the maximum U–contours has become negative at $x/D \approx 0.67$. The velocity field is now situated at an x–position within the so-called reversed flow region. The reversed flow region clearly depicted by figure 8.1 extends from $x/D \approx 0.6$ to $x/D \approx 1.8$. Local minima of U are found near the wall ($x/D \approx 0.2$) and at $(x/D, z/D) \approx (1, 1.5)$. This observation was also reported by Meyer et al. [55]. The negative values of U in the upper part of the reversed flow region indicate that the z–components of the vorticity connected to the CVP start to become important (cf. section 8.3).

A similar pattern is found in figures 8.10(d) and 8.10(e), which show that a region with negative U–velocity enclosed by contours corresponding to a crossflow faster than the freestream velocity also characterizes the y–z planes at $x/D \approx 1.17$ and $x/D \approx 1.42$. It is worth noting that the location of the circular symbol indicating the path of the jet trajectory in figure 8.10(d) is coincident with the location of the maximum U–velocity. As already mentioned this is a feature related specifically to a jet-to-crossflow ratio of $R = 3.3$, and the result validates the findings presented in [62].

In the final plot, which shows the mean velocity field at $x/D \approx 1.92$, the velocities in the x–direction have all returned to values greater than or equal to zero. Hence, at this position almost two jet diameters downstream of the jet center, the CVP is now exclusively connected to vorticity components aligned in the x–direction. Further, the jet trajectory has risen to a z–location so far from the wall that the U–velocities in the lower part of the domain start to increase towards the mean freestream crossflow velocity. Once again comparing with figure 8.1, the results are seen to be in perfect agreement with the mean velocity field found in the symmetry plane.

With this an almost complete description of the mean characteristics of the JICF has been achieved. For completeness a couple of mean velocity fields from the $z = \text{const.}$ planes will be displayed in section 8.3. In order to obtain an overview of the dominant turbulent structures of the JICF as viewed in the $x = \text{const.}$ planes, the results of a POD analysis are now presented.

8.2.2 POD analysis

The flow mapping presented above was based on dataseries each of about 200 instantaneous flow realizations. To make sure that the number of snapshots was high enough to obtain statistical convergence, the POD analysis has only been carried out in the $x = 24$ mm plane for which a total of 1000 independent realizations were available. The results of the analyses, including two and three velocity components, will be referred to a 2D and 3D POD modes and coefficients, respectively.

Figure 8.11 displays the eigenvalue spectra of the POD analyses in the $x = 24$ mm plane, i.e. at $x/D = 1$ including two and three velocity components, respectively. The relative energy content of the individual modes in the 3D case is seen to be a little bit lower than in the 2D case. However, the two spectra exhibit the same behavior showing

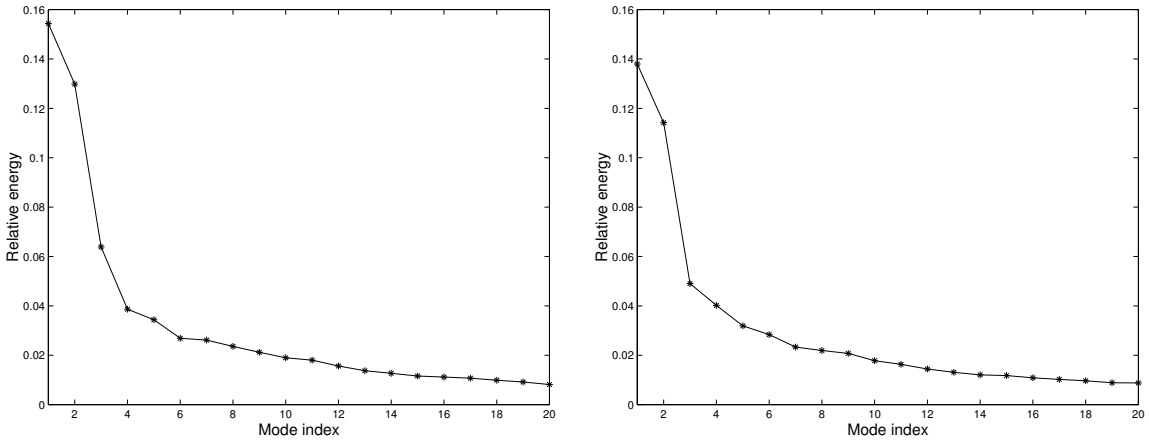

(a) (b)

Figure 8.11: *Relative energy of POD modes in the $x/D = 1$ plane.* (a) *2D analysis.* (b) *3D analysis.*

the existence of two dominant modes, which together contain of the order of 25% of the total turbulent energy, followed by a significant number of modes for which the energy decays slowly with mode number. The similarity of the two graphs indicates that the in-plane flow pattern revealed by the first couple of modes does not change, when all three velocity components are included, compared to the 2D case. Still, as the first two modes represent only about 25% of the total energy, the plots also imply that many modes are needed to capture all details of a given flow realization. In fact, the shape of the two spectra is quite similar to the one obtained from the 3D POD analysis in the $y = 0$ plane (figure 8.8).

Figures 8.12(a)–8.12(d) show the first two POD modes obtained from the 2D and 3D analysis, respectively. The out-of-plane motion, $\widetilde{u}(y, z)$, is depicted via contourplots and the red circular symbol at $z/D \approx 3.3$ indicates the position where the jet trajectory penetrates the $x = 24$ mm plane. To enhance the details of the in-plane flow pattern, the vectors have been scaled by a factor of 3 in all four plots.

As speculated on basis of the eigenvalue spectra, the in-plane motion is identical for the first two modes in the 2D and the 3D case. In addition to the in-plane motion, two connected regions with significant out-of-plane motion are found around $|y|/D \approx 0.5$. The vertical position of the region centers are $z/D \approx 2$ and $z/D \approx 1$ in the first and second mode, respectively. This out-of-plane motion is related to the shape of the dominant modes found in the z = const. planes, which will be described in detail in section 8.3. Hence, in the following, the main focus will be on a comparison of the present results with the POD modes found in the previous section.

Considering the motion along a straight line given by $y = 0$, mode 1 is seen to be dominated by a region with movement in the positive y–direction, which covers the region $0.3 \leq z/D < 2$. The value of $\widetilde{v}$ then drops to zero and changes sign to become negative but with a smaller absolute value for $2.2 < z/D < 3$. Both $\widetilde{u}$ and $\widetilde{w}$ are virtually identical zero in the same interval. The exact same behavior is observed in figure 8.9(a) along $x/D = 1$, except in this mode the sign of $\widetilde{v}$ changes from negative

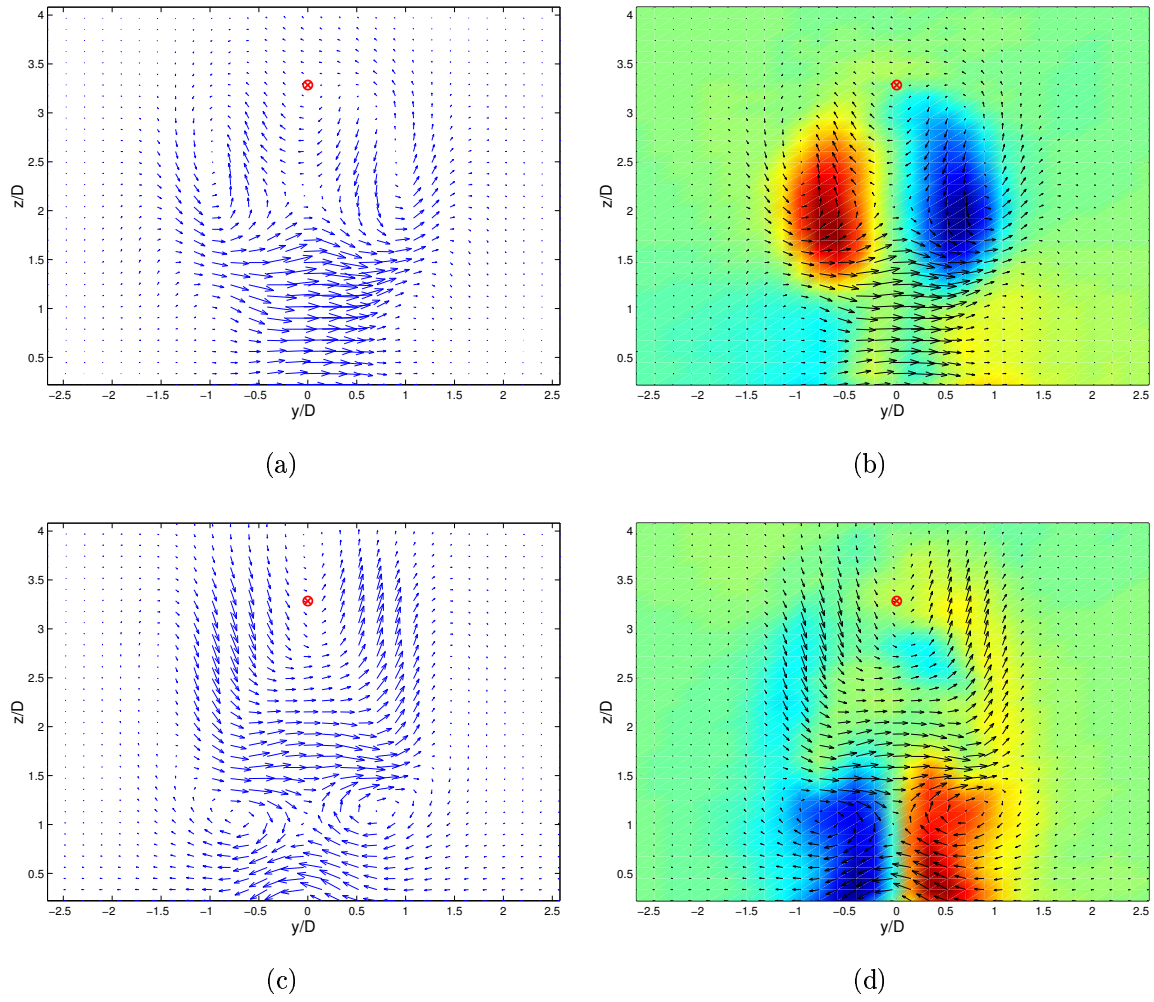

Figure 8.12: *Dominant modes in $x/D = 1$ plane.* (a) *2D POD mode 1.* (b) *3D POD mode 1.* (c) *2D POD mode 2.* (d) *3D POD mode 2.*

to positive. However, as mentioned in connection with the discussion of the first two modes in the $y = 0$ plane, the sign of the motion in the y–direction, downstream of the jet, is not fixed. This is also reflected in the POD coefficients corresponding to the first 2D and 3D mode in the $x/D = 1$ plane, which are shown in figures 8.13(a) and 8.13(b), respectively: the coefficients alternate between positive and negative values throughout

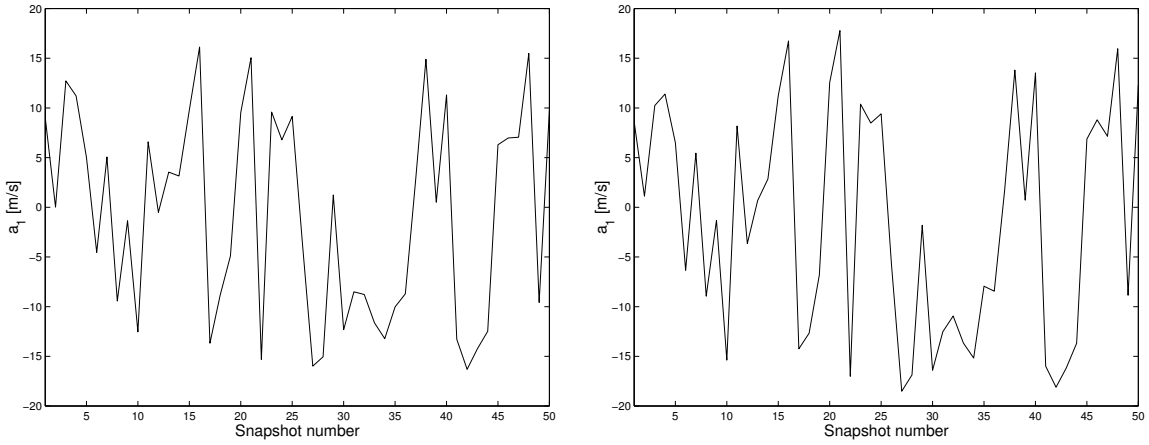

(a) (b)

Figure 8.13: *POD coefficients corresponding to first POD mode in the $x/D = 1$ plane.* (a) *2D analysis.* (b) *3D analysis.*

the dataseries shown. Thus, recalling that the velocities in POD space should always be interpreted in the context of the sign of the associated POD coefficients, the first 3D modes found in the $y = 0$ and $x = 24$ mm planes are in perfect agreement. One should note, though, that a comparison of the POD coefficient of 3D mode 1 in the $y = 0$ plane with the coefficients shown in figure 8.13 would not make sense as the latter are related to the complete y–z domain at $x/D = 1$ and not just $y = 0$.

The eigenvalue spectra were found to be quite similar for the 2D and 3D POD analysis. Close inspection of figures 8.13(a) and 8.13(b) reveals that the coefficient corresponding to the first POD mode is practically identical in the two cases. These observations suggest that the in-plane fluctuations are more intense than the out-of-plane fluctuations in the $x/D = 1$ plane. To elaborate on this, the relative out-of-plane motion, U_{rel} (equation (8.3)), has been calculated for some of the first 3D POD modes. The result is shown in table 8.2. Although the dominance of the in-plane motion in

Mode number	1	2	3	4	5	6
U_{rel} [–]	0.5	0.4	0.5	1.1	0.9	0.3

Table 8.2: *Relative out-of-plane motion in 3D POD modes in the $x/D = 1$ plane.*

the $x/D = 1$ plane is not as pronounced as the dominance of the out-of-plane motion in the $y = 0$ plane (see table 8.1), the first three modes are seen to be characterized by a larger mean in-plane than out-of-plane motion. In the fourth and fifth 3D mode the

out-of-plane motion starts to play a significant role. Remarkably, in the sixth 3D mode the in-plane motion again seems to be dominant. This behavior is reflected in the flow patterns of the corresponding 2D and 3D POD modes of which the third and fourth are shown in figure 8.14. The third 2D and 3D modes show the same in-plane flow pattern

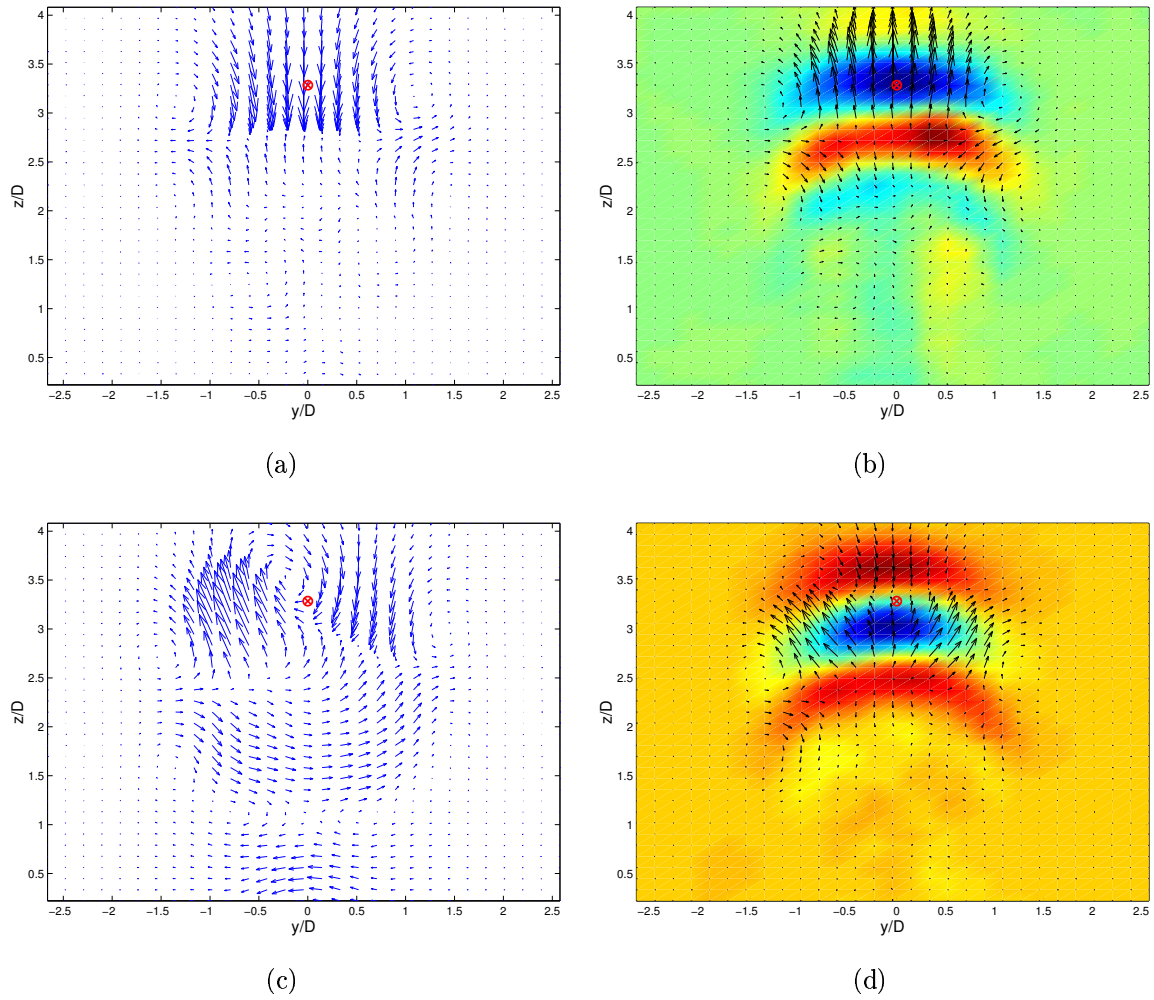

Figure 8.14: *Dominant modes in the $x/D = 1$ plane.* (a) *2D POD mode 3.* (b) *3D POD mode 3.* (c) *2D POD mode 4.* (d) *3D POD mode 4.*

except for a sign reversal. That the two results are indeed equivalent is confirmed by the plots in figure 8.15, which show their respective POD coefficients for a series of 50 snapshots. Apart from minor discrepancies the development of the two coefficients is identical except for a sign reversal. The in-plane motion of the fourth 3D mode is very different from that of the 2D mode. According to table 8.2 the out-of-plane motion in this mode dominates the in-plane motion. Three successive regions with significant out-of-plane motion of alternating sign are found in a region centered at $y \approx 0$, which extends from $z/D \approx 2$ to $z/D \approx 4$ passing the jet trajectory. Comparing with figure 8.9(d) it becomes clear that this flow pattern is related to the existence of the JSV. The dominant out-of-plane fluctuations are produced by vortices with axes of rotation aligned in the y–direction. A flow pattern similar to the one in 3D POD mode 4 is

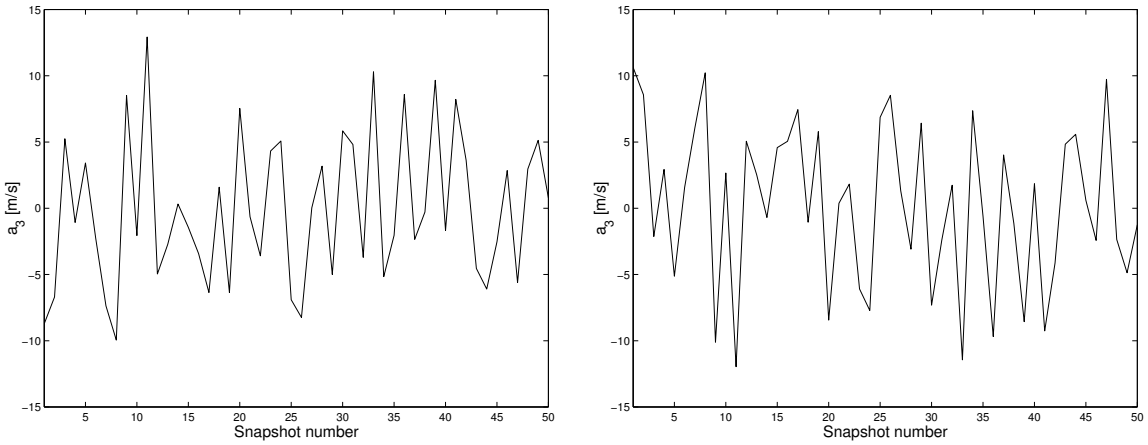

(a) (b)

Figure 8.15: *POD coefficients corresponding to third POD mode in the $x/D = 1$ plane.* (a) *2D analysis.* (b) *3D analysis.*

found in 3D POD mode 5 (not shown), which is also dominated by out-of-plane motion. Interestingly, the in-plane motion of the fourth 2D mode is recovered by the sixth 3D mode (not shown). This is in agreement with the results of table 8.2, which show that the value of U_{rel} for the sixth 3D mode has dropped to a level indicating that the in-plane motion is again dominant.

The topology of the mean flow and the 3D POD modes in the x = const. planes was found to agree well with the results presented for the symmetry plane. To make the examination of the JICF complete, the analysis of the data obtained with the third and final SPIV configuration, i.e. in the z = const. planes is now presented.

8.3 Increasing wall distance (z = const. planes)

The x–y plane data considered was recorded at locations corresponding to $z = 16$ mm, $z = 32$ mm, and $z = 48$ mm, respectively. The domain covered in the second of these planes was centered approximately at $y = 0$ (with $|y|/D \lesssim 1.5$) and extended from $x/D \approx -0.7$ to a downstream position of $x/D \approx 4$. To improve the spatial resolution the data field in the two other planes was limited to the region corresponding to positive y–values ($y/D \gtrsim -0.25$) and which extended from $x/D \approx -0.8$ to $x/D \approx 1.8$. In the following the mean flow pattern as viewed in these three planes is described and POD analyses are carried out to complete the investigation of the dominant flow structures of the JICF.

8.3.1 Mean flow development

Figure 8.16 shows the evolution of the mean flow in the x–y plane with increasing z. The plots were created as contours of $W(x, y)$ with (U, V)–vectors plotted on top, and a vector of length equal to the freestream crossflow velocity has been included in the top right corners for reference.

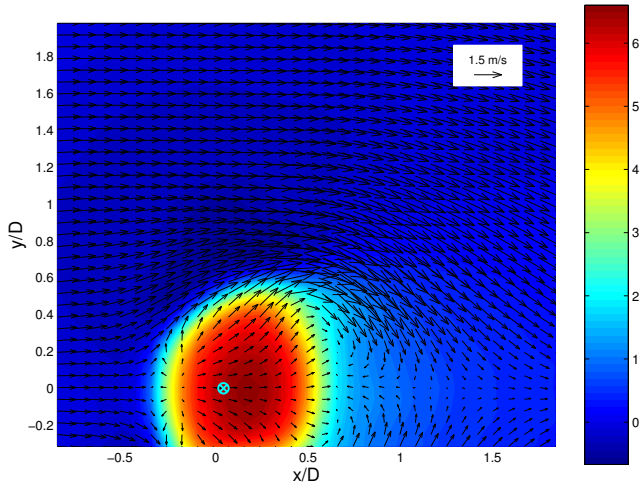

(a)

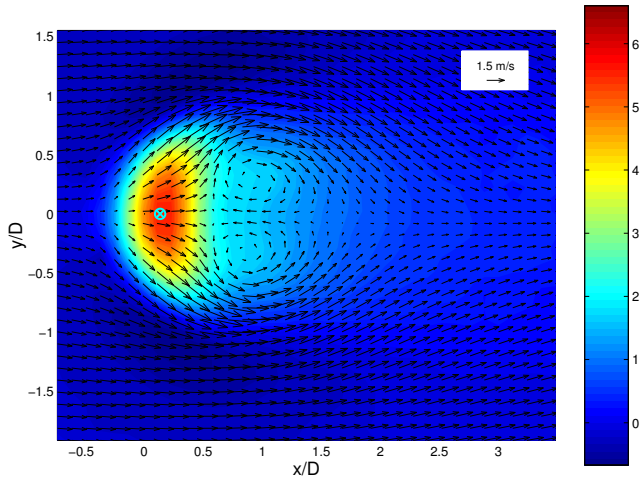

(b)

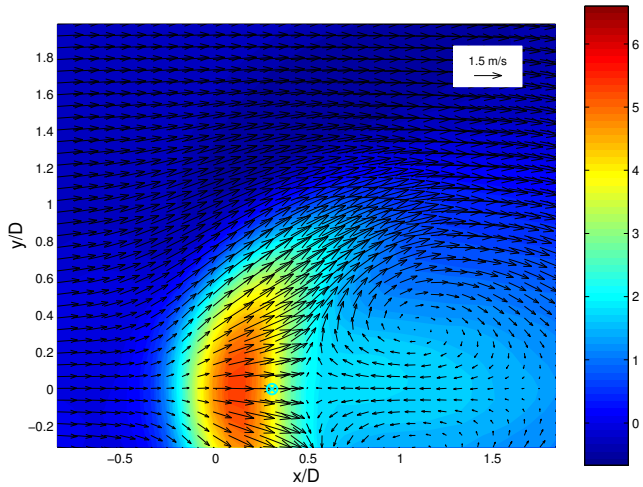

(c)

Figure 8.16: *Mean velocity field viewed in x–y planes.* (a) $z = 16$ *mm* $(z/D \approx 0.67)$. (b) $z = 32$ *mm* $(z/D \approx 1.33)$. (b) $z = 48$ *mm* $(z/D = 2)$.

For all three positions negative values of W are found above (and below) the jet core in regions starting at $x \approx 0$ and extending downstream in a direction parallel to the in-plane velocity vectors which are deflected by the jet. These negative regions are responsible for the x–component of vorticity related to the CVP and are in agreement with the mean velocity fields in the x = const. planes shown in figure 8.10. The region with maximum W–velocity is deformed from an almost circular shape close to the wall to a half–moon shape two jet diameters from the wall. In the same region, U increases from small positive values at $z = 16$ mm to the order of the freestream velocity at $z = 48$ mm. Accordingly, the location where the jet trajectory penetrates the z = const. plane (indicated by a circular symbol) moves downstream.

Most of these changes are related to the formation of the counter–rotating vortex pair. The CVP is clearly depicted by the mean fields at $z = 32$ mm and $z = 48$ mm, with vortex centers at $(x/D, y/D) \approx (0.9, \pm 0.25)$ and $(x/D, y/D) \approx (1.1, \pm 0.3)$, respectively. As already discussed the CVP has vorticity components in both the x– and the z–direction. The x–component is initiated very close to the jet exit and stays at a significant level several jet diameters downstream. The z–component of vorticity only starts to become important about half a jet diameter downstream and about one diameter from the wall (deduced from figures 8.10(b)–8.10(c)). From this position the axes of rotation of the CVP are more or less aligned with the jet trajectory. The further the downstream position the more parallel to the x–axis the CVP becomes. In this way the CVP accounts for most of the entrainment occurring downstream from (and eventually below) the jet trajectory. Specifically, in the region covering $0.5 < x/D \lesssim 1.5$ and $0.5 < z/D \lesssim 2.5$ the CVP is transporting fluid with low W–velocity towards the jet core and thus contributes to the exchange of W–momentum (cf. figure 8.1).

So far there seems to be no definitive consensus on how the CVP is initiated. Fric and Roshko [30] simply state that it occurs as a result of the impulse of the jet on the crossflow. A more detailed explanation was provided by Lim et al. [47] whose visualizations of a laminar JICF showed that the CVP results from folding of the cylindrical shear–layer from the jet exit. A related explanation was given by Yuan et al. [98], who reported the existence of so-called "hanging" vortices forming on the lateral sides of the turbulent jet as it encounters the crossflow. They theorized that these vortices break down to initiate the CVP just downstream of the jet as a result of the adverse pressure gradient in this region. The present analysis does not reveal how the CVP is initiated. However, the evolution of the CVP in its mean sense is clearly depicted by the velocity fields shown in figures 8.10 and 8.16. The relevance of the CVP in the entrainment process has already been pointed out. In the following the results of a POD analysis will show, among other things, how the CVP is also of significant importance to the production of turbulent kinetic energy.

8.3.2 POD analysis

The in-plane motion was found to be identical for most of the first 2D and 3D modes in the z = const. planes. Hence, in the following, only the results of the 3D analysis will be considered. Table 8.3 shows the relative mean out-of-plane motion, W_{rel}, for the dominant modes in the three planes, as defined by equation (8.4). The values of W_{rel} also indicate a dominance of in-plane motion in the z = const. planes. A slight increase

Mode number	1	2	3	4
W_{rel} [–], $z = 16$ mm	0.3	0.2	0.4	0.5
W_{rel} [–], $z = 32$ mm	0.3	0.2	0.3	0.4
W_{rel} [–], $z = 48$ mm	0.3	0.6	0.5	0.8

Table 8.3: *Relative out-of-plane motion in 3D POD modes in the z = const. planes.*

in the influence of the out-of-plane motion is observed for the second POD mode at $z = 48$ mm compared to the other two positions. This difference will be explained later in connection with the interpretation of the individual modes.

Figure 8.17 shows the eigenvalue spectra for the 3D modes in the $z = 16$ mm and $z = 48$ mm planes. The shape of the spectrum obtained at $z = 32$ mm is similar to the one

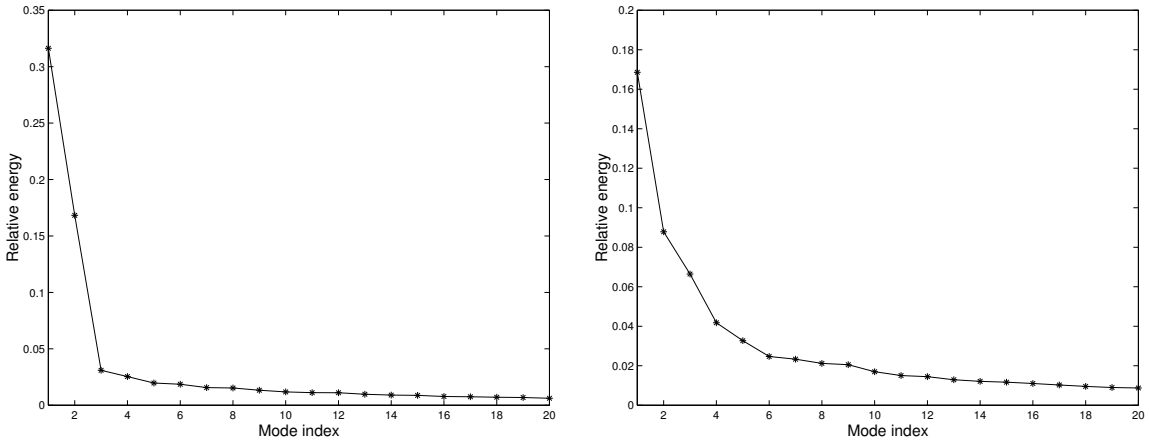

(a) (b)

Figure 8.17: *Eigenvalue spectra for 3D POD modes in the z = const. planes.* (a) *$z = 16$ mm.* (b) *$z = 48$ mm.*

in figure 8.17(a) with two distinct highly energetic modes followed by many modes at a comparable level of energy. In contrast, the energy distribution at $z = 48$ mm decreases smoothly with mode number. Further, the plots show that the energy contained in the first POD mode drops with increasing wall distance. (Mode 1 at $z = 32$ mm accounts for 19%). This is in agreement with the general observation that the coherent structures of the near jet represent a larger amount of energy than those of the far jet (see e.g. [22]). Another interesting result is that the two first modes at $z = 16$ mm alone capture more than 48% of the total energy. Comparing with the results of the POD analyses in the y = const. and x = const. planes, it may be concluded that the most energetic components of the CS characterizing the JICF, at least in the domains considered, are found in x–y planes perpendicular to the z–direction.

The first two POD modes found in the three z = const. planes are shown in figure 8.18. As before the plots were created as contourplots of the out-of-plane motion with the in-plane motion vectors on top and the location of the jet trajectory indicated by a circular symbol.

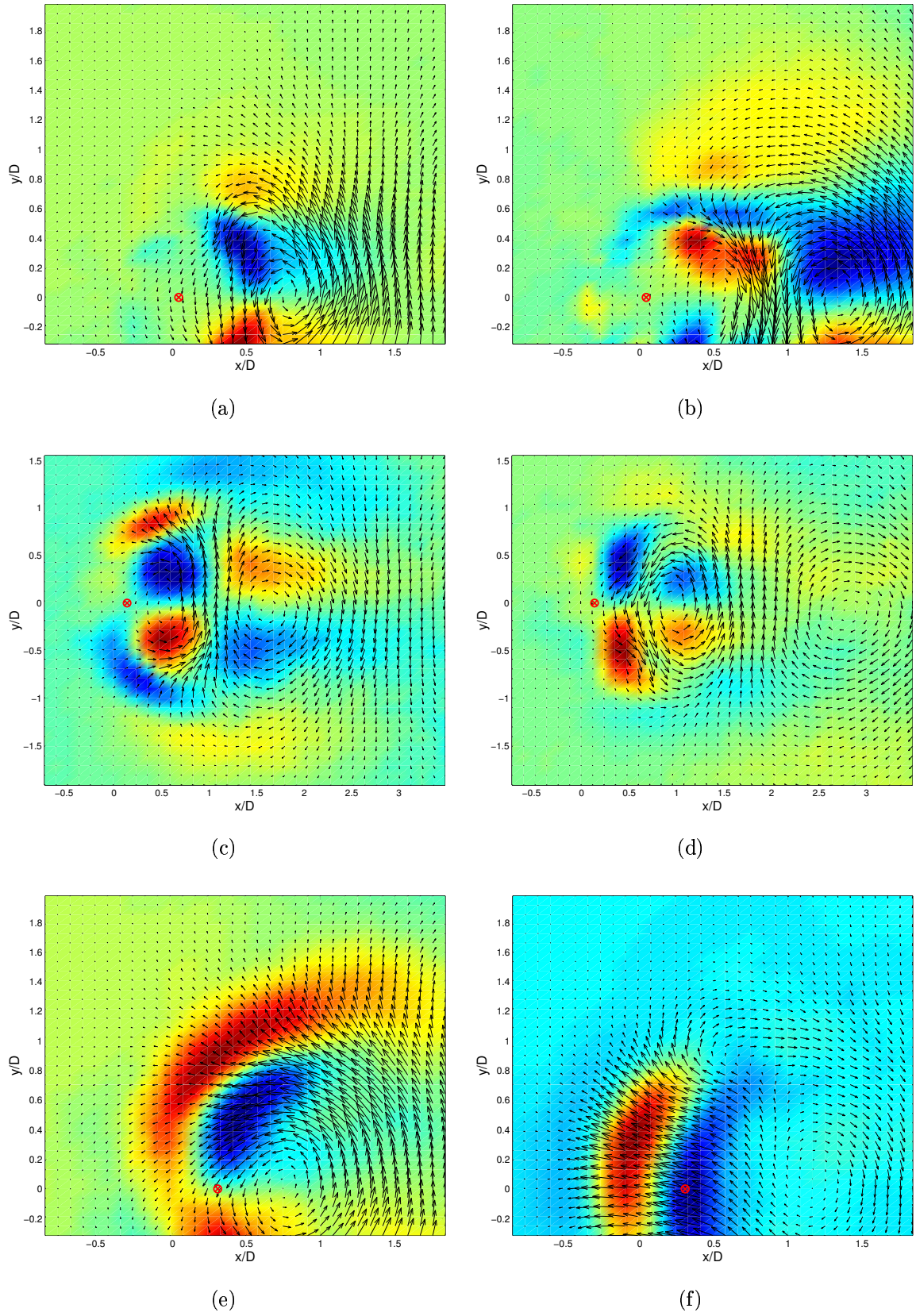

Figure 8.18: *3D POD modes in z = const. planes.* (a) *Mode 1 at z = 16 mm.* (b) *Mode 2 at z = 16 mm.* (c) *Mode 1 at z = 32 mm.* (d) *Mode 2 at z = 32 mm.* (e) *Mode 1 at z = 48 mm.* (f) *Mode 2 at z = 48 mm.*

The first interesting observation is that the most energetic mode in the $z = 16$ mm plane (figure 8.18(a)) is qualitatively similar to the second most energetic mode in the $z = 32$ mm plane (figure 8.18(d)) and vice versa. Thus, the mode representing the most energetic structure closer to the wall has become less important further from the wall, while the mode representing the second most energetic structure closer to the wall is found to represent the most energetic structure further from the wall. As the POD searches for the most energetic structures the first modes indicate where the turbulence production is maximum. This fact was pointed out by Delville et. al [25]. Therefore the result can be interpreted as follows. The dominant structures in the two planes are similar in shape, but the location of maximum production of turbulent kinetic energy has changed. The change is related to the evolution of the CVP with increasing z. At $z = 16$ mm the deformation of the incoming jet is still limited. Here, the most energetic fluctuations are found just after the jet core, in connection with the region around the singular point (stable node) seen in figure 8.16(a). Further from the wall, at $z = 32$ mm, mode 1, now showing two in-plane vortices, is centered at $x/D \approx 1$. The fully developed CVP, depicted by figure 8.16(c), is also found to be centered at this downstream position. Hence, the current results indicate that the maximum production of turbulent kinetic energy occurs in connection with the CVP.

A general observation for the planes closest to the wall is that most of the modes are located in the region downstream of the jet trajectory. In fact there seems to be a connection between z–location and preferred mode organization. At $z = 16$ mm, motion upstream of the jet trajectory is not detected until the seventh POD mode (not shown). In the $z = 32$ mm plane motion upstream of the jet trajectory is seen already in the fourth mode (not shown). In accordance with this tendency upstream motion is seen to be of importance already in the second mode at $z = 48$ mm (figure 8.18(f)). Actually, a little motion upstream of the trajectory can be detected already in the first mode at $z = 48$ mm. The reason for this is that close to the wall the high values of w cause the jet to act almost as a solid body. The crossflow fluid is simply diverted around the jet[2]. Hence, in this region, turbulent interactions are confined to the downstream part of the domain. Further from the wall the vertical velocities have decreased to the level of the crossflow velocity and vigorous mixing of jet and crossflow fluid takes place already upstream of the jet trajectory. Not only the in-plane motion upstream of the jet is of significance in mode 2 at $z = 48$ mm. While confined to a small region, also the relative out-of-plane motion has increased compared to the other planes (cf. table 8.3). Comparing the flow pattern in figure 8.18(d) with the fourth and fifth 3D mode in the $y = 0$ plane of which the first is shown in figure 8.9(d) it seems reasonable to assume that this mode is related to the dynamics of the JSV. These observations are reflected in the eigenvalue spectrum of the POD modes at $z = 48$ mm (figure 8.17(b)). Although the energy content of the first mode is still significantly larger than for the rest, the smooth decrease of energy with mode number indicates that several different flow structures start to become important in the x–y planes for $z > 48$ mm.

[2]An exception is the fluid which rolls up into the horseshoe vortices. However, these are formed very close to the wall and hence have no influence on the flow at $z = 16$ mm.

8.4 Implications of results of POD analyses

The present section serves to sum up the results of the POD analyses carried out in the three mutually orthogonal planes of the JICF and to discuss the implications hereof.

First of all, the importance of including all three velocity components to obtain a satisfactory picture of the dominant structures of this complex type of flow has been demonstrated. More specifically, the following main observations were made:

- The most energetic POD modes of the JICF are related to velocity fluctuations normal to the symmetry plane in a region downstream of the jet trajectory
- After the first couple of modes, the level of energy decays slowly with mode number
- The first modes change character with increasing wall distance

As already discussed, the two most energetic modes are found in connection with the CVP, which develops along and just downstream of the jet trajectory. There are several possible explanations for this. Although the CVP has mean flow definition, it also has unsteady components. These unsteady components, which may arise e.g. as a result of the interaction with accelerated crossflow fluid, may themselves be responsible for velocity fluctuations of significant intensity. Another possible explanation is that the most energetic modes are related to the wake vortices. These are indeed observed downstream of the jet, but judging from the experimental evidence presented by Fric and Roshko [30], these vortices do not become important until several jet diameters downstream, i.e. further downstream than the region in which the most dominant POD modes are found. However, the initiation of the wake vortices starts directly downstream of the jet. Hence, it may be speculated that this initiation is connected to the presence of the CVP. Although the wake vortices are not "shed" from the jet, they still occur with alternating sign. This also explains the flapping motion indicated by the coefficients of the dominant POD modes. Based on these observations it is conjectured that the maximum production of turbulent kinetic energy in the JICF takes place as a result of the initiation of the wake vortices and that the dynamics of the CVP play a significant role in the process.

The second observation listed above implies that many structures representing lower levels of energy are also important to the near field of the JICF. Most of these are related to motion in the vicinity of the jet trajectory. Some may be due to the entrainment of crossflow fluid, but for the main part the exchange of energy in this region is related to the dynamics of the jet shear–layer vortices. The JSV are fixed neither in space nor in shape, which makes it impossible for the POD to educe one dominant structure representing this phenomenon. Hence, although the results have shown that in the $z =$ const. planes the first two POD modes alone may capture up to 50% of the total energy, the presence of the JSV necessitates the inclusion of a large number of POD modes to fully describe the dynamics of the JICF.

The final main observation is related to both of the above. As the distance to the wall increases the jet becomes less dominant and interaction between jet and crossflow fluid starts to take place also on the upstream side of the jet trajectory. Also, the JSV start to become more important a certain distance from the wall (see figure 8.4). At

the same time, the strength of the CVP whose maximum is found in the region around $(x/D, z/D) \approx (1, 1.5)$ starts to decrease. Interestingly, the results in [30] show that also the intensity of the wake vortices is less pronounced the further the distance from the wall. These observations all support the theory that the maximum production of turbulent kinetic energy in the near field of the JICF is related to the initiation of the wake vortices and that the CVP plays an important role in the process.

The speculations above reflect the current state of the investigations carried out for the jet-in-crossflow by the present author. To further explore these ideas the next step would be to compare the POD modes with instantaneous flow realizations to obtain a deeper understanding of the importance of the individual modes in the actual flow. Also, acquisition of temporally resolved data would make a study of how the influence of the different POD modes varies in time possible. Both of these are obvious topics for a continued study of the dynamics of the JICF.

8.5 Summary

This chapter has presented the results of an elaborate analysis of velocity data from the JICF. The data was acquired in three mutually orthogonal planes using stereoscopic PIV. Accordingly, the results were presented in three separate sections. A fourth section was finally included to discuss the implications of the outcome of the POD analyses.

The first section focused on the symmetry plane i.e. the x–z plane at $y = 0$. The mean flow in this plane was presented and it was explained how the mean streamline trajectory can be obtained to describe the trajectory of the jet. Further, the mean vorticity field in the $y = 0$ plane was discussed and a demonstration of the existence of the jet shear–layer vortices given. It was found that the mean vorticity field is in excellent agreement with result from LDA measurements from the same test facility. Finally, POD analyses were carried out including two and three velocity components, respectively. A measure of the relative out-of-plane motion in the 3D POD modes was introduced, which showed that flow structures related to fluctuations perpendicular to the x–z plane are dominant in the near field of the JICF.

In the second section, the data obtained in y–z planes at different x–positions was considered. A thorough description of the downstream evolution of the mean 3D velocity field was gained through plots of the mean flow at $x = 4, 10, 16, 28, 34,$ and 46 mm, respectively. POD analyses including two and three velocity components in the $x = 24$ mm plane revealed that the in-plane motion is dominant, but that significant out-of-plane motion is represented already from the fourth 3D POD mode. The flow pattern of the first 3D mode viewed along the line $y = 0$ was found to be in perfect agreement with the flow pattern of the first mode in the symmetry plane.

In the third section, data in the x–y planes corresponding to $z = 16$, 32, and 48 mm, respectively, was investigated. Plots of the mean 3D velocity fields, as viewed in these planes, clearly depicted the important counter–rotating vortex pair, whose centers are found at $(x/D, y/D) \approx (0.9, \pm 0.25)$ and $(x/D, y/D) \approx (1.1, \pm 0.3)$ at $z = 32$ mm and $z = 48$ mm, respectively. POD analyses showed that the in-plane motion in the $z =$ const. planes dominates close to the wall, where the most energetic structures are found downstream of the jet trajectory. Further from the wall at $z = 48$ mm where the

jet is less dominant, the first modes were found to represent structure also upstream of the jet trajectory.

Finally, the main results of the POD analyses were recapitulated and their implications discussed. The main conclusion was that the maximum production of turbulent kinetic energy in the JICF is associated with the initiation of the wake vortices, which is related to the dynamics of the counter–rotating vortex pair.

The next and final part of the present thesis reports the results of analysis of data obtained by simultaneous PIV and LIF measurements in a free axisymmetric turbulent jet.

Part D

Free turbulent jet

Chapter 9

Free Turbulent Axisymmetric Jet

As the title suggests, the present chapter deals with the free turbulent axisymmetric jet. For convenience, one or more of the adjectives will be left out from time to time in the following. Most of the results presented were obtained during a three month stay at the Laboratory for Aero and Hydrodynamics, Delft University of Technology, The Netherlands, working with prof. dr. ir. J. Westerweel. The investigations have been based on an existing dataset of combined PIV and LIF images recorded by C. Fukushima[†] and were initiated by the ideas of prof. dr. J.C.R. Hunt[‡].

In the first section a short description of the background and motivation of the current investigations including references to related work will be provided. Second the concept of self similarity, a feature possessed by the axisymmetric jet, is explained. Third a description of the data processing with a short explanation of the concepts of laser induced fluorescence (LIF) is given and finally, selected analysis results showing conventional as well as *conditional* statistics of the free turbulent jet are presented. The ideas behind the derivation of conditional statistics comprise the core of the investigations and will be explained throughout the chapter.

9.1 Background and motivation

As mentioned in the introductory chapter of this thesis, the free turbulent jet is of importance to mixing processes. This was the original incitement for Fukushima et al. [31] to carry out the experiments yielding the simultaneous PIV and LIF data for the free jet. With the former providing the instantaneous velocity field and the latter providing the instantaneous concentration field, they were able to calculate the very important velocity–concentration correlations (Reynolds fluxes), which represent the contribution of turbulent motion to the mean concentration flux. Further exploration of the data obtained by Fukushima et al. was made by Westerweel et al. [92], who used the data to derive conditional turbulence statistics for the free jet. Using the LIF images to detect the *jet interface*, i.e. the boundary separating turbulent from non–turbulent fluid, statistical quantities could be determined as a function of the distance to this. These authors were inspired by the contemporary investigations by Bisset et

[†]Department of Mechanical and Systems Engineering, Gifu University, Gifu, Japan.

[‡]Laboratory for Aero and Hydrodynamics, Delft University of Technology, The Netherlands and Department of Space and Climate Physics, University College London, UK.

al. [14], who carried out a similar analysis based on direct numerical simulations of a turbulent wake behind a flat plate. (For the present purpose, the basic features of a free turbulent jet and a free turbulent wake are the same. In both cases a turbulent region is surrounded by a region of irrotational fluid. Only difference is which region has the highest mean velocity). However, the investigations presented by Westerweel et al. were only based on a subset of the total data ensemble and apparently at a spatial resolution lower than what could be achieved from the raw PIV data. Thus, questions as to whether an improvement of the statistical accuracy, including all the available data, or raising the spatial resolution would have an effect on the outcome of the analysis remained unanswered. The search for an answer to these questions is what has made up the prime motivation for the present work.

9.2 Self similarity

One of the properties of the axisymmetric turbulent jet is that it is self–similar. Since the self similarity parameters are used for scaling of the results in the subsequent sections, a few lines are now devoted to a description of the concept of self similarity.

An axisymmetric flow, in general, is said to be self–similar (or self–preserving) if the mean velocity profile can be written in polar coordinates as

$$U(z,r) = U_c(z)f(\eta) \tag{9.1}$$

and (with good approximation)

$$\langle u'v' \rangle (z,r) = U_c^2(z)g(\eta) \tag{9.2}$$

with $\eta = r/b(z)$, where r is the radial position and $b(z)$ a length scale. The validity of the latter of these requirements has often been questioned and an extended, more accurate, expression now exists (see e.g. [15]). The scaling parameters used in the present study are derived from an expression based on equation (9.1) only. Hence, as this expression is generally believed to be valid these issues will be of no consequence to the results described below. Experimental data have shown that the velocity and shear stress profiles for a jet can become self-similar as quickly as 10 orifice diameters downstream of the jet exit. Self similarity of other statistical quantities such as the turbulence intensity may not be established till after about 35 orifice diameters [15]. For a jet, $U_c(z)$ is chosen as the centerline velocity. Thus, from (9.1), plotting the mean axial velocity normalized by the local centerline velocity as function of η, the result becomes identical for all z in the self–similar region. This is the essence of the property of self similarity.

To avoid the use of polar coordinates, the following description will use x to denote downstream position and y to denote the vertical position, thus conforming with the cartesian coordinate system of the PIV images with origin at the lower left corner. Traditionally, the variable b is chosen as the jet half-width, defined as the value of y where U has dropped to $0.5U_c$. For turbulent jets it can be shown (see e.g. [72]) that b and U_c are proportional to x and x^{-1}, respectively. Further, the mean velocity profile at a given downstream position is very well represented by a Gaussian profile.

Accordingly, the form of equation (9.1) applied for the present investigations is written:

$$U(x,y) = \underbrace{U_0 \frac{B_u d}{x - x_0}}_{U_c(x)} \exp\left\{ - \left[\frac{y - y_0}{C_1 (x - x_0)} \right]^2 \right\} \tag{9.3}$$

Here U_0 is the mean velocity at the jet orifice, d the nozzle diameter, y_0 the vertical centerline position, C_1 a constant, and B_u the so-called decay constant. The last parameter, x_0, states the location of the *virtual origin* of the jet. The virtual origin corresponds to the position where the two straight lines, representing the mean jet boundary, intersect the symmetry line. If $x = 0$ corresponds to the jet orifice x_0 will be negative if the jet starts to spread directly from the orifice. For the present flow, x_0 is positive as the jet leaves the orifice in a top-hat profile and does not start spreading until several nozzle diameters downstream. Evidently, the position of the virtual origin is highly dependent on the inflow conditions. Hence, to facilitate comparison between results obtained from different measurements or numerical simulations, the downstream position should always be measured relative to x_0.

Performing a least mean-squares approximation to equation (9.3), including all data from the mean velocity field, values of B_u, x_0, y_0, and C_1 are obtained. Afterwards, setting $U = 0.5U_c$, an expression for $y_b(x)$ corresponding to the position of the jet half-width can be found. Part of the present study includes an investigation of how the statistical quantities derived for the free turbulent jet evolve with downstream position. For this purpose the local mean centerline velocity and jet half-width will be used as scaling parameters.

Before turning to the actual results, the following section provides a description of the (re–)processing of the raw PIV and LIF data.

9.3 Data processing

The current section provides an overview of the processing of the raw PIV and LIF data which was carried out as the first part of the present study. For completeness, the section starts with a short description of the original data ensemble. The concept of LIF will be explained in the last part of the section in connection with the comments on the processing of these data.

9.3.1 The data ensemble

As already pointed out, the data set used for the investigations presented in this chapter was originally recorded by Fukushima et al. [31]. The measurements were made in a rectangular section of size $110 \times 110 \times 300$ mm^3 fitted in a closed-loop water facility. The jet issued perpendicular to one end wall at a mean velocity of $U_0 = 2\frac{\mathrm{m}}{\mathrm{s}}$ from a nozzle of diameter $d = 1$ mm and thus was characterized by a Reynolds number of $Re = 2000$. The data was obtained in areas of about 45×45 mm^2 centered at three different downstream positions namely $x/d = 40, 80,$ and 120. For the present study the data sets obtained at $x/d = 40$ and 80 was considered. In this thesis only results

from the latter will be discussed. The experimental technique used to obtain these data can be summarized as follows. (For further details please refer to [31] or [92].)

For the illumination of the PIV and LIF images a twin frequency–doubled pulsed Nd:YAG laser and a CW Ar^+ laser were used, respectively. The laser beams were combined along the same optical path to form a single light-sheet in the measuring domain. Two cameras were then placed on opposite sides of the test section with their optical axes perpendicular to the light-sheet plane for recording PIV and LIF images, respectively. The time between pulses for the PIV recordings was set to 1.2 ms and the exposure for a LIF image was 2.4 ms, complying with the maximum velocities occurring in the region centered at $x/d = 80$. The LIF recordings were made with a small time delay following the PIV recordings in order to avoid mutual influence of the recordings. However, the total recording time was 5 ms, which is small compared to the Kolmogorov timescale (≈ 20 ms) and hence the combined PIV and LIF measurements could be considered simultaneous.

Twelve measurement series were carried out, each yielding 67 pairs of PIV images and 67 LIF images. Thus the original data ensemble consisted of data representing a total of 804 combined PIV and LIF images. However, not all of these data could be used. Due to problems in the acquisition system, a PIV recording was skipped from time to time and also some of the LIF images turned out bad. As will be explained in the following, fortunately these problems could be solved in a rather elegant way.

9.3.2 PIV processing

The PIV data was processed using the in–house code developed at the Laboratory for Aero and Hydrodynamics, Delft University of Technology. The results reported by Westerweel et al. [92] were based on vector maps with a spatial resolution corresponding to an interrogation area (IA) size of 32×32 pixels. One of the objectives of the present investigations was to improve this resolution aiming at a final resolution corresponding to an IA size of 16×16 pixels. The steps of the procedure leading to this are explained in the following.

As mentioned above, a PIV image was skipped from time to time during the recordings. Hence, before processing the PIV data the recorded image pairs had to be checked for contiguousness. First an IA size of 128×128 pixels and use of zero percent overlap was specified in the input file. In this way, a conservative estimate of the displacement was obtained and the computation time drastically reduced compared to what was needed for the final resolution. Processing the images of a given measurement series the average displacement in the x–direction for each image was written to a file. Plotting the contents of this file as function of image pair index, it could then be determined which image pairs were not contiguous[1]. Thus, removing solitary PIV images from the 12 datasets a total of 794 contiguous image pairs resulted.

Having checked for contiguousness, the conversion from raw image data to velocity vector maps with a final resolution corresponding to 16×16 pixel IAs was carried out in the following steps:

[1] Obviously, the average displacement in the x–direction for the free jet should be at a significant positive value for all realizations.

1. Interrogation on 32×32 IA grid using 50% overlap and replacement of spurious vectors detected by median test

2. Interrogation applying window shifting on 32×32 IA grid using 50% overlap and replacement of spurious vectors detected by median test

3. Interpolation of result of step 2 to 16×16 IA grid with 50% overlap

4. Interrogation applying window shifting on 16×16 IA grid using 50% overlap and replacement of spurious vectors detected by median test

5. Interrogation applying window shifting on 16×16 IA grid using 50% overlap and replacement of spurious vectors detected by median test

6. Interrogation applying window shifting on 16×16 IA grid using 50% overlap, replacement of spurious vectors detected by median test, and conversion to physical coordinates

Using a 50% overlap the 32×32 IA interrogation yielded vector maps of 61×61 vectors each in total. To detect spurious data, a local–median test was applied to the resulting vector maps. The test returned the magnitude of the difference between the actual displacement and the local median displacement. The threshold value used to label bad vectors was fixed at 2.5 pixels ($\sim 0.1\frac{\mathrm{m}}{\mathrm{s}}$) for the 32×32 IA resolution and at 1.0 pixels ($\sim 0.04\frac{\mathrm{m}}{\mathrm{s}}$) for the 16×16 IA resolution. As explained by Westerweel in [90], the local–median estimator is less sensitive to outliers in the neighborhood from which the local median displacement is computed than the local mean estimate. Hence the median test was preferred. To improve the result of the interrogation at the 32×32 IA resolution, the result of the first step was utilized in a second run to apply window shifting. Moving the IAs in the second image over the local integer displacement in pixels, the accuracy of the cross–correlation is improved resulting in a reduced number of outliers. The principle is the same as in adaptive correlation (see chapter 5). For further details please refer to [87].

To proceed with the interrogation on a 16×16 IA grid, displacement files at this resolution had to be obtained for window shifting. This was crucial as the time between pulses used for the measurements was adjusted to ensure that the in-plane displacement was less than 25% of the IA side length for 32×32 pixel IAs (cf. section 1.2). For this an interpolation script was created, which took as input each vector map from the result of the interrogation at the 32×32 IA resolution and produced vector maps of 121×121 vectors each in total, corresponding to a 16×16 IA resolution with a 50% overlap. It can be noted that a new displacement field at twice the resolution could also have been obtained by applying a 75% overlap at the 32×32 IA resolution. However, gross overlapping is not a good solution as this may create "islands" of outliers in the initial interrogation causing an irreparable error on the result.

Having constructed displacement files for the 16×16 IA cross–correlation all the images were interrogated thrice, each time using the improved displacement field as input for the window shifting. In this way the final vector maps contained less than 4% spurious vectors based on the median test before these were replaced. In the last run, all the vector maps were flipped upside down before they were saved to the disc.

This final operation was necessary in order to bring the data from matrix notation, i.e. with the origin at the top left corner to the more physical, geometric notation with origin at the bottom left corner.

9.3.3 LIF processing

Laser induced fluorescence (LIF) also referred to as planar laser induced fluorescence (PLIF)[2] can be used to obtain the instantaneous concentration distribution in a planar cross section of a liquid flow. The concentration is measured from the amount of light emitted by a fluorescent dye when illuminated by a light source with a known intensity distribution. In fact the intensity of the light emitted is directly proportional to the local concentration of the dye.

In the measurements used for the present study *fluorescein* was added to the incoming jet flow. For fluorescein the ratio of kinematic viscosity to molecular diffusivity, also known as the Schmidt number, is $Sc = 2075$, implying that the molecular diffusion was negligible compared to the turbulent diffusion. In this way the boundary of the jet fluid did not become blurred by the effect of molecular diffusion. An important property for the current investigations, recalling that one of the main points is to detect the position of the jet interface.

The illumination used to produce the LIF images was not homogeneous. Hence the LIF images had to be normalized by the intensity distribution of the illumination. For this purpose Fukushima et al. recorded 100 images of a known uniform dye concentration. The average of these then represented the intensity distribution. After each measurement series 50 images without illumination were recorded to determine the dark background level. Correcting the instantaneous measurements by the background level, and normalizing by the intensity distribution corrected by the background level, the correct concentration could then be obtained. A useful illustration of the procedure is provided by the following equation:

$$C^n(x,y) = \frac{I^n(x,y) - B(x,y)}{L(x,y) - B(x,y)} \tag{9.4}$$

where I^n denotes the measured concentration at time n, B is the mean background level, L is the uncorrected light intensity distribution, and C^n denotes the corrected instantaneous concentration at time n. These are the steps taken in general to process LIF data. For a more detailed description of the theory of LIF the reader may refer to [84] or [86].

After processing the LIF data a final step before the data analysis was carried out to check for contiguousness of the PIV and LIF images. The two components of the Reynolds flux in each point of a 2D domain are found as the ensemble average of the product of the fluctuating part of the two velocities and the concentration. A combined PIV and LIF image contributes significantly to this average only if the two are contiguous. Thus, calculating the *instantaneous* turbulent contribution to the total concentration flux it could be checked whether given PIV and LIF images were contiguous. In the jet region the vertical component of the turbulent flux is negative

[2] As opposed to pointwise laser induced fluorescence.

below the jet and positive above the jet whereas the streamwise component is positive on both sides. Hence, the vertical component was best suited for the check. Figure 9.1 shows a typical example of instantaneous Reynolds flux in the y–direction. The $v'c'$

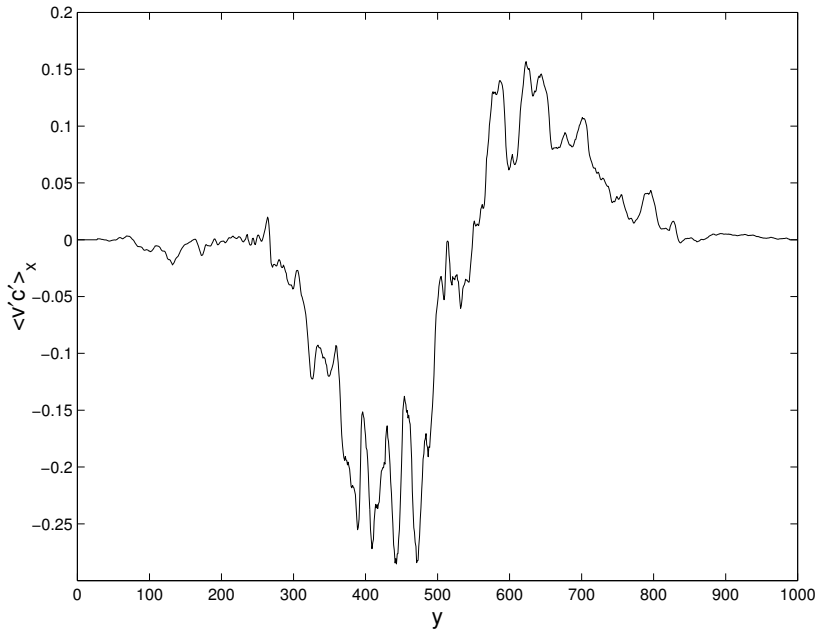

Figure 9.1: *Instantaneous turbulent contribution to mean concentration flux.*

field has been averaged horizontally (denoted by $\langle\cdot\rangle_x$) and plotted as function of y in pixels. Obviously a graph like the one shown in figure 9.1 was not plotted for every pair of PIV and LIF images. Instead, the standard deviation, $\sigma_{v'c'}$, of the instantaneous correlation was calculated for each pair in a measurement series and plotted as function of image pair index. As the mean value was about zero large values of $\sigma_{v'c'}$ indicated contiguousness whereas low values indicated non–contiguousness. Using this criterion a total of 660 contiguous PIV and LIF images was found from the initial ensemble of 794 and 706 usable PIV vector maps and processed LIF images, respectively.

The following sections present selected results from the analysis of the combined PIV and LIF measurements. The term "conventional" has been chosen to describe the statistical quantities found from classical ensemble averages such as the mean velocity and concentration fields. Taking ensemble averages of the different quantities relative to the turbulent/non-turbulent interface, i.e. the jet boundary, the resulting statistics are labeled "conditional".

9.4 Conventional statistics

In the present section examples of instantaneous flow realizations are provided and the mean velocity field, derived from the dataset described above, is shown. Further, the results obtained from the self similarity analysis of the mean velocity field are discussed.

9.4.1 Instantaneous flow realizations

Figure 9.2 shows an example of an instantaneous velocity field consisting of 121 × 121 velocity vectors corresponding to 16 × 16 IA resolution with 50% overlap. The mean

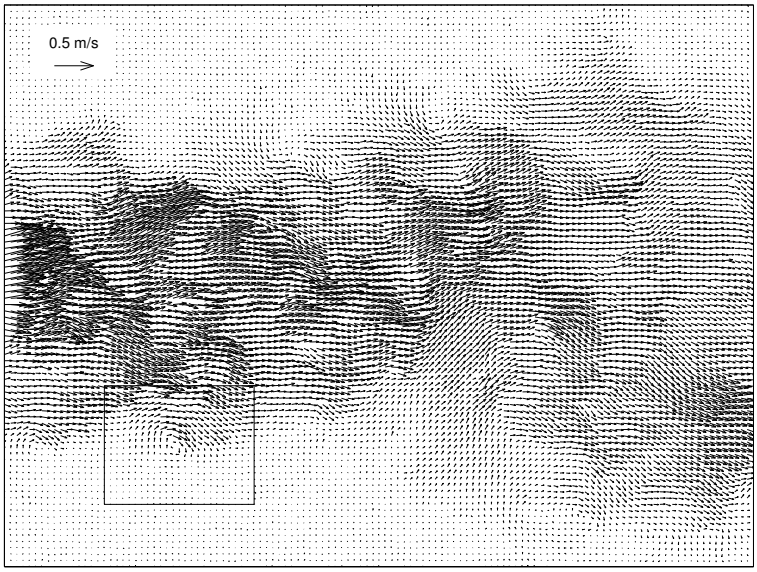

Figure 9.2: *Example of instantaneous velocity field from the free axisymmetric turbulent jet.*

jet flow is from left to right. As expected the velocities are seen to be highest near the left boundary of the domain. However, small regions with bursts of high velocity are seen within the jet at several locations downstream, which indicate that the jet is characterized by high levels of turbulence. The velocity field shown also gives an impression of how the jet spreads with downstream position. The spreading in the region considered ($60 \lesssim x/d \lesssim 100$) is quite limited on average, however.

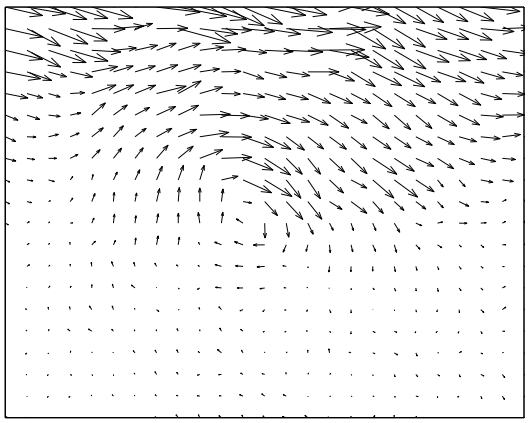

Figure 9.3: *Close-up of instantaneous velocity field near turbulent/non-turbulent interface.*

The effects of the high spatial resolution are visualized in figure 9.3 through a close-up of the region marked by a rectangle in figure 9.2. The plot depicts a small vortex in the region where the flow changes from turbulent to non-turbulent. As will be shown in the following section the improvement of resolution, from 32×32 IAs to 16×16 IAs, has had a positive effect on the quality of the conditional statistics.

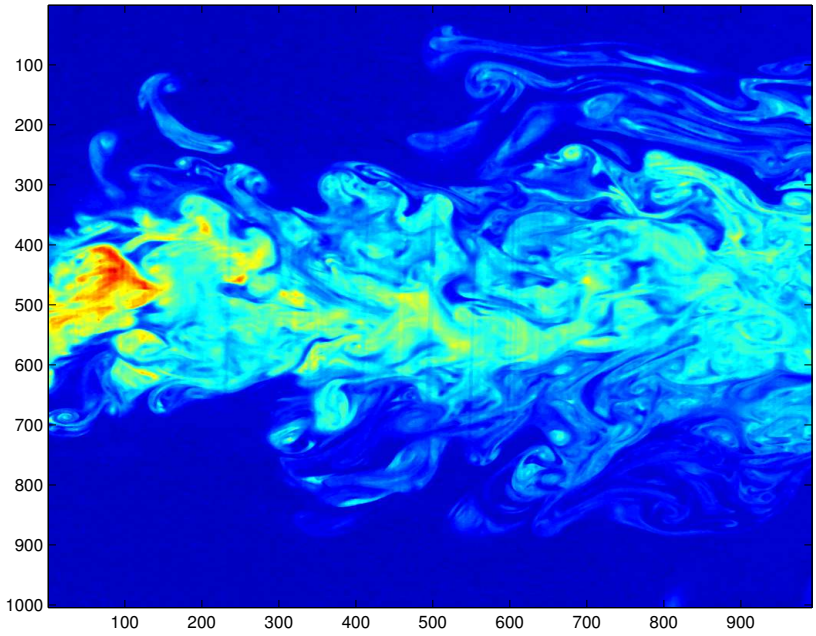

Figure 9.4: *Example of instantaneous concentration field.*

An example of an instantaneous LIF image can be seen in figure 9.4. The "jet fluid" is defined as the fluid in regions with concentration above a certain level (see section 9.5). Most of the jet fluid is connected to a large region with high concentration near the symmetry axis. However, small regions of detrained jet fluid are observed in "islands" outside the jet. An example is seen around $(x_\mathrm{p}, y_\mathrm{p}) \approx (200, 200)$, (subscript "p" indicating pixel coordinates). Also small regions of entrained "ambient fluid" are found inside the jet appearing as small "holes". Starting from figure 9.4, the procedure used to detect the jet interface will be summarized in section 9.5.

9.4.2 Mean field and self similarity

The mean velocity field based on all snapshots included in the analysis is shown in figure 9.5. Only every second vector is shown to avoid crowding. A vector of length corresponding to the order of the maximum velocity in the domain considered has been included in the top left corner for reference. Mean streamwise velocity profiles calculated from equation 9.3 have been plotted on top (in red) at downstream positions corresponding to the left boundary and the center of the domain ($x/d \approx 80$), respectively. The calculated profiles are found to represent the actual U–profiles excellently at both positions.

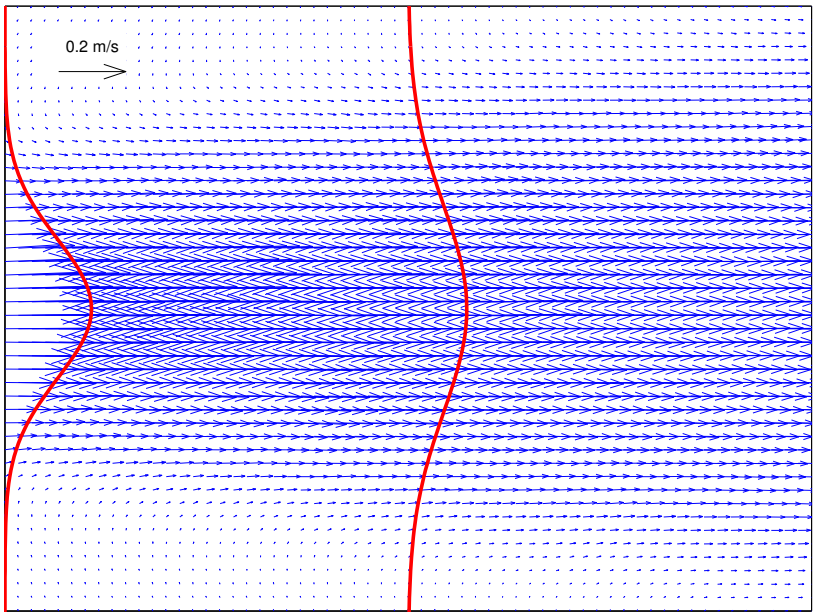

Figure 9.5: *Mean velocity vector field and examples of streamwise velocity profiles from equation 9.3.*

Performing the least mean-squares fit[3] to equation 9.3, the position of the virtual origin was found to be located approximately 13.5 mm downstream of the jet orifice. This value is significantly larger than the 4.9 mm determined from a DNS performed by Boersma et al. [15] and even lower values from earlier experimental data which they used for comparison. However, these results were all obtained at higher Reynolds numbers than for the present jet indicating a higher initial level of turbulence, which would cause the jet to start spreading earlier after the exit. The value of the decay constant, B_u, in equation 9.3 was found to be 5.9, which is identical to the value found by Boersma et al. These results support what was also suggested by the comparisons made in [15], namely that B_u is less dependent on the initial conditions than x_0.

9.5 Conditional statistics

The present section reports part of the results obtained from the conditional statistics derived for the free turbulent jet. First, the procedure for detecting the jet boundary is outlined. Second, horizontally averaged conditional quantities are discussed and finally, the evolution of some of the conditional statistics with downstream position is described.

9.5.1 Boundary detection

Using the LIF image shown in figure 9.4 as example, the steps leading to the determination of the jet boundary from the LIF images are illustrated in figures 9.6(a)–9.6(d).

[3]The fit was based on a routine prepared by J. Westerweel using the NAG–library.

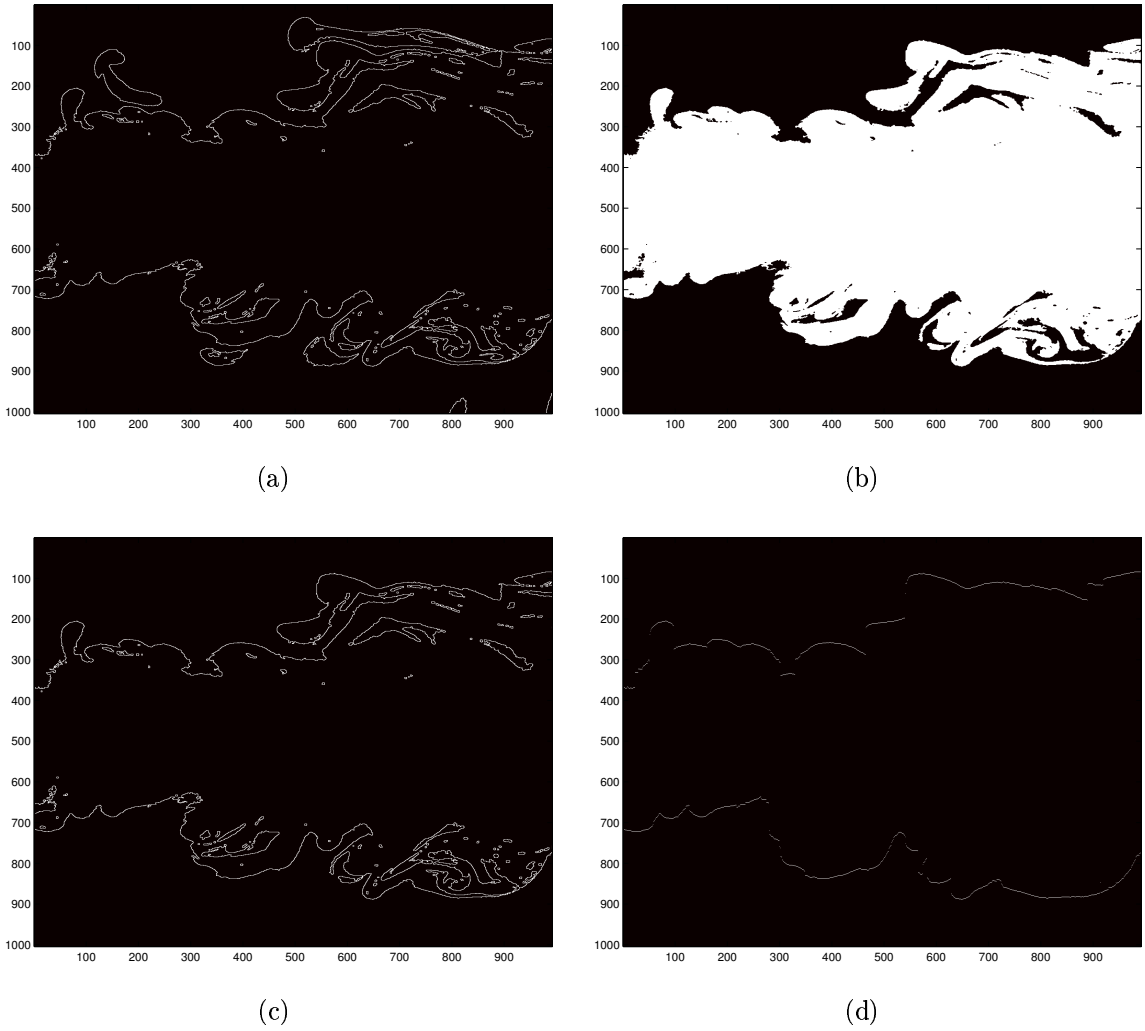

Figure 9.6: *Detection of jet boundary from LIF data.* (a) *All boundaries separating jet fluid and ambient fluid.* (b) *Jet body.* (c) *Intersection of* "a" *and* "b". (d) *Final result keeping outer points only.*

First the image was transformed into a binary image applying a threshold value. The value 1 was assigned to pixels with a gray value above the threshold value and the value 0 to the remaining. (Details of the choice of threshold value, based on a procedure first described by Prasad and Sreenivasan [69], can be found in [92]). Thus, having labeled "jet fluid" and "ambient fluid", respectively, the interfaces separating the two could be detected. The plot in figure 9.6(a) shows all boundaries detected from the binary image resulting from the raw LIF image[4]. As described in connection with figure 9.4 regions of detrained jet fluid are observed. To remove these first an image containing the value 1 only in the "body" of the jet was derived. This was done by keeping all points connected to a point located at the symmetry line just downstream of the left boundary of the domain. The result of this operation can be seen in figure 9.6(b).

[4] The scripts leading to this result as well as the one shown in figure 9.6(d) were originally developed by T. Hofmann, ETH Zürich, Switzerland.

The intersection of pixels with value 1 of the jet body and the boundaries found in figure 9.6(a) then made up all boundaries connected to the jet body as shown in figure 9.6(c). The shape of the boundary thus obtained is seen to be quite complex. Hence, to simplify the further analysis a last operation was performed to yield a boundary consisting only of the outermost points at each x–position. The final result is shown in figure 9.6(d).

To illustrate the strength of the procedure outlined to separate turbulent from non-turbulent motion, figure 9.7 shows the vorticity field derived from the PIV velocity field corresponding to the LIF image used above. The jet boundary from figure 9.6(d) has

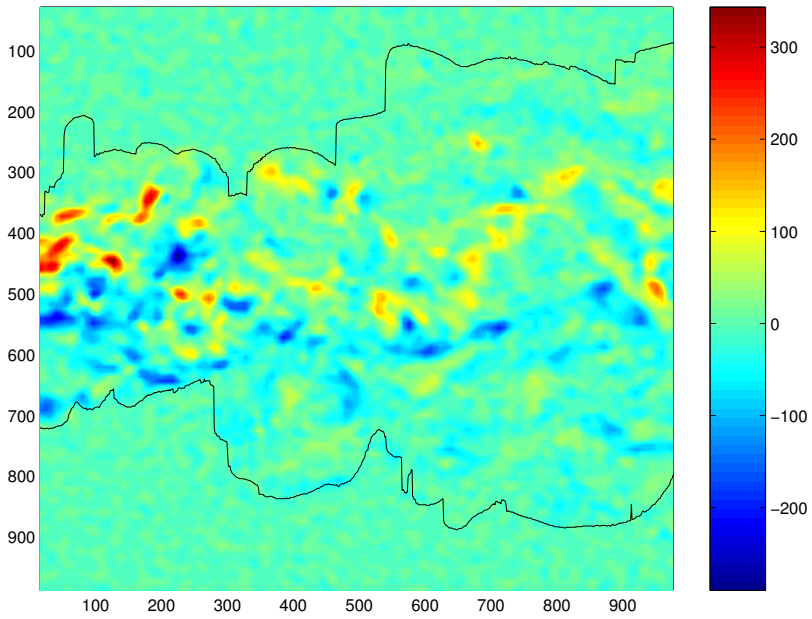

Figure 9.7: *Vorticity field from PIV image corresponding to the LIF image in figure 9.4 with indication of the jet boundary derived from the LIF image.*

been plotted on top of the vorticity field. Evidently the boundary does a good job in separating the regions of rotational and irrotational fluid.

9.5.2 Horizontally averaged quantities

Having determined the position of the jet boundary for all LIF images, conditional statistics could be derived for the different flow parameters. Considering for instance the streamwise velocity component, $u(x, y)$, a coordinate transformation leading to $u(x, y - y_I)$ where y_I denotes the instantaneous position of the jet boundary was performed. From the instantaneous conditional fields the ensemble averaged mean conditional field could then be calculated. Finally, averaging along horizontal lines, i.e. lines with constant $y - y_I$, the horizontally averaged conditional mean of u was obtained. In the following, plots of selected quantities will be shown and the results discussed. It is noted that no scaling has been applied obtaining these results. The purpose of the investigation is to examine the change of a given quantity across the jet

interface for which no scaling is required. In the next section where the downstream evolution of the different quantities is considered, the variables are scaled by the mean centerline velocity and jet half-width, derived from equation (9.3). As indicated by the figure axes, an interval covering $-300 < y - y_I < 300$ px was chosen for the analysis. This corresponds to approximately 27 mm. Since the results as expected are more or less identical whether the statistics are derived with respect to the lower or the upper boundary, it has been chosen to show results with respect to the upper boundary only.

Figures 9.8 and 9.9 show the horizontally averaged conditional statistics for u and the out-of-plane vorticity, ω_z, denoted by $\langle U \rangle_x$ and $\langle \Omega_z \rangle_x$, respectively. Conforming with the notation used for detection of the the jet interface y increases when moving downwards. Hence, values of $y - y_I$ smaller than zero correspond to positions above the upper boundary.

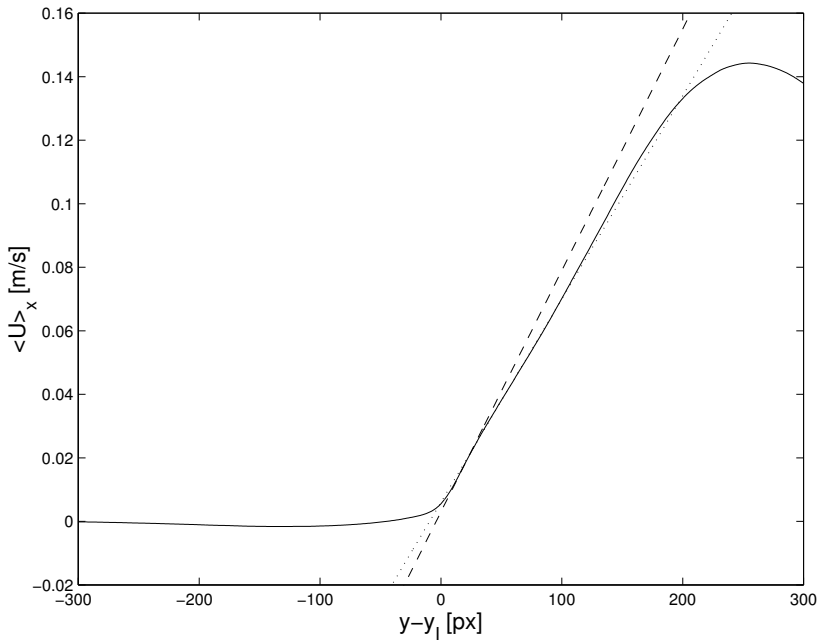

Figure 9.8: *Horizontally averaged conditional mean of u–velocity. Dashed and dotted lines indicate change in velocity gradient.*

As expected the streamwise velocity and the vorticity are both seen to drop to zero outside of the jet region. The $\langle U \rangle_x$–profile increases to a maximum at $y - y_I \approx 250$ px corresponding to the position of the jet center and starts to drop again approaching the lower boundary. Interestingly, a change in velocity gradient is observed a short distance below the jet boundary. This is illustrated by the dashed and the dotted line representing the slope just within the boundary and the slope in the interval covering $25 \lesssim y - y_I \lesssim 50$ px, respectively. Clearly, the velocity gradient drops to a lower value at $y - y_I \approx 25$ px. The phenomenon is also reflected in the profile for $\langle \Omega_z \rangle_x$ (figure 9.9). A vorticity maximum is found just within the jet boundary agreeing with the large (negative) value of $\frac{\partial U}{\partial y}$ in this region. The cause of this result is probably a high concentration of vorticity at the jet interface related to a frequent occurrence of small vortices in this region (cf. figures 9.2 and 9.3). This effect has never been

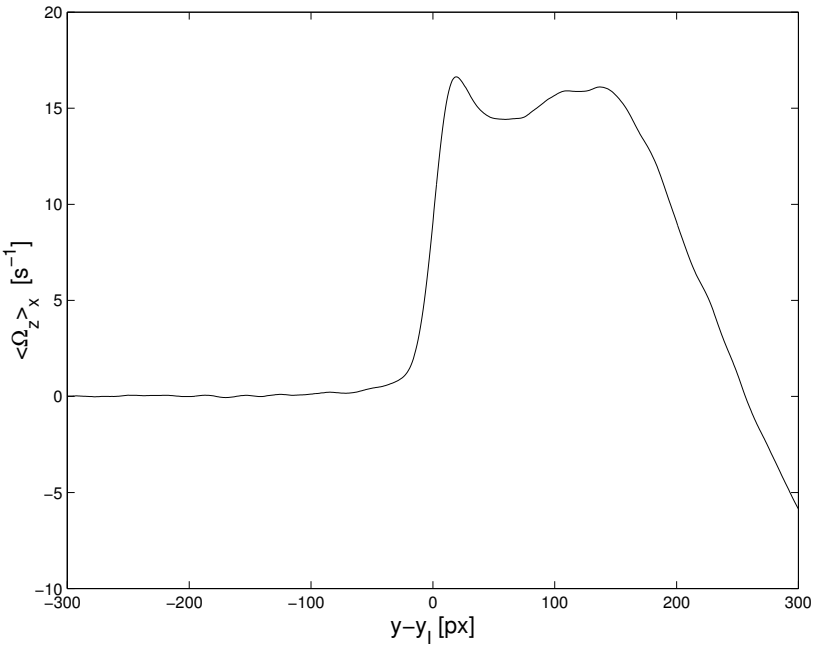

Figure 9.9: *Horizontally averaged conditional mean vorticity.*

measured before and thus constitutes one of the most important results of the present investigations. In fact it controverts earlier theories, which state that no discontinuity exists in this region (see [76] and references therein). As shown below, the result would not have been obtained without the improvement in statistical accuracy provided by the present analysis.

The results in figures 9.8 and 9.9 were both based on the total ensemble of combined PIV and LIF images at a spatial resolution corresponding to 16×16 IAs. Figure 9.10 illustrates the effect of the improved resolution and increased number of images included in the statistical analysis compared to the results presented by Westerweel et al. [92]. The curves show $\langle \Omega_z \rangle_x$ based on the first dataset consisting of 67 pairs of PIV and LIF images at resolutions corresponding to 32×32 IAs and 16×16 IAs, respectively. The change in vorticity across the jet interface is steeper for the 16×16 IA resolution than for the 32×32, which indicates an improved effect on the results using the higher resolution. The characteristic peak just within the the jet boundary is not observed in either of the profiles. Hence, the interesting results discussed above would not have been obtained without increasing the number of realizations included in the analysis as well as the spatial resolution. All in all, it can be concluded that the investigations presented here have indeed been worth the effort.

9.5.3 Downstream evolution

In order to study how the different flow quantities develop with downstream position, plots have been made of unscaled and scaled conditionally averaged data for different values of $(x - x_0)/d$. The scaling parameters used are the mean centerline velocity, $U_c(x)$, as defined by equation (9.3) and the jet half-width, $b(x)$. Thus, for a given

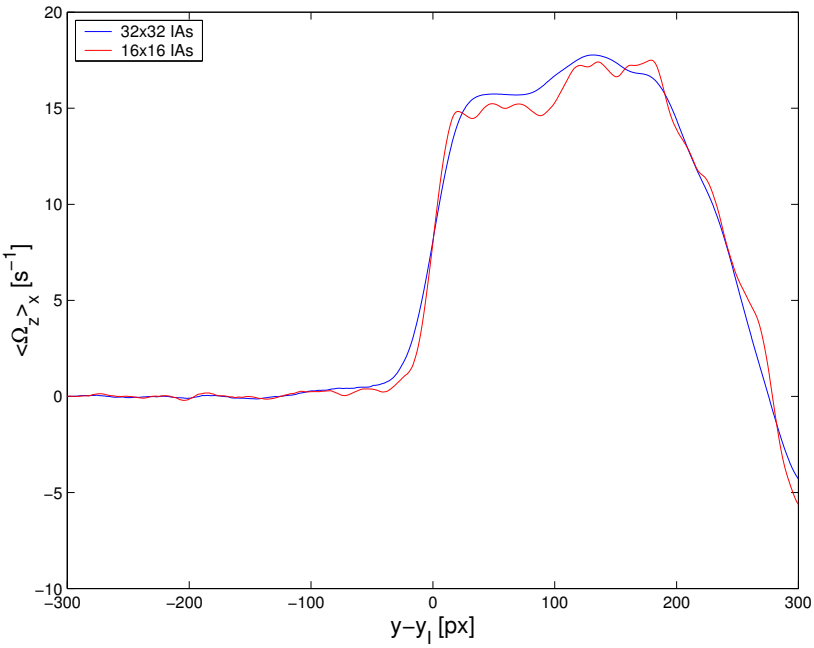

Figure 9.10: *Comparison of conditional vorticity field at different resolutions based on a single dataset.*

downstream position, the conditional mean of, for example, u is plotted as $\langle U(y-y_I)\rangle_{\Delta x}$ and $\langle U((y-y_I)/b(x))/U_c(x)\rangle_{\Delta x}$, respectively. The notation $\langle\cdot\rangle_{\Delta x}$ has been used to indicate that the profile at a given position is obtained as the average of this quantity over an interval of $\Delta x = 200$ px centered at the x–position in question.

Figures 9.11(a) and 9.11(b) show the results for u at three evenly spaced downstream positions. As expected, the streamwise velocity within the jet region is seen to decrease with increasing x for the unscaled data. However, scaling the variables by $U_c(x)$ and $b(x)$, as shown in figure 9.11(b), the profiles become practically identical at all three positions. Hence it can be concluded that the conditional mean of u scales with these parameters. It is noted that the interval for $(y-y_I)/b(x)$ becomes narrower the further the downstream position, which is, of course, an effect of the increased jet width.

For the sake of variation, the y–component of velocity has been chosen to present the conditional mean profiles for the root mean squared values of the fluctuating part of the velocities. The results are shown in figure 9.12. The U_{RMS}–profiles look almost the same just at a slightly higher level of magnitude. Although not as perfectly as in the case of the u–velocity the conditional RMS–profiles are also seen to scale with the self similarity parameters. An interesting thing to notice is that the RMS value does not drop instantly to zero outside the jet region. The same phenomenon was observed by Bisset et al. [14], who explained that random irrotational velocity fluctuations are induced on the non-turbulent side as result of a combination of vorticity on the turbulent side and the irregular shape of the instantaneous jet interface. The fluctuations are induced over a distance of the order of the characteristic length scale in the streamwise direction within the turbulent region.

As the last example, the evolution of the conditional vorticity field with downstream

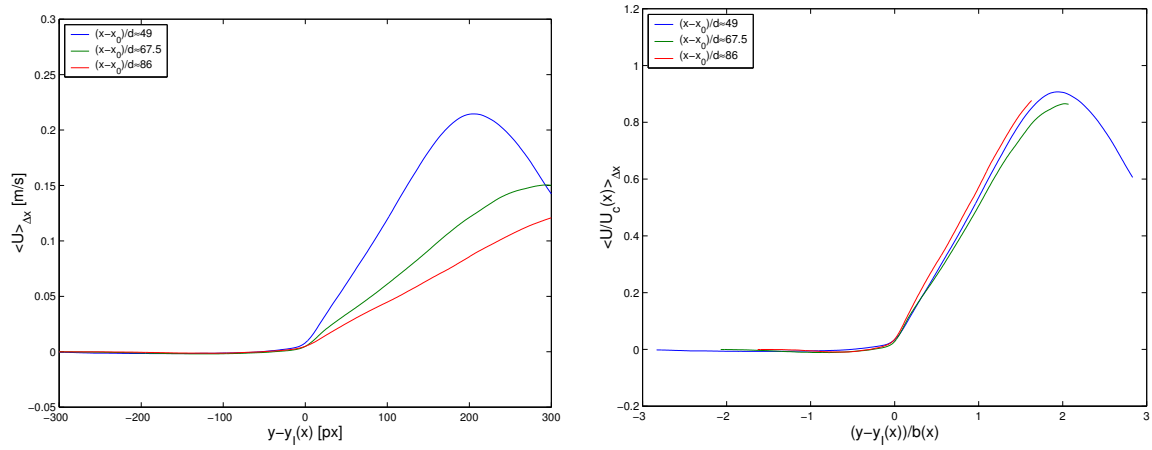

(a) (b)

Figure 9.11: *Conditional U–profiles relative to upper jet boundary at different downstream positions.* (a) *No scaling applied.* (b) *Scaled with self similarity parameters.*

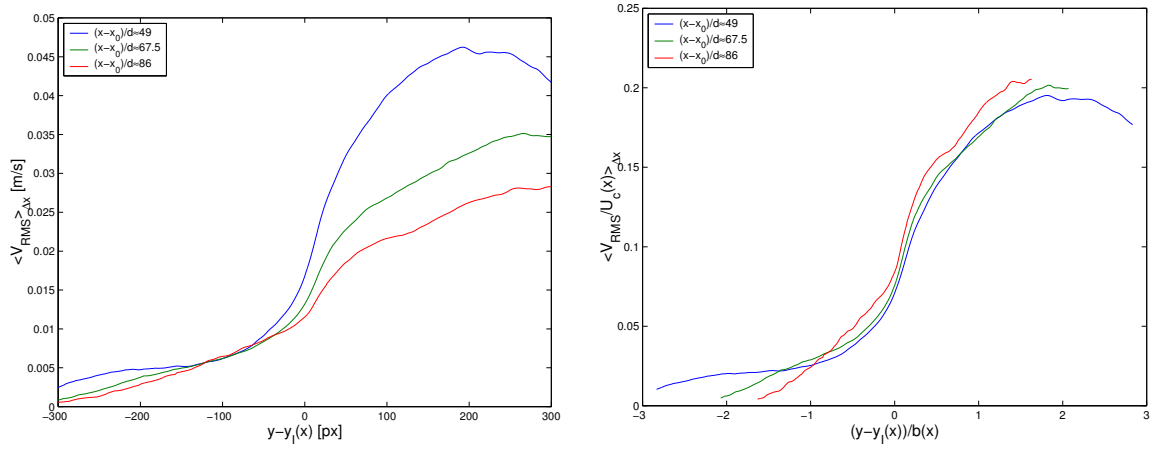

(a) (b)

Figure 9.12: *Conditional V_{RMS}–profiles relative to upper jet boundary at different downstream positions.* (a) *No scaling applied.* (b) *Scaled with self similarity parameters.*

position is considered. Figures 9.13(a) and 9.13(b) show the Ω_z–profiles without and with scaling, respectively. As expected, the magnitude of the conditional vorticity

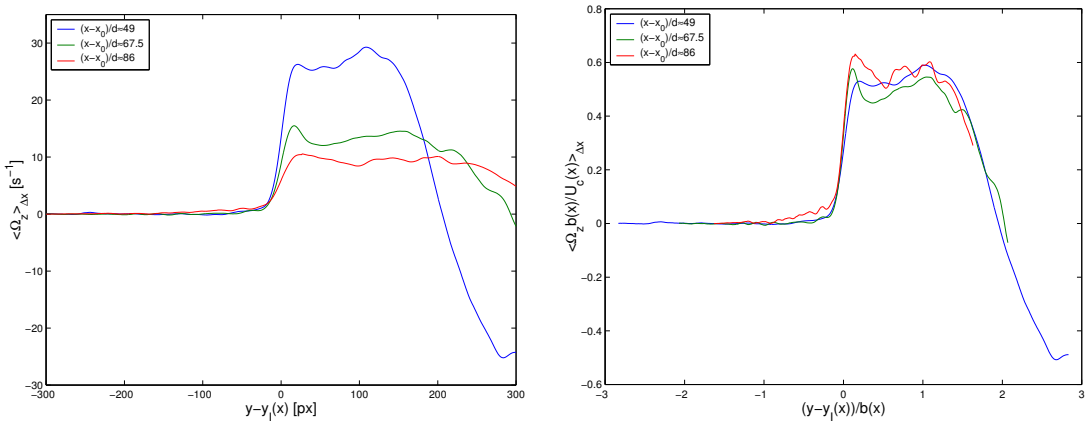

(a) (b)

Figure 9.13: *Conditional Ω_z–profiles relative to upper jet boundary at different downstream positions.* (a) *No scaling applied.* (b) *Scaled with self similarity parameters.*

within the jet region decreases with downstream position. Applying the scaling, the profiles at the three positions become more or less identical and thus, apparently, also Ω_z scales with $U_c(x)$ and $b(x)$. However, on close inspection of figure 9.13(b) there seems to be a tendency to increased peak height with downstream position for the scaled profiles. This observation has incited a more detailed investigation of the peak

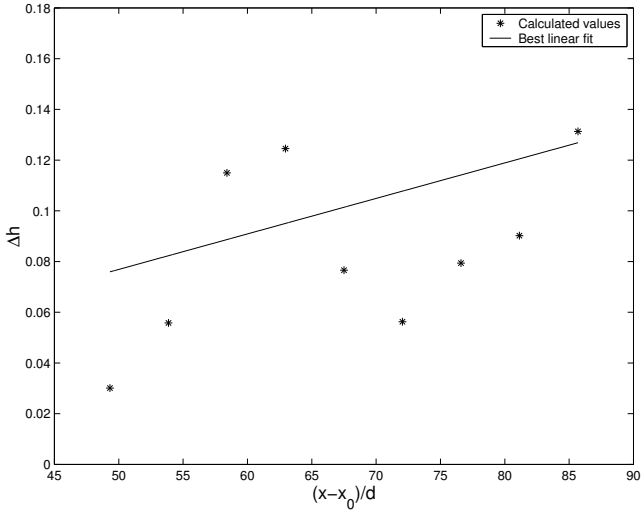

Figure 9.14: *Peak height for scaled conditional Ω_z–profiles relative to upper jet boundary as function of downstream position.*

height as function of downstream position. Specifying a universal value for the level of conditional vorticity within the jet region (in the present case 0.5 scaled units),

the peak height, Δh, for the scaled profiles could be defined as the difference between the maximum vorticity in the interval covering $10 < y - y_I < 30$ px and this level. Thus, figure 9.14 shows the peak height as function of downstream position including 9 locations corresponding to the profiles determined from 9 overlapping intervals each 200 pixels wide. A straight line has been fitted to the data to illustrate the overall behavior. Although the scatter is rather high the result suggests that the peak height increases with downstream position. It can be mentioned that a similar analysis, carried out for the dataset recorded in the measuring domain centered at $x/d = 40$, evidences the increase in peak height with downstream position much more clearly, and at a higher rate. The question is whether the result in figure 9.14 indicates a change towards better scaling with the self similarity parameters or if, indeed a self similar behavior is never established. In any case, it is clear that the vorticity profile of the free turbulent jet does not scale with $U_c(x)$ and $b(x)$ to the same extent as the mean and RMS values of the velocity.

9.6 Summary

The present chapter has reported part of a series of results obtained from investigations of a free turbulent axisymmetric jet. Most of the work was carried out during a three month stay at the Laboratory for Aero and Hydrodynamics, Delft University of Technology, The Netherlands. The investigations were carried out using an earlier recorded dataset consisting of combined PIV and LIF images. The objectives were: 1) Processing of PIV and LIF data using non–commercial software, and 2) Derivation of conditional turbulence statistics. The latter of these was motivated by a desire to improve and elaborate on earlier reported results.

Having explained the background and motivation of the study, the second section of the chapter was devoted to a description of the concept of self–similarity as a characteristic property of the axisymmetric jet. In the third section, details of the processing of the raw PIV and LIF data were given, including a short description of how the original data set was obtained. The procedure used to derive velocity vector maps at a higher resolution than earlier achieved was outlined and it was explained how the individual PIV images could be checked for contiguousness. Further, the basic steps of LIF processing were stated and it was shown how to make certain that a given set of PIV and LIF images were contiguous. The steps yielded a final ensemble of 660 combined PIV and LIF images with a spatial resolution corresponding to 121×121 vectors on a 45×45 mm^2 measuring domain.

Examples of instantaneous flow realizations were given in section four. A velocity vector field showed how very small structures can be detected from the improved resolution of the PIV data. Also, the nature of the developing jet was displayed through an instantaneous LIF realization, showing regions of "detrained" and "entrained" fluid, respectively. Further, the conventional mean velocity field was depicted and compared to velocity profiles derived from a self similarity analysis.

In the final section, the results of the analysis yielding the conditional statistics of the free turbulent jet were presented. First, the procedure used for detection of the jet interface from the LIF images was outlined. Second, horizontally averaged conditional

mean quantities were described, and finally, the downstream evolution of the conditional statistics was investigated applying scaling with self similarity parameters. The results showed that a change in velocity gradient, related to a maximum in conditional vorticity, occurs just within the jet boundary. Also it was found that the velocities and the RMS values of their fluctuating parts scale with the self similarity parameters when moving downstream. The same behavior is not observed for the conditional vorticity for which the height of the peak occurring just within the jet boundary seems to increase with downstream position.

The results shown in this chapter demonstrate the many possibilities provided by the present approach for exploration of the free axisymmetric turbulent jet. Although some of the most important findings have already been presented here many more remain to be reported. For further results and interpretation, the interested reader may refer to the forthcoming paper by Westerweel et al. [93], which will be based on the work described in the present account.

Chapter 10

Conclusions

The work presented in this dissertation has demonstrated the powerfulness of a combination of Particle Image Velocimetry (PIV) and Proper Orthogonal Decomposition (POD) for the task of analyzing turbulent flows. Following a description of the basic theoretical concepts of turbulence and the tools used to investigate this phenomenon, three flow cases of engineering relevancy were considered. The following sections sum up the results presented for these cases and discuss the main conclusions drawn. Finally some comments are made on possible topics for future investigations.

10.1 Ventilated room

The flow in the Annex 20 room, a standard measure room used to investigate ventilation problems, has been studied through analysis of velocity data obtained with PIV. Uncorrelated as well as time resolved data was acquired in a plane near the inlet where a wall jet is formed to interact with the slowly evolving flow in the region below it. New insight into the dominant flow structures was obtained through a POD. It was found that the first ten POD modes could be divided into modes mainly related to the jet region and modes related to the complete domain. Projection of the temporally resolved dataseries onto the POD basis made possible an investigation of how the influence of the most dominant modes varies in time. The main conclusion drawn from the analysis was that flow structures which are significantly different from the mean velocity field are of importance to the flow and that the time scale of these structures can be many seconds.

Further investigations of the PIV data included a determination of the characteristic length scales of the flow in the region considered. The results indicated that the spatial resolution of the flow field sets the lower limit for the level of detail which may be extracted from a POD analysis. Also, Linear Stochastic Estimation (LSE) was applied to reproduce the dominant structures and compare with the results of the POD. While illustrating the vital importance of the choice of event data for an LSE, these investigations also showed that, as a rule of thumb, the minimum number of event points needed to reproduce a given flow pattern is equal to the number of individual flow structures in this pattern.

10.2 Jet-in-crossflow

The complex flow found in the near field of a turbulent jet-in-crossflow (JICF) has been investigated using Stereoscopic PIV and POD. Uncorrelated flow realizations, including all three velocity components, were obtained in mutually orthogonal planes near the jet exit.

First, the symmetry plane located at the center of the jet exit and extending in the downstream (crossflow) direction was considered. The mean velocity field was depicted and the mean streamline trajectory of the deflecting jet was derived. Calculation of the mean dimensionless vorticity field showed perfect agreement with earlier investigations using Laser Doppler Anemometry (LDA). Further, the existence of the characteristic jet shear–layer vortices was demonstrated through plots of instantaneous velocity realizations and the corresponding vorticity fields.

A mapping of the mean velocity field was provided by plots created at six different downstream positions and three vertical (i.e. normal to the incoming jet axis) positions. Good agreement was found between the mean flow depicted in the mutually orthogonal planes, which further yielded an excellent picture of the development of the counter–rotating vortex pair (CVP) along and downstream of the jet trajectory.

POD analyses were carried out in a number of planes to extract the dominant flow structures of the near field of the JICF. The most energetic modes were found to be centered around the location of the CVP and to be associated with velocity fluctuations normal to the symmetry plane. Earlier experimental studies have shown that the wake vortices of the JICF are initiated in the same region. Hence, as the dominant POD modes indicate the location of the maximum production of turbulent kinetic energy, it was conjectured that the maximum turbulence production in the JICF is related to the initiation of the wake vortices and that the CVP plays a significant role in the process.

After the first couple of modes a large number of modes were found to represent structure at a comparable level of energy. This result is due to the nature of the jet shear–layer vortices and indicates that many modes may be necessary to fully describe the dynamics of the JICF.

10.3 Free turbulent jet

Part of an existing database of raw measurement data, obtained with PIV and Laser Induced Fluorescence (LIF) in a free axisymmetric turbulent jet, was processed and analyzed to investigate turbulence statistics relative to the turbulent/non–turbulent interface, which exists at the boundary of this jet. The results presented were based on a dataset of combined PIV and LIF images recorded 80 orifice diameters downstream where the jet has reached a self–similar state.

Part of the study concerned processing of the raw data, which was carried out using non-commercial software. A technique used to derive reliable vector maps with very high resolution was outlined and the basic steps of LIF processing were explained. Also, it was shown how a given pair of PIV and LIF images may be checked for contiguousness in an efficient manner.

A self similarity analysis was carried out for the mean velocity field. Comparing the position of the virtual origin and the so-called decay constant of the jet with results

from earlier investigations, it was found that the position of the virtual origin is highly dependent on initial conditions, whereas the value of the decay constant seems to be universally valid.

Detecting the jet boundary from the concentration fields provided by the LIF images turbulence statistics could be derived relative to the interface. These statistics were labeled "conditional". Taking the average along lines with fixed distances to the jet boundary showed that a change in velocity gradient related to a maximum in vorticity occurs across the turbulent/non–turbulent interface. This interesting result contradicts earlier stated theories and is believed to be caused by the frequent occurrence of small scale vortices in this region.

Finally, the downstream evolution of the conditional statistics of different flow variables was investigated through scaling with the mean centerline velocity and the jet half-width. The results showed that the conditional velocities and the root mean squared values of their fluctuating parts scale with these self similarity parameters. Apparently the conditional vorticity profile does not scale with these parameters. Here the height of the scaled vorticity peak at the interface seems to slightly increase with downstream position relative to a fixed mean value within the jet region.

10.4 Topics for future investigations

The sections above have recapitulated the main results and conclusions of the present study. Many more may be obtained either by a continued exploration of the existing databases or in combination with new measurements and/or numerical simulations. Possible topics for future investigations are the following.

The investigations of the flow in the Annex 20 room were based on measurements in a single plane. Additional measurements e.g. in planes perpendicular to the symmetry plane would facilitate a study of possible 3D effects and further contribute to the understanding of the dynamics in the room.

As for the jet-in-crossflow a comparison of instantaneous realizations with the dominant POD modes still remains to be carried out. Also, a derivation of classical statistical quantities, like Reynolds stresses and turbulent kinetic energy, could be made. An obvious continuation of the investigations of the JICF would be a numerical study based on Large Eddy Simulation (LES). The results of the simulations could then be compared to the measurements e.g. through the results of POD analyses.

The results shown for the free turbulent jet represent just a small fraction of the possibilities with this dataset. Conditional statistics of the velocity–concentration correlations or an investigation of characteristic length scales as function of the distance to the interface are other possible topics of investigation. A paper is currently under preparation in which additional results and further interpretation will be presented.

Nomenclature, parts B–D

Latin

a_i	Coefficient of POD mode i
$\mathbf{a}^k$	POD coefficient vector corresponding to $\mathbf{v}_k$
$\mathbf{A}$	Matrix containing all $\mathbf{a}^k$
b	Jet half-width
B	Mean background level
B_u	Decay constant
c	Concentration
C^n	Corrected concentration field at time n
d	Orifice diameter
d_d	Diffraction limited minimum image diameter
D	Jet diameter (JICF)
f	Self similarity function
f	Spatial uu–correlation in x–direction
$f^\#$	Numerical aperture
g	Self similarity function
g	Spatial vv–correlation in x–direction
g_i^k	Components of eigenvector corresponding to λ_k
h	Inlet height, Annex 20 model
H	Height, Annex 20 model
I^n	Measured concentration field at time n
k	Turbulent kinetic energy
L	Length, Annex 20 model
L	Light intensity distribution
m	Number of basis modes in reconstruction of velocity field
M	Magnification factor
n	Total number of snapshots
N_I	Image density
r	Radial position
R	Jet-to-crossflow ratio
$\mathbf{R}$	Auto–covariance matrix
Re	Reynolds number
R_{ik}	Elements of $\mathbf{R}$
Sc	Schmidt number
t	Outlet height, Annex 20 model
t_0	Time between recordings

u	Velocity in x–direction
u_0	Mean inlet velocity
u_l	Displacement in x–direction measured by left SPIV camera
u_r	Displacement in x–direction measured by right SPIV camera
$\widetilde{u}$	Velocity in x–direction in POD space
U	Conditional mean of velocity in x–direction
U	Mean velocity in x–direction
U_0	Mean velocity at jet orifice
U_c	Mean centerline velocity
U_c	Mean crossflow velocity
U_j	Mean jet velocity
U_{rel}	Relative out-of-plane motion in x–direction in POD space
v	Velocity in y–direction
$\mathbf{v}_i$	Fluctuating part of $\mathbf{x}_i$
v_l	Displacement in y–direction measured by left SPIV camera
v_r	Displacement in y–direction measured by right SPIV camera
$\widetilde{v}$	Velocity in y–direction in POD space
V	Mean velocity in y–direction
$\mathbf{V}$	Matrix containing all $\mathbf{v}_i$
V_{rel}	Relative out-of-plane motion in y–direction in POD space
w	Velocity in z–direction
$\widetilde{w}$	Velocity in z–direction in POD space
W	Mean velocity in z–direction
W	Width, Annex 20 model
W_{rel}	Relative out-of-plane motion in z–direction in POD space
x_0	Virtual origin
$\mathbf{x}_i$	Snapshot vectors
x_{p}	x–coordinate in pixels
y_0	Vertical centerline position
y_b	Position of jet half-width
y_I	Instantaneous position of jet boundary
y_{p}	y–coordinate in pixels

Greek

Δh	Peak height
Δt	Time separation
Δx	Distance in x–direction
ϵ	Viscous dissipation
η	Scaled radial position
λ	Wavelength of laser light
λ_k	Eigenvalues of $\mathbf{R}$
Λ	Characteristic length scale (macro scale)
$\sigma_{v'c'}$	Standard deviation of velocity–concentration correlation
$\boldsymbol{\phi}^k$	POD mode k
$\boldsymbol{\Phi}$	Matrix containing all $\boldsymbol{\phi}^k$

ω_y	y–component of vorticity
ω_z	z–component of vorticity
Ω_z	Conditional mean of z–component of vorticity

Super scripts

$'$	Fluctuating part
*	Dimensionless quantity

Acronyms

CCD	Charge Coupled Device
CFD	Computational Fluid Dynamics
CS	Coherent structures
CVP	Counter–rotating vortex pair
CW	Continuous wave
DNS	Direct Numerical Simulation
IA	Interrogation Area
JICF	Jet-in-crossflow
JSV	Jet shear–layer vortices
LDA	Laser Doppler Anemometry
LES	Large Eddy Simulation
LIF	Laser Induced Fluorescence
LSE	Linear Stochastic Estimation
NAG	Numerical Algorithms Group
PIV	Particle Image Velocimetry
PLIF	Planar Laser Induced Fluorescence
POD	Proper Orthogonal Decomposition
RANS	Reynolds Averaged Navier–Stokes
RMS	Root mean squared
SPIV	Stereoscopic Particle Image Velocimetry

Bibliography

[1] Adrian, R.J. Conditional eddies in isotropic turbulence. *Phys. Fluids.*, 22(11):2065–2070, 1979.

[2] Adrian, R.J. Dynamic ranges of velocity and spatial resolution of particle image velocimetry. *Meas. Sci. Technology*, 8:1393–1398, 1997.

[3] Adrian, R.J. and Moin, P. Stochastic estimation of organized turbulent structure: homogeneous shear flow. *J. Fluid Mech.*, 190:531–559, 1988.

[4] Adrian, R.J. Particle-imaging techniques for experimental fluid mechanics. *Ann. Rev. Fluid Mech.*, 23:261–304, 1991.

[5] Adrian, R.J. Scattering particle characteristics and their effect on pulsed laser measurements of fluid flow; speckle velocimetry vs. particle image velocimetry. *Appl. Optics*, 23(11):1690–1691, 1984.

[6] Adrian, R.J. Stochastic estimation of the structure of turbulent fields. In J.P. Bonnet, editor, *Eddy Structure Identification*, pages 145–196. Springer, 1996.

[7] Arpaci, V.S. and Larsen, P.S. *Convection Heat Transfer.* Prentice–Hall, Inc., 1984.

[8] Aubry, N., Holmes, P., Lumley, J.L., and Stone, E. The dynamics of coherent structures in the wall region of a boundary layer. *J. Fluid Mech.*, 192:115–173, 1988.

[9] Aubry, N. On the Hidden Beauty of the Proper Orthogonal Decomposition. *Theoret. Comput. Fluid Dynamics*, 2:339–352, 1991.

[10] Bakewell, P. and Lumley, J.L. Viscous sublayer and adjacent wall region in turbulent pipe flow. *Phys. Fluids.*, 10:1880–1889, 1967.

[11] Batchelor, G.K. *The Theory of Homogeneous Turbulence.* Cambridge University Press, 1956.

[12] Bérengère, P. and Le Quéré, P. Low-order models for the flow in a differentially heated cavity. *Phys. Fluids.*, 13(11):3204–3214, 2001.

[13] Berkooz, G., Holmes, P., and Lumley, J.L. The Proper Orthogonal Decomposition in the Analysis of Turbulent Flows. *Ann. Rev. Fluid Mech.*, 25:539–75, 1993.

[14] Bisset, D.K., Hunt, J.C.R., and Rogers, M.M. The turbulent/non-turbulent interface bounding a far wake. *J. Fluid Mech.*, 451:383–410, 2002.

[15] Boersma, B.J., Brethouwer, G., and Nieuwstadt, F.T.M. A numerical investigation on the effect of the inflow conditions on the self-similar region of a round jet. *Phys. Fluids.*, 10(4):899–909, 1998.

[16] Bonnet, J.P., Delville, J., Glauser, M.N., Antonia, R.A., Bisset, D.K., Cole, D.R., Fiedler, H.E., Garem, J.H., Hilberg, D., Jeong, J., Kevlahan, N.K.R., Ukeiley, L.S., and Vincendeau, E. Collaborative testing of eddy structure identification methods in free turbulent shear flows. *Exp. Fluids*, 25:197–225, 1998.

[17] Chen, Q. Comparison of different k-ϵ models for indoor airflow computations. *Numerical Heat Transfer, Part B.* 28(3):353-369, 1995.

[18] Christensen, E.A., Brøns, M., and Sørensen, J.N. Evaluation of Proper Orthogonal Decomposition–Based Techniques Applied to Parameter–Dependent Nonturbulent Flows. *SIAM J. Sci. Comput.*, 21(4):1419-1434, 2000.

[19] Christensen, E.A., Sørensen, J.N., Brøns, M., and Christiansen, P.L. Low–Dimensional Representations of Early Transition in Rotating Fluid Flow. *Theoret. Comput. Fluid Dynamics*, 5:259–267, 1993.

[20] Citriniti, J.H. *Experimental investigation into the dynamics of the axisymmetric jet mixing layer utilizing the proper orthogonal decomposition.* PhD Thesis, State University of New York at Buffalo, 1996.

[21] Citriniti, J.H. and George, W.K. Reconstruction of the global velocity field in the axisymmetric mixing layer utilizing the proper orthogonal decomposition. *J. Fluid Mech.*, 418:137–166, 2000.

[22] Cordier, L. and Bergmann, M. Proper Orthogonal Decomposition: an overview. *Lecture series 2002–04* on post-processing of experimental and numerical data, von Karman Institute for Fluid Dynamics, 2002.

[23] Cordier, L. and Bergmann, M. Two typical applications of POD: coherent structures eduction and reduced order modelling. *Lecture series 2002–04* on post-processing of experimental and numerical data, von Karman Institute for Fluid Dynamics, 2002.

[24] Delville, J. Characterization of the Organization in Shear Layers via the Proper Orthogonal Decomposition. *App. Sci. Res.*, 53:263–281, 1994.

[25] Delville, J., Ukeiley, L., Cordier, L., Bonnet, J.P., and Glauser, M. Examination of large-scale structures in a turbulent plane mixing layer. Part 1. Proper orthogonal decomposition. *J. Fluid Mech.*, 391:91–122, 1999.

[26] Drazin, P.G. and Reid, W.H. *Hydrodynamic stability.* Cambridge University Press, 1981.

[27] Dubief, Y. and Delcayre, F. On coherent-vortex identification in turbulence. *J. Turbulence*, 1:011, 2000.

[28] Fabry, E.P. 3D holographic PIV with a forward scattering laser sheet and stereoscopic analysis. *Exp. Fluids*, 24:39–46, 1998.

[29] Farge, M. Wavelet transforms and their applications to turbulence. *Ann. Rev. Fluid Mech.* 24:395–457, 1992.

[30] Fric, T.F. and Roshko, A. Vortical structure in the wake of a transverse jet. *J. Fluid Mech.*, 279:1–47, 1994.

[31] Fukushima, C., Aanen, L., and Westerweel, J. Investigation of the Mixing Process in an Axisymmetric Turbulent Jet using PIV and LIF. *Proc. 10th Int. Symp. on Applications of Laser Techniques to Fluid Mechanics.* Lisbon, Portugal, July 10–13, 2000.

[32] Gamard, S., George, W.K., Jung, D., and Woodward, S. Application of a "slice" proper orthogonal decomposition to the far field of an axisymmetric turbulent jet. *Phys. Fluids.*, 14(7):2515–2522, 2002.

[33] George, W.K., Abrahamsson, H., Eriksson, J., Karlsson, R.I., Löfdahl, L., and Wosnik, M. A similarity theory for the turbulent plane wall jet without external stream. *J. Fluid Mech.*, 425:367–411, 2000.

[34] Glauser, M., Lieb, S.J., and George, W.K. Coherent structure in the axisymmetric jet mixing layer. *Proc. 5th Symp. Turb. Shear Flow*, Cornell Univ., Springer-Verlag, N.Y., 1985.

[35] Graham, W.R., Peraire, J., and Tang, K.Y. Optimal Control of Vortex Shedding Using Low Order Models. Part I: Open-Loop Model Development. *Int. J. for Numer. Meth. in Engrg.*, 44(7):973–990, 1999.

[36] Holmes, P., Lumley, J.L., and Berkooz, G. *Turbulence, Coherent Structures, Dynamical Systems and Symmetry.* Cambridge Monographs on Mechanics, 1996.

[37] Hunt, J.C.R., Wray, A.A., and Moin, P. Eddies, stream and convergence zones in turbulent flows. Technical Report, Center for Turbulence Research, CTR-S88:193, 1988.

[38] Jeong, J. and Hussain, F. On the identification of a vortex. *J. Fluid. Mech.*, 285:69–94, 1995.

[39] Johansson, P.B.V., George, W.K., and Woodward, S. Proper orthogonal decomposition of an axisymmetric wake behind a disk. *Phys. Fluids.*, 14(7):2508–2514, 2002.

[40] Jørgensen, B.H. *Low-dimensional modeling and the dynamics of the flow in a lid driven cavity with a rotating rod.* PhD Thesis, Dept. of Energy Engineering, Technical University of Denmark. ET-PHD 2000-02, ISBN 87-7475-232-4, 2000.

[41] Keane, R.D. and Adrian, R.J. Optimization of particle image velocimeters. Part I: Double pulsed systems. *Meas. Sci. Technology*, 1:1202–1215, 1990.

[42] Keane, R.D. and Adrian, R.J. Theory of cross-correlation analysis of PIV images. *App. Sci. Res.*, 49(3):191–215, 1992.

[43] Kevlahan, N.K.-R., Hunt, J.C.R., and Vassilicos, J.C. A comparison of different analytical techniques for identifying structures in turbulence. In J.P. Bonnet and M.N. Glauser, editors, *Eddy Structure Identification in Free Turbulent Shear Flows*, pages 311–324. Kluwer Academic Publishers, 1993.

[44] Kim, J., Moin, P., and Moser, R. Turbulence in fully developed channel flow at low Reynolds number. *J. Fluid Mech.*, 177:133–166, 1987.

[45] Kirby, M., Boris, J., and Sirovich, L. An eigenfunction analysis of axisymmetric jet flow. *J. Comput. Physics*, 90(1):98-122, 1990.

[46] Kirby, M. and Sirovich, L. Application of the Karhunen-Loève Procedure for the Characterization of Human Faces. In *IEEE Transactions on Pattern Analysis and Machine Intelligence*, vol. 12(1), pages 103–108, 1990.

[47] Lim, T.T., New, T.H., and Luo, S.C. On the development of large-scale structures of a jet normal to a cross flow. *Phys. Fluids.*, 13(3):770–775, 2001.

[48] Loève, M. *Probability Theory.* Van Nostrand, New York, 1955.

[49] Lumley, J.L. *Stochastic Tools in Turbulence.* Academic Press, 1970.

[50] Lumley, J.L. The Structure of Inhomogeneous Turbulent Flows. In A.M. Yaglom and V.I. Tatarski, editors, *Atmospheric Turbulence and Radio Wave Propagation*, pages 166–178, 1967.

[51] Marple, S.L. *Digital Spectral Analysis with Applications.* Prentice–Hall, Englewood Cliffs, N.J., 1987.

[52] Mathieu, J. and Scott, J. *An Introduction to Turbulent Flow.* Cambridge University Press, 2000.

[53] Maurel, S., Borée J., and Lumley, J.L. Extended Proper Orthogonal Decomposition: Application to Jet/Vortex Interaction. *Flow, Turbulence and Combustion*, 67:125–136, 2001.

[54] Meyer, K.E., Özcan, O., Larsen, P.S., and Westergaard, C.H. Stereoscopic PIV measurements in a jet in crossflow. Proceedings of *Second International Symposium on Turbulence and Shear Flow Phenomena*, 27–29 June, Stockholm, Sweden, 2001.

[55] Meyer, K.E., Özcan, O., and Westergaard, C.H. Flow Mapping of a Jet in Crossflow with Stereoscopic PIV. *Journal of Visualization*, 5(3):225–232, 2002.

[56] MEYER, K.E. AND WESTERWEEL, J. Advection velocities of flow structures estimated from particle image velocimetry measurements in a pipe. *Exp. Fluids*, 29(7):S237–S247, 2000.

[57] MOIN, P. AND MOSER, R. Characteristic-eddy decomposition of turbulence in a channel. *J. Fluid Mech.*, 200:471–509, 1989.

[58] MOIN, P. Probing turbulence via large eddy simulation, *AIAA* paper 84-0174, 1984.

[59] NAGUIB, A.M., WARK, C.E., AND JUCKENHÖFEL, O. Stochastic estimation and flow sources associated with surface pressure events in a turbulent boundary layer. *Phys. Fluids.*, 13(9):2611–2626, 2001.

[60] NIELSEN, P.V., RESTIVO, A., AND WHITELAW, J.H. The Velocity Characteristics of Ventilated Rooms. *J. Fluids Engng.*, 100:291–298, 1978.

[61] NIELSEN, P.V. Specification of a two-dimensional test case. *International Energy Agency, Annex 20: Air flow pattern within buildings.* Dept. of Building Technology and Structural Engineering, Aalborg University, Denmark. ISSN 0902-7513 R9040, 1990.

[62] ÖZCAN, O. AND LARSEN, P.S. An experimental study of a turbulent jet in cross-flow by using LDA. Department report, MEK–FM 2001–02, Department of Mechanical Engineering, Technical University of Denmark. ISBN 87-7475-247-2, 2001.

[63] PAYNE, F.R. AND LUMLEY, J.L. Large-eddy structure of the turbulent wake behind a circular cylinder. *Phys. Fluids.*, 10:S194–196, 1967.

[64] PEDERSEN, N. *Experimental Investigation of Flow Structures in a Centrifugal Pump Impeller using Particle Image Velocimetry.* PhD Thesis, Dept. of Energy Engineering, Technical University of Denmark. ET-PHD 2000-05, ISBN 87-7475-239-1, 2000.

[65] PEDERSEN, M. *Functional Analysis in Applied Mathematics and Engineering.* Chapman & Hall/CRC, 2000.

[66] PEDERSEN, J.M. AND MEYER, K.E. POD analysis of flow structures in a scale model of a ventilated room. *Exp. Fluids*, 33:940–949, 2002.

[67] PELLICCIA–KRAFT, B.J. AND WATT, D.W. Visualization of coherent structure in scalar fields of unsteady jet flows with interferometric tomography and proper orthogonal decomposition. *Exp. Fluids*, 30:633–644, 2001.

[68] PRASAD, A.K. AND ADRIAN, R.J. Stereoscopic particle image velocimetry applied to liquid flows. *Exp. Fluids*, 15:49–60, 1993.

[69] PRASAD, R.R. AND SREENIVASAN, K.R. Scalar interfaces in digital images of turbulent flows. *Exp. Fluids*, 7(4):259–264, 1989.

[70] PRASAD, A.K. Stereoscopic particle image velocimetry. *Exp. Fluids*, 29:103–116, 2000.

[71] RAFFEL, M., WILLERT, C., AND KOMPENHANS, J. *Particle Image Velocimetry - A Practical Guide.* Springer Verlag, 1998.

[72] RAJARATNAM, N. *Turbulent Jets.* Elsevier Scientific Publishing Company, Amsterdam, 1976.

[73] REMPFER, D. AND FASEL, H.F. Evolution of three-dimensional coherent structures in a flat-plate boundary layer. *J. Fluid Mech.*, 260:351–375, 1994.

[74] REMPFER, D. Investigations of boundary layer transition via Galerkin projection on empirical eigenfunctions. *Phys. Fluids.*, 8(1):175–188, 1996.

[75] REMPFER, D. On Low-Dimensional Galerkin Models for Fluid Flow. *Theoret. Comput. Fluid Dynamics*, 14:75–88, 2000.

[76] REYNOLDS, W.C. Large-scale instabilities of turbulent wakes. *J. Fluid Mech.*, 54(3):481–488, 1972.

[77] SCARANO, F., BENOCCI, C., AND RIETHMULLER, M.L. Pattern recognition analysis of the turbulent flow past a backward facing step. *Phys. Fluids.*, 11(12):3808–3818, 1999.

[78] SIROVICH, L. AND EVERSON, R. A Karhunen-Loève analysis of episodic phenomena., 1998. Unpublished.
Downloadable on http://camelot.mssm.edu/publications/larry.html.

[79] SIROVICH, L. Turbulence and the dynamics of coherent structures. Part I: Coherent structures. *Quart. Appl. Math.*, 45(3):561–571, 1987.

[80] SUMER, B.M. AND FREDSØE, J. *Hydrodynamics Around Cylindrical Structures.* World Scientific Publishing Co. Pte. Ltd., 1997.

[81] TANG, S. AND AUBRY, N. Suppression of vortex shedding inspired by a low-dimensional model. *Journal of Fluids and Structures*, 14:443–468, 2000.

[82] TENNEKES, H. AND LUMLEY, J.L. *A First Course in Turbulence.* The MIT Press, Cambridge, Massachusetts, 1972.

[83] TOWNSEND, A.A. *The Structure of Turbulent Shear Flow.* Cambridge University Press, 1956.

[84] ULLUM, U. *Imaging Techniques for Planar Velocity and Concentration Measurements.* PhD Thesis, Dept. of Energy Engineering, Technical University of Denmark. ET-PHD 1999-03, ISBN 87-7475-223-5, 1999.

[85] VOIGT, L.P.K. *Navier–Stokes Simulations of Airflow in Rooms and Around a Human Body.* PhD Thesis, Dept. of Mechanical Engineering, Technical University of Denmark. ISBN 87-7475-250-2, 2001.

[86] WALKER, D.A. A fluorescence technique for measurement of concentration in mixing liquids. *J. Physics E*, 20(2):217–224, 1987.

[87] WESTERWEEL, J., DABIRI, D., AND GHARIB, M. The effect of a discrete window offset on the accuracy of cross-correlation analysis of digital PIV recordings. *Exp. Fluids*, 23:20–28, 1997.

[88] WESTERWEEL, J. *Digital Particle Image Velocimetry – Theory and Application.* PhD Thesis, Delft University of Technology. Delft University Press, 1993.

[89] WESTERWEEL, J. Effect of Sensor Geometry on the Performance of PIV Interrogation. In R.J. Adrian, D.F.G. Durão, F. Durst, M.V. Heitor, M. Maeda, and J.H. Whitelaw, editors, *Laser Techniques Applied to Fluid Mechanics*, pages 37–56, Springer Verlag, 2000.

[90] WESTERWEEL, J. Efficient detection of spurious vectors in particle image velocimetry. *Exp. Fluids*, 16:236–247, 1994.

[91] WESTERWEEL, J. Fundamentals of digital particle image velocimetry. *Meas. Sci. Technology*, 8:1379–1392, 1997.

[92] WESTERWEEL, J., HOFMANN, T., FUKUSHIMA, C., AND HUNT, J.C.R. The turbulent/non-turbulent interface at the outer boundary of a self-similar turbulent jet. *Exp. Fluids*, 33:873–878, 2002.

[93] WESTERWEEL, J., PEDERSEN, J.M., FUKUSHIMA, C., AND HUNT, J.C.R. Experimental investigation of the turbulent/non-turbulent interface at the outer boundary of a self-similar turbulent jet. Under preparation for the *Journal of Fluid Mechanics*.

[94] WHITE, F.M. *Viscous Fluid Flow.* McGraw–Hill, second edition, 1991.

[95] WILCOX, D.C. *Turbulence Modeling for CFD.* DCW Industries, Inc., second edition, 1998.

[96] WILLERT, C.E. AND GHARIB, M. Digital particle image velocimetry. *Exp. Fluids*, 10:181–193, 1991.

[97] WINTER, M., BARBER, T.J., EVERSON, R.M., AND SIROVICH, L. Eigenfunction Analysis of Turbulent Mixing Phenomena. *AIAA J.* 30(7):1681–1688, 1992.

[98] YUAN, L.L., STREET, R.L., AND FERZIGER, J.H. Large-eddy simulations of a round jet in crossflow. *J. Fluid Mech.*, 379:71–104, 1999.

[99] YUAN, L.L. AND STREET, R.L. Trajectory and entrainment of a round jet in crossflow. *Phys. Fluids.*, 10(9):2323–2335, 1998.

[100] ZHOU, J., ADRIAN, R.J., BALACHANDAR, S., AND KENDALL, T.M. Mechanisms for generating coherent packets of hairpin vortices in channel flow. *J. Fluid Mech.*, 387:353–396, 1999.

Appendices

Appendix A

Derivation of equation (3.6)

The expression to be maximized reads:

$$\frac{(\mathbf{R}(\mathbf{x},\mathbf{x}'),\mathbf{\Phi}(\mathbf{x})\mathbf{\Phi}^*(\mathbf{x}'))}{(\mathbf{\Phi}(\mathbf{x}),\mathbf{\Phi}(\mathbf{x}))} = \lambda \tag{A.1}$$

Introducing a perturbation, the solution $\mathbf{\Phi}(\mathbf{x}) + \epsilon\mathbf{\Upsilon}(\mathbf{x})$ is inserted, where ϵ is a complex constant. For clarity the resulting expression is written on integral form. First, considering the numerator:

$$\begin{aligned} N &= \int_\Omega\int_\Omega \mathbf{R}(\mathbf{x},\mathbf{x}')[(\mathbf{\Phi}(\mathbf{x}) + \epsilon\mathbf{\Upsilon}(\mathbf{x}))^*(\mathbf{\Phi}(\mathbf{x}') + \epsilon\mathbf{\Upsilon}(\mathbf{x}'))]d\mathbf{x}d\mathbf{x}' \\ &= \int_\Omega\int_\Omega \mathbf{R}(\mathbf{x},\mathbf{x}')[\mathbf{\Phi}^*(\mathbf{x})\mathbf{\Phi}(\mathbf{x}') + \epsilon\mathbf{\Phi}^*(\mathbf{x})\mathbf{\Upsilon}(\mathbf{x}') + \epsilon^*\mathbf{\Upsilon}^*(\mathbf{x})\mathbf{\Phi}(\mathbf{x}') + \epsilon^*\epsilon\mathbf{\Upsilon}^*(\mathbf{x})\mathbf{\Upsilon}(\mathbf{x}')]d\mathbf{x}d\mathbf{x}' \end{aligned}$$

Which from the definition of the inner product can be written:

$$\begin{aligned} N = (\mathbf{R}(\mathbf{x},\mathbf{x}'),\mathbf{\Phi}(\mathbf{x})\mathbf{\Phi}^*(\mathbf{x}')) + \epsilon(\mathbf{R}(\mathbf{x},\mathbf{x}'),\mathbf{\Phi}(\mathbf{x})\mathbf{\Upsilon}^*(\mathbf{x}')) \\ +\epsilon^*(\mathbf{R}(\mathbf{x},\mathbf{x}'),\mathbf{\Upsilon}(\mathbf{x})\mathbf{\Phi}^*(\mathbf{x}')) + \epsilon^*\epsilon(\mathbf{R}(\mathbf{x},\mathbf{x}'),\mathbf{\Upsilon}(\mathbf{x})\mathbf{\Upsilon}^*(\mathbf{x}')) \end{aligned} \tag{A.2}$$

(The constants ϵ and ϵ^* are moved outside the integration sign.)

In the same way for the denominator:

$$\begin{aligned} D &= \int_\Omega (\mathbf{\Phi}(\mathbf{x}) + \epsilon\mathbf{\Upsilon}(\mathbf{x}))(\mathbf{\Phi}(\mathbf{x}) + \epsilon\mathbf{\Upsilon}(\mathbf{x}))^* d\mathbf{x} \\ &= \int_\Omega [\mathbf{\Phi}(\mathbf{x})\mathbf{\Phi}^*(\mathbf{x}) + \epsilon^*\mathbf{\Phi}(\mathbf{x})\mathbf{\Upsilon}^*(\mathbf{x}) + \epsilon\mathbf{\Upsilon}(\mathbf{x})\mathbf{\Phi}^*(\mathbf{x}) + \epsilon\epsilon^*\mathbf{\Upsilon}(\mathbf{x})\mathbf{\Upsilon}^*(\mathbf{x})]d\mathbf{x} \end{aligned}$$

which is written:

$$D = (\mathbf{\Phi}(\mathbf{x}),\mathbf{\Phi}(\mathbf{x})) + \epsilon^*(\mathbf{\Phi}(\mathbf{x}),\mathbf{\Upsilon}(\mathbf{x})) + \epsilon(\mathbf{\Upsilon}(\mathbf{x}),\mathbf{\Phi}(\mathbf{x})) + \epsilon\epsilon^*(\mathbf{\Upsilon}(\mathbf{x}),\mathbf{\Upsilon}(\mathbf{x})) \tag{A.3}$$

For (A.1) to attain a maximum it is required that the first derivative with respect to ϵ of the perturbed expression be zero. Or equivalently that the first derivative with respect to ϵ^* be zero (see [49]). Using the latter and employing the basic rules of differentiation then leads to:

$$\left.\frac{\frac{dN}{d\epsilon^*}D - \frac{dD}{d\epsilon^*}N}{D^2}\right|_{\epsilon^*=0} = 0$$

From which

$$(\mathbf{R}(\mathbf{x},\mathbf{x}'),\boldsymbol{\Upsilon}(\mathbf{x})\boldsymbol{\Phi}^*(\mathbf{x}'))(\boldsymbol{\Phi}(\mathbf{x}),\boldsymbol{\Phi}(\mathbf{x})) - (\boldsymbol{\Phi}(\mathbf{x}),\boldsymbol{\Upsilon}(\mathbf{x}))(\mathbf{R}(\mathbf{x},\mathbf{x}'),\boldsymbol{\Phi}(\mathbf{x})\boldsymbol{\Phi}^*(\mathbf{x}')) = 0$$

$$\Downarrow$$

$$\frac{(\mathbf{R}(\mathbf{x},\mathbf{x}'),\boldsymbol{\Upsilon}(\mathbf{x})\boldsymbol{\Phi}^*(\mathbf{x}'))}{(\boldsymbol{\Phi}(\mathbf{x}),\boldsymbol{\Upsilon}(\mathbf{x}))} = \frac{(\mathbf{R}(\mathbf{x},\mathbf{x}'),\boldsymbol{\Phi}(\mathbf{x})\boldsymbol{\Phi}^*(\mathbf{x}'))}{(\boldsymbol{\Phi}(\mathbf{x}),\boldsymbol{\Phi}(\mathbf{x}))}$$

And finally using (A.1):

$$(\mathbf{R}(\mathbf{x},\mathbf{x}'),\boldsymbol{\Upsilon}(\mathbf{x})\boldsymbol{\Phi}^*(\mathbf{x}')) = \lambda(\boldsymbol{\Phi}(\mathbf{x}),\boldsymbol{\Upsilon}(\mathbf{x})) \tag{A.4}$$

Appendix B

Derivation of equation (4.4)

Consider the expression for e_1 (analogous calculations can be made for $i = 2, 3$). With N events this expression becomes:

$$e_1 = \langle [u_1' - A_{1j}u_j]^2 \rangle = \langle [u_1' - A_{11}u_1 - A_{12}u_2 - \cdots - A_{1N}u_N]^2 \rangle \tag{B.1}$$

For e_1 to attain its minimum value it must be required that:

$$\frac{\partial e_1}{\partial A_{11}} = \frac{\partial e_1}{\partial A_{12}} = \cdots = \frac{\partial e_1}{\partial A_{1N}} = 0$$

The first of these equations yields:

$$2\langle [u_1' - A_{11}u_1 - A_{12}u_2 - \cdots - A_{1N}u_N]u_1 \rangle = 0$$

$$\Downarrow$$

$$\langle u_1'u_1 \rangle - A_{11}\langle u_1u_1 \rangle - A_{12}\langle u_2u_1 \rangle - \cdots - A_{1N}\langle u_Nu_1 \rangle = 0 \tag{B.2}$$

Where it has been utilized that the A_{ij} are time independent. Similarly, the other equations lead to the following expressions:

$$\langle u_1'u_2 \rangle - A_{11}\langle u_1u_2 \rangle - A_{12}\langle u_2u_2 \rangle - \cdots - A_{1N}\langle u_Nu_2 \rangle = 0 \tag{B.3}$$

$$\vdots$$

$$\langle u_1'u_N \rangle - A_{11}\langle u_1u_N \rangle - A_{12}\langle u_2u_N \rangle - \cdots - A_{1N}\langle u_Nu_N \rangle = 0 \tag{B.4}$$

Rewriting equations (B.2)–(B.4) with unknowns A_{11}, A_{12} up to A_{1N} on matrix–vector form, and using the fact that $\langle u_iu_j \rangle = \langle u_ju_i \rangle$, then yields:

$$\begin{bmatrix} \langle u_1u_1 \rangle & \langle u_1u_2 \rangle & \dots & \langle u_1u_N \rangle \\ \langle u_1u_2 \rangle & \langle u_2u_2 \rangle & \dots & \langle u_2u_N \rangle \\ \vdots & \vdots & \ddots & \vdots \\ \langle u_1u_N \rangle & \langle u_2u_N \rangle & \dots & \langle u_Nu_N \rangle \end{bmatrix} \begin{bmatrix} A_{11} \\ A_{12} \\ \vdots \\ A_{1N} \end{bmatrix} = \begin{bmatrix} \langle u_1'u_1 \rangle \\ \langle u_1'u_2 \rangle \\ \vdots \\ \langle u_1'u_N \rangle \end{bmatrix} \tag{B.5}$$

which is exactly the part of the system

$$\langle u_j(\mathbf{x})u_k(\mathbf{x}) \rangle A_{ij}(\mathbf{x}, \mathbf{x}') = \langle u_i(\mathbf{x}')u_k(\mathbf{x}) \rangle \tag{B.6}$$

corresponding to A_{1j}.